

REVIEW ARTICLE

Fluctuations and Correlations in Nucleus-Nucleus Collisions within Transport Models

V.P. Konchakovski^{1,2}, M.I. Gorenstein^{1,3},
E.L. Bratkovskaya² and W. Greiner³

¹Bogolyubov Institute for Theoretical Physics, Kiev, Ukraine

²Institute for Theoretical Physics, University of Frankfurt, Germany

³Frankfurt Institute for Advanced Studies, University of Frankfurt, Germany

Abstract. Particle number fluctuations and correlations in nucleus-nucleus collisions at SPS and RHIC energies are studied within microscopic transport approaches. In this review we focus on the Hadron-String-Dynamics (HSD) and Ultra-relativistic-Quantum-Molecular-Dynamics (UrQMD) models. The obtained results are compared with the available experimental data as well as with the statistical models and the model of independent sources. In particular the role of the experimental centrality selection and acceptance is discussed in detail for a variety of experimental fluctuations and correlation observables with the aim to extract information on the critical point in the (T, μ_B) plane of strongly interacting matter.

Contents

1	Introduction	4
1.1	Relativistic Heavy-Ion Collisions	4
1.2	Fluctuations and Correlations in High Energy Collisions	6
1.3	Outline of the Review	8
2	Concept of Transport Approaches	8
2.1	The covariant off-shell transport approach	9
2.2	On-shell limit	10
2.3	Basic concept of HSD and UrQMD	11
3	Multiplicity Fluctuations in Nucleus-Nucleus Collisions at the SPS	12
3.1	Fluctuations in the Number of Participants	12
3.2	HSD and UrQMD Results for Pb+Pb at 158 AGeV	13
3.3	Transparency and Mixing in Nucleus-Nucleus Collisions	17
4	Multiplicity Fluctuations in Central Nucleus-Nucleus Collisions	21
4.1	Inelastic N+N and Central A+A Collisions	22
4.2	Comparison with the NA49 Data	24
5	Dependence on Energy and Atomic Number	27
5.1	Why Does One Need Central Collisions of Light Ions?	28
5.2	Multiplicity Fluctuations at Zero Impact Parameter	30
5.3	Centrality Trigger with the Number of Projectile Participants	33
6	Fluctuations and Correlations in Au+Au Collisions at RHIC	38
6.1	Multiplicity Fluctuations in Au+Au Collisions at RHIC	38
6.2	Forward-Backward Correlations	40
6.3	Glauber Monte Carlo Model	41
6.4	HSD Transport Model Simulations	44
7	Fluctuations of Conserved Charges in Nucleus-Nucleus Collisions	47
7.1	Net Baryon Number Fluctuations	47
7.2	Net Electric Charge Fluctuations	49
8	Fluctuations of Ratios in Nucleus-Nucleus Collisions	52
8.1	Notations and Approximations	53
8.2	Mixed Events Procedure	54
8.3	Hadron Scaled Variances and Correlation Coefficients	55
8.4	Excitation Function for the Fluctuations of Ratios	61
9	Summary	64

	3
Acknowledgments	68
References	68

1. Introduction

1.1. Relativistic Heavy-Ion Collisions

Hot and dense nuclear matter can be generated in the laboratory in a wide range of temperatures and densities by colliding atomic nuclei at high energies. In the collision zone the matter is heated and compressed for a very short period of time. If the energy pumped into the formed fireball is sufficiently large the quark-gluon substructure of nucleons comes into play. At moderate temperatures, nucleons are excited to short-lived states (baryonic resonances) which decay by the emission of mesons. At higher temperatures, also baryon-antibaryon pairs are created. This mixture of baryons, antibaryons and mesons, all strongly interacting particles, is generally called hadronic matter, or baryonic matter if baryons prevail. At even higher temperatures or densities the hadrons melt and the constituents, the quarks and gluons, form a new phase, the Quark-Gluon Plasma (QGP).

High-energy heavy-ion collision experiments provide the unique possibility to create and investigate these extreme states of matter. The study of matter at extremely high temperature and baryon density, where the hadronic matter transforms to a QGP is the aim of a variety of experiments at current and future facilities: NA38, NA49, NA50, NA60 and NA61/SHINE at the Super-Proton-Synchrotron (SPS) [1–5]; PHENIX, STAR, PHOBOS and BRAHMS at the Relativistic-Heavy-Ion-Collider (RHIC) [6–9]; ALICE at the Large-Hadron-Collider (LHC) [10]; CBM and PANDA at the Facility for Antiproton and Ion Research (FAIR) [11]; MPD at the Nuclotron-based Ion Collider fAcility (NICA) [12].

Relativistic nucleus-nucleus (A+A) collisions have been studied so far at beam energies from 0.1 to 2 AGeV at the SIS (SchwerIonen-Synchrotron), from 2 to 11.6 AGeV at the AGS (Alternating Gradient Synchrotron) and from 20 to 160 AGeV at the SPS [13,14]. While part of these programs are closed now, the heavy-ion research has been extended at RHIC with Au+Au collisions at c.m. nucleon pair energies $\sqrt{s_{NN}}$ from ~ 20 to 200 GeV (equivalent energies in a fixed target experiment: 0.2 to 21.3 ATeV). In the near future, further insight into the physics of matter at even more extreme conditions will be gained at the LHC, which will reach center-of-mass energies of the few TeV scale. Apart from LHC, the SPS successor SHINE operates at CERN in order to scan the 10A-158AGeV energy range with light and intermediate mass nuclei [5]. At FAIR, which is expected to start operation in 2015, collisions of gold nuclei from 5 AGeV up to 35 AGeV will be studied. At NICA it is planned to start the experimental program of colliding Au and/or U ions as well as polarized light nuclei at energies up to of 5 AGeV in 2013 (an upgrade to $\sqrt{s_{NN}} = 9$ GeV is foreseen [15]).

At very high beam energies – as available at RHIC and LHC – the research programs concentrate on the study of the properties of deconfined QCD matter at very high temperatures and almost zero net baryon densities, whereas at moderate beam energies (SPS, FAIR and NICA) experiments focus on the search for structures in the QCD phase diagram such as the critical endpoint, the predicted first order phase transition between

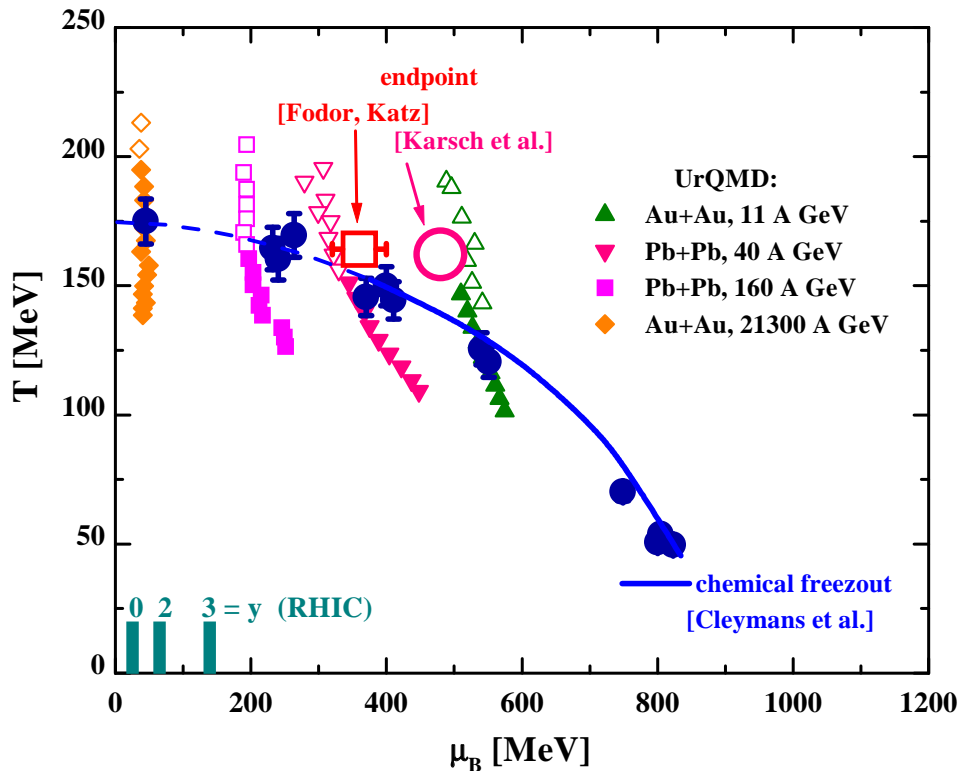


Figure 1. The phase diagram with the critical end point at $\mu_B \approx 400$ MeV, $T \approx 150$ MeV as predicted by Lattice QCD. In addition, the time evolution in the $T - \mu$ -plane of a central cell in UrQMD calculations [24, 25] is depicted for different bombarding energies. At RHIC (see insert at the μ_B scale) large μ_B can be accessible in the fragmentation region only. The figure is taken from Ref. [26].

hadronic and partonic matter, and the chiral phase transition. The critical endpoint and the first order phase transition are expected to occur at finite baryon chemical potential and moderate temperatures.

Particle yields or ratios measured at different beam energies and analyzed with the statistical model provide sets of thermal parameters, temperature T and baryo-chemical potential μ_B , which establish a “line of chemical freeze-out” [16–18]. The results of the fits to experimental data are shown in a phase diagram of hadronic and quark-gluon matter in Fig. 1 [19] with full circles.

Lattice QCD results [20, 21] show a crossing, but no first order phase transition to the QGP for vanishing or small chemical potentials μ_B , i.e. at the conditions accessible at central rapidities at RHIC full energies. A first order phase transition is assumed at high baryochemical potentials or baryon densities. This corresponds to SPS energies and in the fragmentation region of RHIC [22, 23]. The critical baryochemical potential is predicted [20, 21] to be $\mu_B^c = 400 \pm 50$ MeV and the critical temperature $T_c = 140 \div 160$ MeV.

The thermodynamic parameters T and μ_B – as extracted from the microscopic UrQMD approach in the central overlap region of Pb+Pb or Au+Au collisions [26] – are shown in Fig. 1, where the full dots with error bars denote the chemical freeze-

out parameters determined from fits to the experimental yields [18]. The triangular and quadratic symbols (time-ordered in vertical sequence) stand for temperatures T and chemical potentials μ_B extracted from UrQMD transport calculations in central Au+Au (Pb+Pb) collisions at RHIC (21.3 ATeV), SPS (160, 40 AGeV) and AGS (11 AGeV) [24, 25] as a function of the reaction time (separated by 1 fm/c steps from top to bottom). The open symbols denote non-equilibrium configurations and correspond to T parameters extracted from the transverse momentum distributions, whereas the full symbols denote configurations in approximate pressure equilibrium in longitudinal and transverse direction. The T and μ_B values found in the transport model suggest that local thermal and chemical equilibrium may exist in the interesting regions of the phase diagram: the line of the first order phase transition, the critical point, and the region of a crossover. Note, however, that most transport models in their present formulation (such as UrQMD) have no explicit QGP phase.

1.2. Fluctuations and Correlations in High Energy Collisions

Fluctuations and correlations are important characteristics of any physical system. They provide essential information about the effective degrees of freedom. In general, one can distinguish between several classes of fluctuations. There are “dynamical” fluctuations and correlations reflecting the underlying dynamics of the system. There are also “trivial” fluctuations induced by the measurement process itself, such as finite number statistics, etc. They should be clarified and subtracted in order to access the dynamical fluctuations which tell us about the properties of the system as well as susceptibilities.

The event-by-event fluctuations in high energy A+A collisions are expected to be closely related to the transitions between different phases of QCD matter. By measuring the fluctuations one should observe anomalies from the onset of deconfinement and dynamical instabilities when the expanding system goes through the 1-st order transition line between the QGP and the hadron gas. It is predicted [27] that the onset of deconfinement should lead to a non-monotonous behavior in the energy dependence of multiplicity fluctuations, the so-called “shark fin”. Furthermore, the QCD critical point may be signaled by a characteristic pattern in enhanced fluctuations [28].

Indeed, the Lattice QCD calculations in Ref. [29] indicate a sharp increase of the susceptibilities at the critical point for non-zero chemical potentials. This is illustrated in Fig. 2 which shows the dimensionless quark number susceptibility χ_q/T^2 as a function of T/T_0 for various μ_q/T where the quark number (q) susceptibility is defined for the system in thermal equilibrium (for a grand-canonical ensemble) as follows [29]:

$$\frac{\chi_q}{T^2} = \left(\frac{\partial}{\partial(\mu_u/T)} + \frac{\partial}{\partial(\mu_d/T)} \right) \frac{n_u + n_d}{T^3} \quad (1)$$

with n_q denoting the quark number density. The peak, which develops in χ_q with increasing μ_q , is a sign that fluctuations in the baryon density are growing when approaching the critical endpoint in the (μ, T) . Thus A+A collisions in the SPS energy region are expected to be a suitable tool for a search of signatures for the critical point.

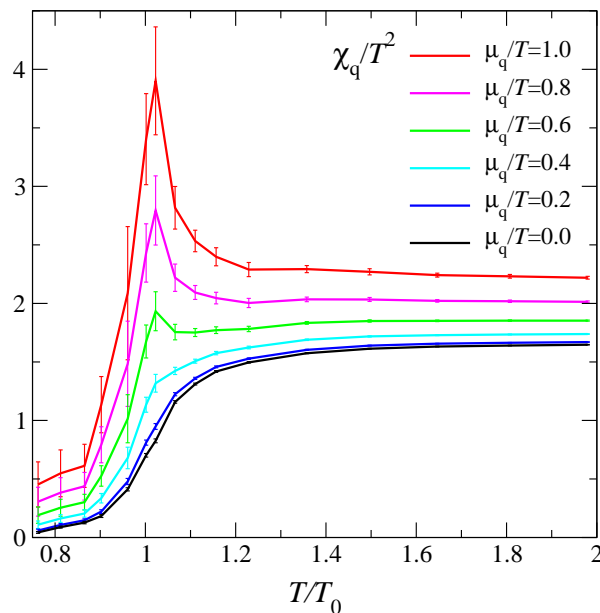


Figure 2. χ_q/T^2 as a function of T/T_0 for various μ_q/T according to Ref. [29].

An ambitious experimental program for the search of the QCD critical point has been started by the NA61 Collaboration at the CERN SPS [5,30]. The program includes a variation in the atomic number A of the colliding nuclei as well as an energy scan. This allows to explore the phase diagram in the $T - \mu_B$ plane near the critical point. One expects to ‘locate’ the position of the critical point by studying its ‘fluctuation signals’. High statistics multiplicity fluctuation data will be taken for p+p, C+C, S+S, In+In, and Pb+Pb collisions at bombarding energies of $E_{lab}=10, 20, 30, 40, 80,$ and 158 AGeV.

The QCD critical point is expected to be experimentally seen as a non-monotonic dependence of the multiplicity fluctuations, i.e. a specific combination of atomic number A and bombarding energy E_{lab} could move the chemical freeze-out of the system close to the critical point and show a ‘spike’ in the multiplicity fluctuations. Since the available microscopic transport approaches Hadron-String-Dynamics (HSD) and Ultra-relativistic-Quantum-Molecular-Dynamics (UrQMD), which operate from lower SIS to top RHIC energies, do not include explicitly a phase transition from a hadronic to a partonic phase, we can not make a clear suggestion for the location of the critical point – this is beyond the scope of hadron-string models. However, this study should be helpful in the interpretation of the upcoming experimental data since it will allow to subtract simple dynamical and geometrical effects from the expected QGP signal. The deviations of the future experimental data from the HSD and UrQMD predictions may be considered as an indication for the critical point signals.

We will deal in particular with particle number event-by-event fluctuations. They are quantified by the ratio of the variance of the multiplicity distribution to its mean value, the scaled variance. Let’s introduce the corresponding notations: The

deviation ΔN_A from the average number $\langle N_A \rangle$ of the particle species A is defined by $N_A = \langle N_A \rangle + \Delta N_A$, while the covariance for species A and B is

$$\Delta(N_A, N_B) \equiv \langle \Delta N_A \Delta N_B \rangle = \langle N_A N_B \rangle - \langle N_A \rangle \langle N_B \rangle, \quad (2)$$

the variance,

$$\text{Var}(N_A) \equiv \Delta(N_A, N_A) = \langle (\Delta N_A)^2 \rangle = \langle N_A^2 \rangle - \langle N_A \rangle^2, \quad (3)$$

the scaled variance,

$$\omega_A \equiv \frac{\text{Var}(N_A)}{\langle N_A \rangle} = \frac{\langle (\Delta N_A)^2 \rangle}{\langle N_A \rangle} = \frac{\langle N_A^2 \rangle - \langle N_A \rangle^2}{\langle N_A \rangle}, \quad (4)$$

and the correlation coefficient,

$$\rho_{AB} \equiv \frac{\langle \Delta N_A \Delta N_B \rangle}{[\langle (\Delta N_A)^2 \rangle \langle (\Delta N_B)^2 \rangle]^{1/2}}. \quad (5)$$

Note that an absence of correlations, $\rho_{AB} = 0$, implies $P(N_A, N_B) = P_A(N_A) \times P_B(N_B)$, and $\omega = 1$ for the Poisson multiplicity distribution, $P(N) = \bar{N}^N \exp(-\bar{N})/N!$.

1.3. Outline of the Review

The Sec. 2 provides the basic concept of transport approaches. The centrality (Sec. 3), energy (Sec. 4) and system size dependence (Sec. 5) of event-by-event fluctuations in the particle multiplicity are studied in A+A collisions at the SPS CERN energies. The results on particle number fluctuations and long-range forward-backward multiplicity correlations at RHIC BNL energies are discussed in Sec. 6. Electric charge and baryonic number fluctuations are considered in Sec. 7 while fluctuations of the particle number ratios are presented in Sec. 8. A summary in Sec. 9 concludes the review.

The transport model calculations are performed within the HSD and UrQMD approaches. The results of both models qualitatively agree to each other. In some cases – to illustrate the systematic uncertainties of the transport model approaches for a specific observable – we will present the results of both models. Otherwise the results of only HSD simulations are presented for brevity.

2. Concept of Transport Approaches

Two independent transport models that employ hadronic and string degrees of freedom, i.e. HSD [31, 32] and UrQMD [33, 34], have been used for studying the fluctuations in $p+p$ and $A+A$ collisions. Both approaches take into account the formation and multiple re-scattering of hadrons in A+A reactions and thus dynamically describe the generation of pressure in the hadronic expansion phase. Though quite different in the numerical realization, both models are based on the same concepts and dynamical degrees of freedom: strings, quarks, diquarks ($q, \bar{q}, qq, \bar{q}\bar{q}$) as well as hadronic degrees of freedom in the confined phase. We stress again that both approaches do not include an explicit phase transition to a quark-gluon plasma.

2.1. The covariant off-shell transport approach

The novel HSD model (extended for off-shell dynamics [35]) is based on the solution of generalized covariant off-shell transport equations for hadronic degrees of freedom (for the details of the covariant off-shell transport theory we refer the reader to the review [36] and references therein). As demonstrated in [35] the off-shell dynamics is particularly important for the transport description of the propagation and interaction of resonances with broad spectral functions which change their properties in the hot and dense medium (e.g. for the vector mesons).

The coupled set of transport equations for the phase-space distributions $N_h(x, p)$ ($x = (t, \vec{r})$, $p = (\varepsilon, \vec{p})$) of fermion h [31, 32, 37] with a spectral function $A_h(x, p)$ (using the Green function decomposition $iG_h^<(x, p) = N_h(x, p)A_h(x, p)$) is formally written as

$$\begin{aligned} & \left\{ (\Pi_\mu - \Pi_\nu \partial_\mu^p U_h^\nu - m_h^* \partial_\mu^p U_h^S) \partial_x^\mu + (\Pi_\nu \partial_\mu^x U_h^\nu + m_h^* \partial_\mu^x U_h^S) \partial_p^\mu \right\} N_h(x, p) A_h(x, p) \\ & - \{i\Sigma^<, Re G^R\} = \sum_{h_2 h_3 h_4} Tr_2 Tr_3 Tr_4 [T^\dagger T]_{12 \rightarrow 34} \delta^4(\Pi + \Pi_2 - \Pi_3 - \Pi_4) \\ & \quad \times A_h(x, p) A_{h_2}(x, p_2) A_{h_3}(x, p_3) A_{h_4}(x, p_4) \\ & \quad \times \left\{ N_{h_3}(x, p_3) N_{h_4}(x, p_4) \bar{f}_h(x, p) \bar{f}_{h_2}(x, p_2) - N_h(x, p) N_{h_2}(x, p_2) \bar{f}_{h_3}(x, p_3) \bar{f}_{h_4}(x, p_4) \right\}. \end{aligned} \quad (6)$$

Here $\partial_\mu^x \equiv (\partial_t, \vec{\nabla}_r)$, $\partial_\mu^p \equiv (\partial_\varepsilon, \vec{\nabla}_p)$, ($\mu = 0, 1, 2, 3$) and $\bar{f}_h(x, p) = 1 - N_h(x, p)$ for fermions.

The 'backflow' term in (6) – i.e. the Poisson bracket with the self-energy and retarded Green function – is given by

$$\begin{aligned} & - \{i\Sigma^<, Re G^R\} = \partial_p^\mu \left(\frac{M_h(x, p)}{M_h(x, p)^2 + \Gamma_h(x, p)^2/4} \right) \partial_\mu^x (N_h(x, p) \Gamma_h(x, p)) \\ & \quad - \partial_\mu^x \left(\frac{M_h(x, p)}{M_h(x, p)^2 + \Gamma_h(x, p)^2/4} \right) \partial_p^\mu (N_h(x, p) \Gamma_h(x, p)). \end{aligned} \quad (7)$$

It stands for the off-shell evolution which vanishes in the on-shell limit, when the spectral function $A_h(x, p)$ does not change its shape during the propagation through the medium, i.e. $\vec{\nabla}_r \Gamma(x, p) = 0$ and $\vec{\nabla}_p \Gamma(x, p) = 0$ with Γ denoting the local width of the spectral function.

In (6) the trace over particles 2,3,4 reads explicitly for fermions

$$Tr_2 = \sum_{\sigma_2, \tau_2} \frac{1}{(2\pi)^4} \int d^3 p_2 \frac{dM_2^2}{2\sqrt{p_2^2 + M_2^2}}, \quad (8)$$

where σ_2, τ_2 stand for the spin and isospin of particle 2. In case of bosons one has

$$Tr_2 = \sum_{\sigma_2, \tau_2} \frac{1}{(2\pi)^4} \int d^3 p_2 \frac{dp_{0,2}^2}{2}, \quad (9)$$

since here the spectral function A_B is normalized as

$$\int \frac{dp_0^2}{4\pi} A_B(x, p) = 1 \quad (10)$$

whereas for fermions one obtains the normalization

$$\int \frac{dp_0}{2\pi} A_h(x, p) = 1. \quad (11)$$

For the bosons B the mass function is Eq. (7)

$$M_B(x, p) = p_0^2 - \vec{p}^2 - m^2 - \text{Re}\Sigma(x, p) \quad (12)$$

where the (local and nonlocal) self-energies are included in $\text{Re}\Sigma(x, p)$.

The Lorentz covariant mass-function for the fermions is

$$M_h(x, p) = \Pi_0^2 - \vec{\Pi}^2 - m_h^{*2}, \quad (13)$$

with the effective mass and four-momentum given by

$$m_h^*(x, p) = m_h + U_h^S(x, p) \quad (14)$$

$$\Pi^\mu(x, p) = p^\mu - U_h^\mu(x, p).$$

In (14) $U_h^S(x, p)$ and $U_h^\mu(x, p)$ denote the real part of the scalar and vector hadron self-energies, respectively, and m_h stands for the bare (vacuum) mass of baryon h .

In (6) $[T^+T]_{12 \rightarrow 34}$ is the 'transition rate' for the process $1+2 \rightarrow 3+4$ (which is taken to be on-shell in the default HSD approach). In the c.m.s. of the colliding particles the transition rate is given by

$$[T^+T]_{12 \rightarrow 34} \Rightarrow v_{12} \left. \frac{d\sigma}{d\Omega} \right|_{1+2 \rightarrow 3+4}, \quad (15)$$

where $d\sigma/d\Omega$ is the differential cross section of the reaction and v_{12} the relative velocity of particles 1 and 2. Note, that a generalized collision term for $n \leftrightarrow m$ reactions is given in Ref. [38] and optionally included in HSD, which is, however, not used in the present study.

The hadron quasi-particle properties in (6) are defined via the mass-functions (12) or (13) with (14) while the phase-space factors

$$\bar{f}_h(x, p) = 1 \pm N_h(x, p) \quad (16)$$

are responsible for fermion Pauli-blocking or Bose enhancement, respectively, depending on the type of hadron in the final/initial channel. The transport approach (6) is fully specified by $U_h^S(x, p)$ and $U_h^\mu(x, p)$, which determine the mean-field propagation of the hadrons, and by the transition rates T^+T in the collision term, that describe the scattering and hadron production/absorption rates. The coupled set of hadronic transport equations (6) may be employed for a large variety of hadronic systems at relativistic (and non-relativistic) energies.

2.2. On-shell limit

In our present study we will discard the scalar and vector potentials U_h^S and U_h^μ in (6) and (14) which are of minor importance at SPS and RHIC energies due to the dominance of string excitations and decay. Furthermore, we will employ the on-shell limit for the spectral functions

$$A_h(x, p) \sim \delta(p^2 - m_h^2),$$

where m_h denotes the hadron on-shell mass. These (legitimate) approximations - employed in the standard transport approximations - will allow for a large reduction

in the necessary CPU time and a proper statistics for the fluctuation analysis. We mention that each individual cascade simulation will correspond to a micro-canonical non-equilibrium simulation of the dynamics with exact conservation of energy and momentum, baryon number, charge number, strangeness etc.

Also note that the transport equations – in the limits discussed above – yield the well-known statistical distributions

$$N_h(x, p) = \frac{1}{e^{(p_0 - \mu_h)/T} - \eta} \quad (17)$$

with $\eta = 1$ for mesons and $\eta = -1$ for fermions in the limit $t \rightarrow \infty$, if the system is confined to a finite (and fixed) volume. In (17) μ_h and T denote the conventional Lagrange parameters for the chemical potential of hadron h and equilibrium temperature. Accordingly, the transport approaches allow to explore non-equilibrium dynamical effects for fluctuations observables while they smoothly approach the grand canonical ensemble (GCE) in the limit $t \rightarrow \infty$ for stationary systems when averaging over many events with a different amount of excitation energy and different number of produced particles.

2.3. Basic concept of HSD and UrQMD

We recall that in the HSD (v. 2.5) [31, 32, 39] approach nucleons, Δ 's, $N^*(1440)$, $N^*(1535)$, Λ , Σ and Σ^* hyperons, Ξ 's, Ξ^* 's and Ω 's as well as their antiparticles are included on the baryonic side whereas the 0^- and 1^- octet states are incorporated in the mesonic sector. Inelastic baryon–baryon (and meson–baryon) collisions with energies above $\sqrt{s_{th}} \simeq 2.6\text{GeV}$ (and $\sqrt{s_{th}} \simeq 2.3\text{GeV}$) are described by the FRITIOF string model [40] whereas low energy hadron–hadron collisions are modelled in line with experimental cross sections. Low energy cross sections such as threshold meson production in proton–neutron (pn) collisions – which are scarcely available from experiments – are fixed by proton–proton (pp) cross sections and isospin factors emerging from pion-exchange diagrams. Since we address ultra-relativistic collisions at SPS and RHIC energies such 'low energy uncertainties' are of minor relevance here. As pre-hadronic degrees of freedom HSD includes 'effective' quarks (antiquarks) and diquarks (antidiquarks) which interact with cross sections in accordance with the constituent quark model (cf. Refs. [41]).

The UrQMD (v.1.3) transport approach [33, 34] includes all baryonic resonances up to masses of 2 GeV as well as mesonic resonances up to 1.9 GeV as tabulated by the Particle Data Group [42]. For hadronic continuum excitations a string model is used with hadron formation times in the order of 1-2 fm/c depending on the momentum and energy of the created hadron. The transport approach – by construction – yields a good reproduction of nucleon–nucleon, meson–nucleon and meson–meson cross section data in a wide kinematical range [33, 34].

The HSD and UrQMD transport models have been used for the description of pp , pA and AA collisions from SIS to RHIC energies and lead to a fair reproduction of 'bulk' properties such as hadron abundances, rapidity distributions etc. We mention that some

rare probes (e.g. particles with high transverse momentum) are not well described by transport models (cf. Refs. [26, 43, 44]), however, this issue is of minor impact on the fluctuation analysis to be presented below.

3. Multiplicity Fluctuations in Nucleus-Nucleus Collisions at the SPS

This Section contains the results for the particle number fluctuations in Pb+Pb collisions at 158 AGeV within HSD and UrQMD [45]. The results of these transport models are compared with the model of independent sources and with the experimental data of the NA49 Collaboration.

3.1. Fluctuations in the Number of Participants

Fig. 3 demonstrates a typical non-central A+A collision. In each collision only a fraction of all $2A$ nucleons interact. These are called participant nucleons and are denoted as N_P^{proj} and N_P^{targ} for the projectile and target nuclei, respectively. The corresponding nucleons, which do not interact, are called the projectile and target spectators, $N_S^{proj} = A - N_P^{proj}$ and $N_S^{targ} = A - N_P^{targ}$. In the transport models the nucleon spectators are defined according to the criteria, $|y - y_{beam(target)}| \leq 0.32$, which restricts their rapidities.

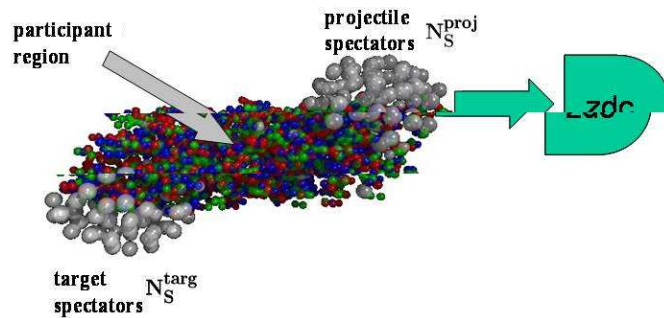


Figure 3. Non-central heavy ion collision: Spectators in the projectile and target are denoted as N_P^{proj} and N_P^{targ} . ‘Participant region’ indicates the region where the particle production occurs due to the interaction of participants from target and projectile. Note that in a fixed target experiment it is possible to fix the number of projectile participants by detecting projectile spectators via a Zero Degree Calorimeter (ZDC).

The fluctuations in high energy A+A collisions are dominated by a geometrical variation of the impact parameter. However, even for the fixed impact parameter the number of participants, $N_P \equiv N_P^{proj} + N_P^{targ}$, fluctuates from event to event. This is due to the fluctuations of the initial states of the colliding nuclei and the probabilistic character of the interaction process. The fluctuations of N_P form usually a large and uninteresting background. In order to minimize its contribution the NA49 Collaboration has selected samples of collisions with a fixed numbers of projectile participants. This

selection is possible due to a measurement of N_S^{proj} in each individual A+A collision by a calorimeter which covers the projectile fragmentation domain. However, even in the samples with $N_P^{proj} = const$ the number of target participants fluctuates considerably. Hence, an asymmetry between projectile and target participants is introduced, i.e. N_P^{proj} is constant by constraint, whereas N_P^{targ} fluctuates.

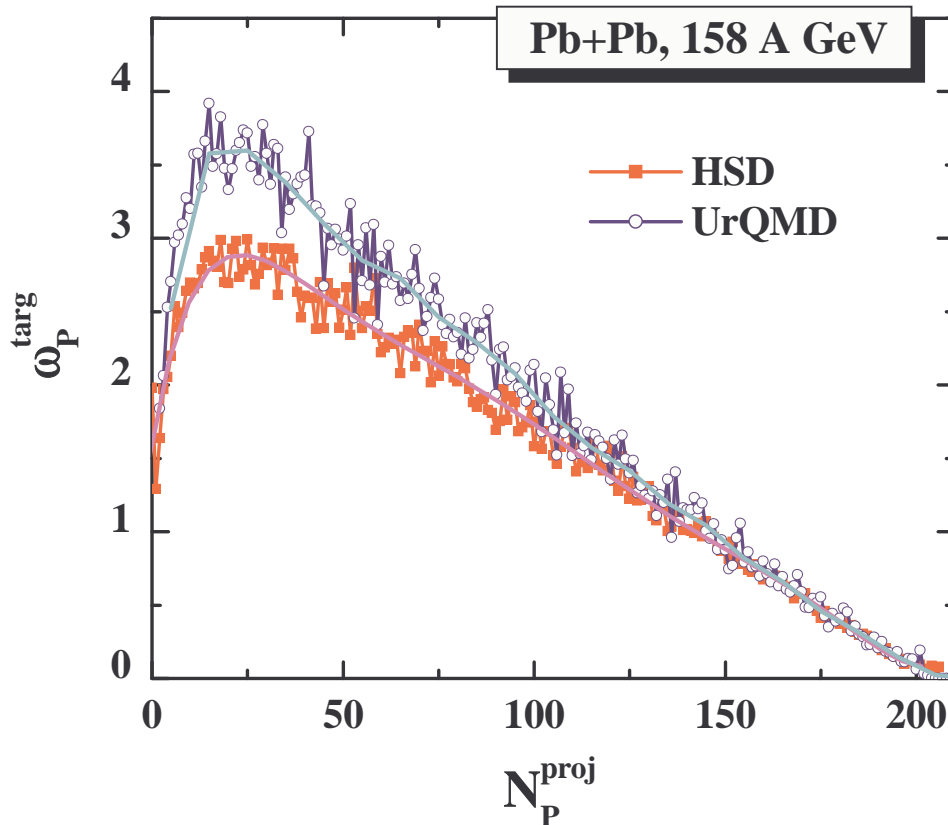


Figure 4. The HSD and UrQMD results for the scaled variance ω_P^{targ} as the function of N_P^{proj} .

From an output of the HSD minimum bias simulations of Pb+Pb collisions at 158 AGeV the samples of events with fixed values of N_P^{proj} have been formed. For the average number of target participants in these samples one finds, $\langle N_P^{targ} \rangle \cong N_P^{proj}$. The deviations are only seen at very small ($N_P^{proj} \approx 1$) and very large ($N_P^{proj} \approx A$) numbers of projectile participants. In each sample with fixed value of N_P^{proj} the N_P^{targ} number fluctuates around its mean value. The scaled variance of these fluctuations is denoted as ω_P^{targ} . Fig. 4 shows both the HSD and UrQMD results for the scaled variance ω_P^{targ} as the function of N_P^{proj} . The fluctuations of N_P^{targ} are quite strong; the largest value of $\omega_P^{targ} = 3 \div 3.5$ occurs at $N_P^{proj} = 20 \div 30$.

3.2. HSD and UrQMD Results for Pb+Pb at 158 AGeV

The NA49 Collaboration has minimized the event by event fluctuations of the number of nucleon participants in measuring the multiplicity fluctuations by selecting the samples

of collisions with a fixed number of projectile spectators, $N_S^{proj} = const$, and thus a fixed number of projectile participants, $N_P^{proj} = A - N_S^{proj}$. From an output of the HSD and UrQMD minimum bias simulations the samples of Pb+Pb events with fixed values of N_P^{proj} have been formed. Fig. 5 presents the HSD and UrQMD results for the scaled variances of negatively, positively, and all charged particles, ω_i (with $i = +, -, ch$), in Pb+Pb collisions at 158 AGeV calculated at fixed N_P^{proj} .

The final particles in the HSD and UrQMD simulations are accepted at rapidities $1.1 < y < 2.6$ (y corresponds to the particle rapidity in the Pb+Pb c.m.s. frame) in accordance to the NA49 transverse momentum filter [46]. This is done to compare the HSD and UrQMD results with the NA49 data. The HSD and UrQMD simulations both show flat ω_i values, $\omega_- \approx \omega_+ \approx 1.2$, $\omega_{ch} \approx 1.5$, and exhibit almost no dependence on N_P^{proj} . The NA49 data, in contrast, exhibit an enhancement in ω_i for $N_P^{proj} \approx 50$. The data show maximum values, $\omega_- \approx \omega_+ \approx 2$ and $\omega_{ch} \approx 3$, and a rather strong dependence on N_P^{proj} .

Fig. 5 also shows results of the HSD and UrQMD simulations for the full 4π acceptance for final particles, and shows the NA49-like acceptance in the mirror rapidity interval, $-2.6 < y < -1.1$ of the target hemisphere. HSD and UrQMD both result in large values of ω_i , i.e. large fluctuations in the backward hemisphere: in the backward rapidity interval $-2.6 < y < -1.1$ (target hemisphere) the fluctuations are much larger than those calculated in the forward rapidity interval $1.1 < y < 2.6$ (projectile hemisphere, where the NA49 measurements have been done). Even much larger fluctuations seen in Fig. 5 follow from the HSD and UrQMD simulations for the full acceptance of final particles.

At fixed values of the numbers of participants N_P^{proj} and N_P^{targ} one can introduce the probability $W_i(N_i; N_P^{targ}, N_P^{proj})$ for producing N_i ($i = -, +, ch$) final hadrons. At fixed N_P^{proj} the averaging procedure is defined as,

$$\langle \dots \rangle \equiv \sum_{N_P^{targ} \geq 1}^A \sum_{N_i \geq 0} \dots W_P(N_P^{targ}; N_P^{proj}) W_i(N_i; N_P^{targ}, N_P^{proj}), \quad (18)$$

where $W_P(N_P^{targ}; N_P^{proj})$ is the probability for a given value of N_P^{targ} in a sample of events with fixed number of the projectile participants N_P^{proj} . Under certain simplifications, the variance can be presented as,

$$Var(N_i) \equiv \langle N_i^2 \rangle - \langle N_i \rangle^2 = \omega_i^* \langle N_i \rangle + \omega_P n_i \langle N_i \rangle, \quad (19)$$

where the scaled variance ω_i^* corresponds to the fluctuations of N_i at fixed values of N_P^{proj} and N_P^{targ} , $n_i \equiv \langle N_i \rangle / \langle N_P \rangle$, and $N_P = N_P^{targ} + N_P^{proj}$ is the total number of participants. In obtaining of Eq. (19) two assumptions have been made. First, it is assumed that ω_i^* does not depend on N_P . The second assumption is that the average multiplicities $\langle N_i \rangle$ are proportional to the number of participating nucleons. Finally, the scaled variances, ω_i , can be presented as:

$$\omega_i \equiv \frac{Var(N_i)}{\langle N_i \rangle} = \omega_i^* + \omega_P n_i. \quad (20)$$

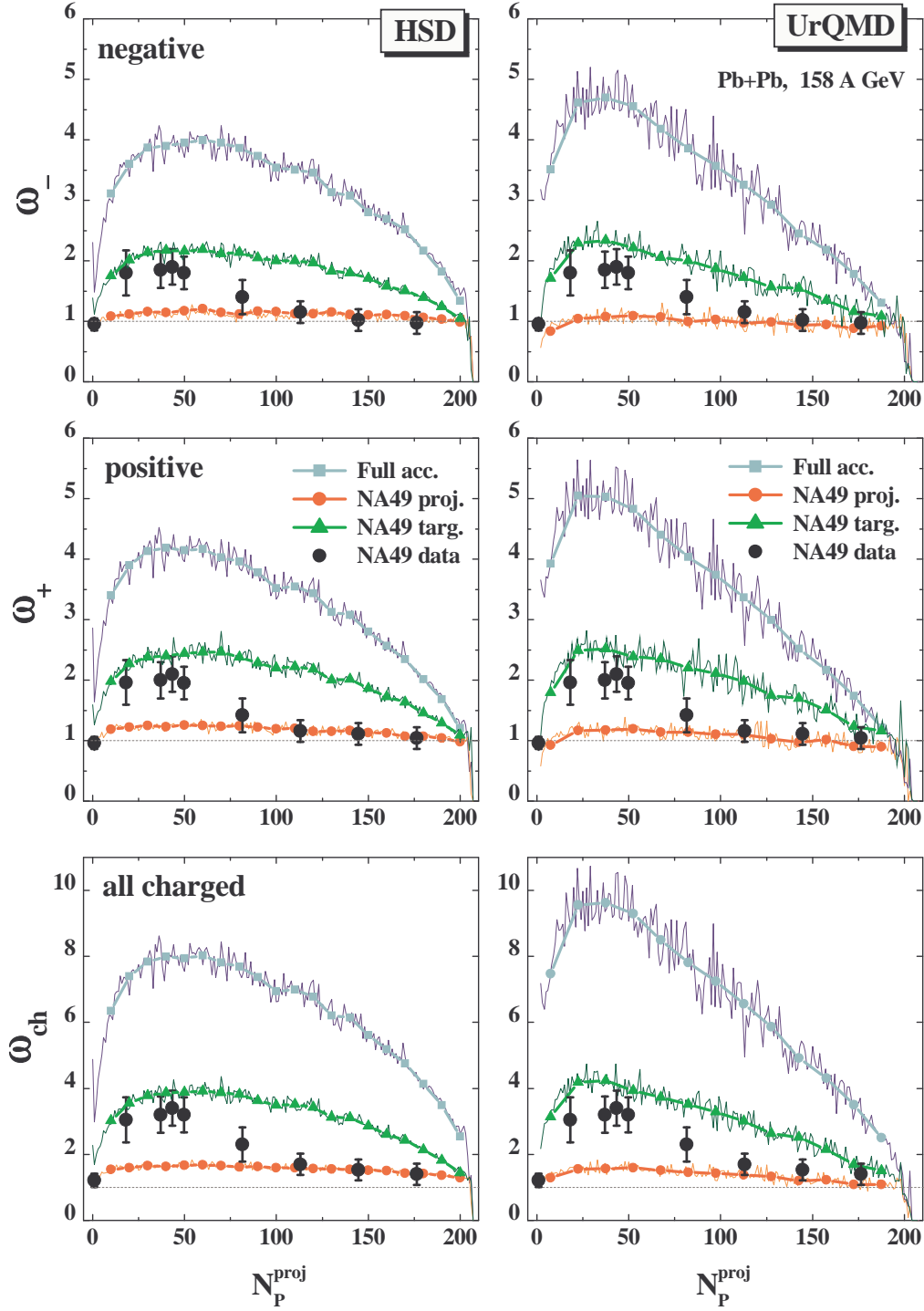


Figure 5. The results of the HSD (left) and UrQMD (right) simulations are shown for ω_- , ω_+ , and ω_{ch} in Pb+Pb collisions at 158 AGeV as functions of N_P^{proj} . The black points are the NA49 data. The different lines correspond to the model simulations with the original NA49 acceptance, $1.1 < y < 2.6$, in the projectile hemisphere (lower lines), the NA49-like acceptance in the mirror rapidity interval, $-2.6 < y < -1.1$, in the target hemisphere (middle lines), and in full 4π acceptance (upper lines).

The average values are $\langle N_P^{targ} \rangle \cong N_P^{proj}$, thus, $\langle N_P^{targ} \rangle \cong \langle N_P \rangle / 2$. Therefore, the scaled variance ω_P for the total number of participants in Eq. (20) equals to $\omega_P = \omega_P^{targ} / 2$ as only a half of the total number of participants does fluctuate. The value of ω_P^{targ} depends on N_P^{proj} , as shown by the HSD and UrQMD results in Fig. 4. The average particle number n_i ($i = +, -, ch$) per participant calculated within the HSD and UrQMD models for full 4π -acceptance show a good agreement with each other as well as with the extrapolated to 4π NA49 data.

Eq. (20) corresponds to the so called model of independent sources (MIS), see, e.g., Ref [47]. One assumes that final particles are produced by the sources. The numbers of the sources are taken to be proportional to the number of projectile and target participant nucleons, and the sources are assumed to be independent of each other. The physical meaning of the sources depends on the model under consideration (e.g., wounded nucleons [48], strings and resonances [31–34], or the fluid cells at chemical freeze-out in the hydrodynamical models). The Eq. (20) presents the final multiplicity fluctuations as a sum of two terms: the fluctuations from one source, ω_i^* , and the contribution due to the fluctuations of the number of sources, $\omega_P n_i$.

In peripheral A+A collisions there are only few nucleon-nucleon (N+N) collisions, and rescatterings are rare. The picture of independent N+N collisions looks thus reasonable. In this case, a hadron production source can be associated with a N+N collision. The multiplicities and scaled variances of N+N is given in terms of proton-proton (p+p), proton-neutron (p+n), and neutron-neutron (n+n) collisions:

$$\langle N_i^{NN} \rangle = \alpha_{pp} \langle N_i^{pp} \rangle + \alpha_{pn} \langle N_i^{pn} \rangle + \alpha_{nn} \langle N_i^{nn} \rangle, \quad (21)$$

$$\omega_i^{NN} = \frac{1}{\langle N_i^{NN} \rangle} [\alpha_{pp} \omega_i^{pp} \langle N_i^{pp} \rangle + \alpha_{pn} \omega_i^{pn} \langle N_i^{pn} \rangle + \alpha_{nn} \omega_i^{nn} \langle N_i^{nn} \rangle], \quad (22)$$

where $\alpha_{pp} = Z^2/A^2 = 0.155$, $\alpha_{pn} = 2Z(A-Z)/A^2 = 0.478$, $\alpha_{nn} = (A-Z)^2/A^2 = 0.367$ are the probabilities of p+p, p+n, and n+n collisions in Pb+Pb reactions ($A=208$, $Z=82$). The average multiplicities and scaled variances for elementary collisions calculated within the HSD simulations at 158 GeV are equal to:

$$\langle N_{ch}^{pp} \rangle = 6.2, \quad \langle N_{ch}^{pn} \rangle = 5.8, \quad \langle N_{ch}^{nn} \rangle = 5.4, \quad (23)$$

$$\omega_{ch}^{pp} = 2.1, \quad \omega_{ch}^{pn} = 2.4, \quad \omega_{ch}^{nn} = 2.9. \quad (24)$$

For negatively and positively charged hadrons, the average multiplicities and scaled variances in elementary reactions can be presented in terms of corresponding quantities for all charged particles:

$$\langle N_{\pm} \rangle = \frac{1}{2} \langle N_{ch} \rangle \pm \gamma, \quad \omega_{\pm} = \frac{1}{2} \omega_{ch} \frac{\langle N_{ch} \rangle}{\langle N_{ch} \rangle \pm \gamma}, \quad (25)$$

with $\gamma = 2, 1, 0$ for pp, pn and nn reactions, respectively. Thus, using Eqs. (21-25) one finds the HSD results for ω_i^* per N+N collision at 158 GeV:

$$\omega_{ch}^* = 2.5, \quad \omega_{-}^* = 1.5, \quad \omega_{+}^* = 1.1. \quad (26)$$

The above arguments are not applicable for central A+A collisions, where a large degree of thermalization is expected. In the limit of $N_P^{proj} = A$ one can take the values

of ω_i^* from the Pb+Pb data or model simulations. In this limit, $\omega_P = \omega_P^{targ}/2 \approx 0$ (see Fig. 4), and thus $\omega_i \approx \omega_i^*$. It has been found that (26) gives a reasonable description of ω_i in the HSD simulations for central Pb+Pb collisions at 158 AGeV. Therefore, one can extrapolate (20) and (26) to all values of N_P^{proj} . This leads to a good agreement for ω_i (20) in the full 4π acceptance with the transport model simulations [45].

The fluctuations of the total hadron multiplicities generated by the transport model dynamics are large, i.e. the ω_i for 4π -acceptance are essentially larger than 1. The main contributions to ω_i come from the second terms in (20), which are due to the fluctuations of N_P^{targ} . These fluctuations of the target nucleon participants presented in Fig. 4 explain both, the large values of ω_i and their strong dependence on N_P^{proj} .

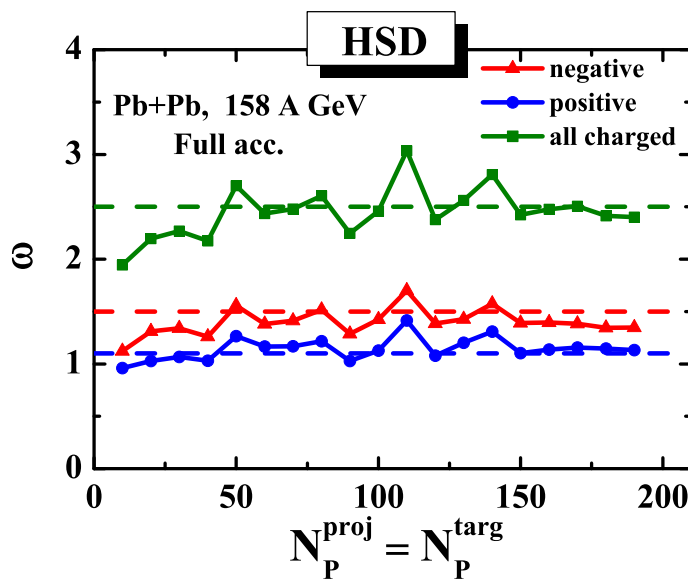


Figure 6. The circles, triangles, and boxes are the results of the HSD simulations for ω_i in full 4π acceptance with $N_P^{targ} = N_P^{proj}$. This condition yields $\omega_P^{targ} = 0$, and Eq. (20) is reduced to $\omega_i = \omega_i^*$. The dashed lines correspond to ω_i^* taken from Eq. (26).

Fig. 6 supports the previous findings. The HSD events with fixed target participant number, $N_P^{targ} = N_P^{proj}$, exhibit much smaller multiplicity fluctuations. This is due to the fact that terms proportional to ω_P^{targ} in (20) do not contribute, ω_i become approximately independent of the number of participants and equal to ω_i^* (26).

3.3. Transparency and Mixing in Nucleus-Nucleus Collisions

Different models of hadron production in relativistic A+A collisions can be divided into three limiting groups: transparency, mixing, and reflection models (see Ref. [49]). The first group assumes that the final longitudinal flows of the hadron production sources related to projectile and target participants follow in the directions of the projectile and target, respectively. One calls this group of models as transparency (T-)models. If the projectile and target flows of hadron production sources are mixed, these models are

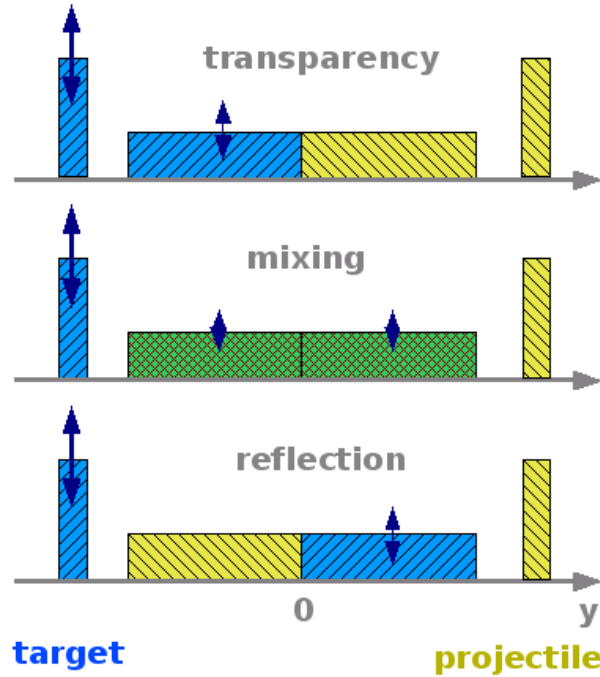


Figure 7. The sketch of the rapidity distributions of the baryon number or the particle production sources (horizontal rectangles) in nucleus-nucleus collisions resulting from the transparency, mixing and reflection models. The spectator nucleons are indicated by the vertical rectangles. In the collisions with a fixed number of projectile spectators only matter related to the target shows significant fluctuations (vertical arrows). See Ref. [49] for more details.

called as mixing (M-)models. Finally, one may assume that the initial flows are reflected in the collision process. The projectile related matter then flows in the direction of the target and the target related matter flows in the direction of the projectile. This class of models corresponds to the reflection (R-)models. The rapidity distributions resulting from the T-, M-, and R-models are sketched in Fig. 7 taken from Ref. [49].

An asymmetry between the projectile and target participants introduced by the experimental selection procedure in a fix target experiment can be used to distinguish between projectile related and target related final state flows of hadron production sources. The multiplicity fluctuations measured in the target momentum hemisphere clearly are larger than those measured in the projectile hemisphere in T-models. The opposite relation is predicted for R-models, whereas for M-models the fluctuations in the projectile and target hemispheres are expected to be the same. Note that there are models which assume the mixing of hadron production sources, however, the transparency of baryon flows, e.g. three-fluid hydrodynamical model [50, 51].

Now the fluctuations of the particle multiplicities in the projectile ($y > 0$) and target ($y < 0$) hemispheres are considered. As one can see from Fig. 4, in samples with $N_P^{proj} = const$ the number of target participants, N_P^{targ} , fluctuates considerably. Of course, this event selection procedure introduces an asymmetry between projectile and

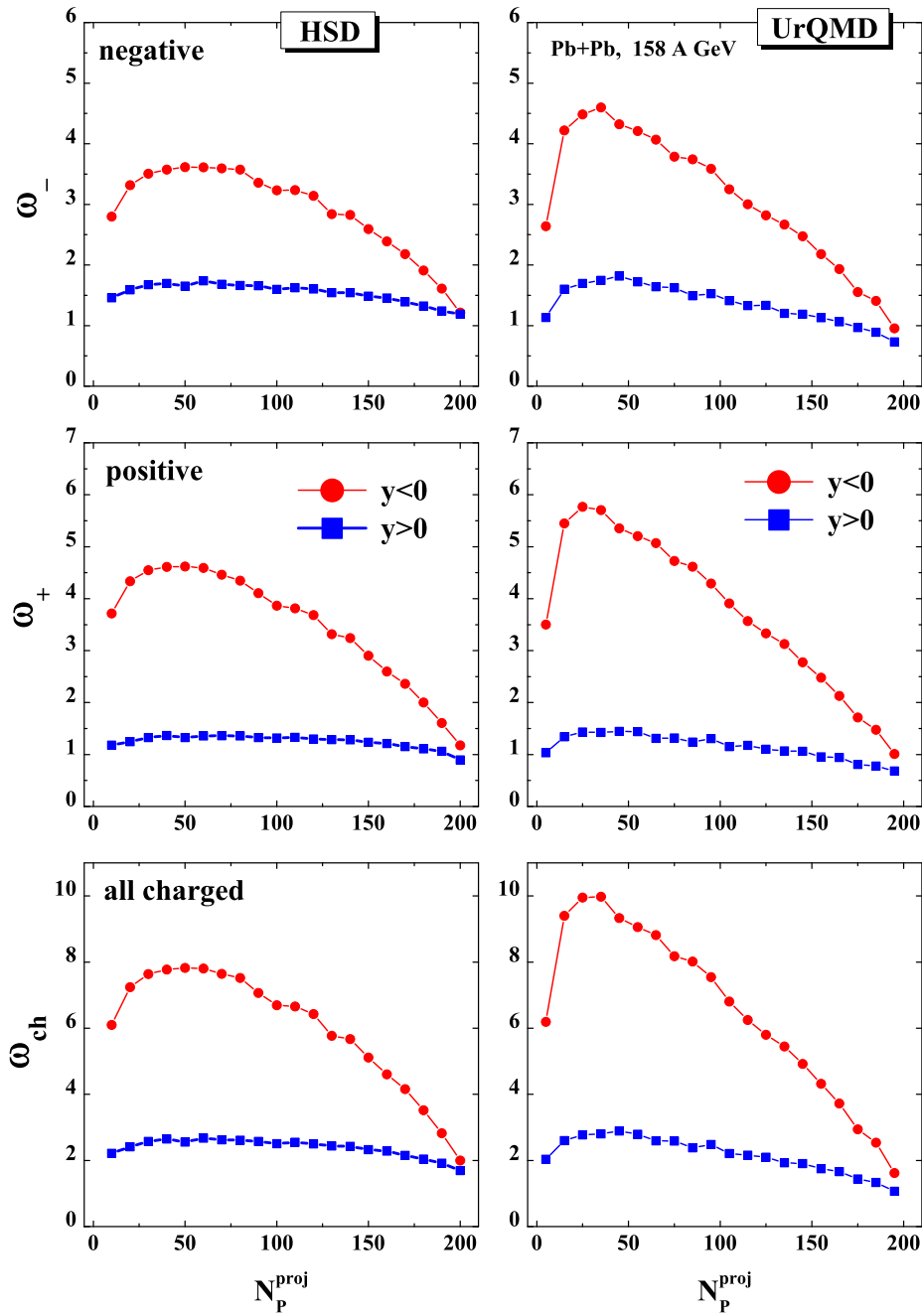


Figure 8. The scaled variances ω_i for the projectile (boxes) and target (circles) hemispheres in the HSD (*left*) and UrQMD (*right*) simulations.

target participants: N_P^{proj} is constant, whereas N_P^{targ} fluctuates. Under this restriction the transport models give very different results for the particle number fluctuations in the projectile and target hemispheres. As clearly seen from Fig. 8 the particle number fluctuations in the target hemispheres are much stronger than those in the projectile hemispheres. There is also a strong N_P^{proj} -dependence of ω_i in the target hemisphere, which is almost absent for the ω_i in the projectile hemisphere. Thus, the fluctuations

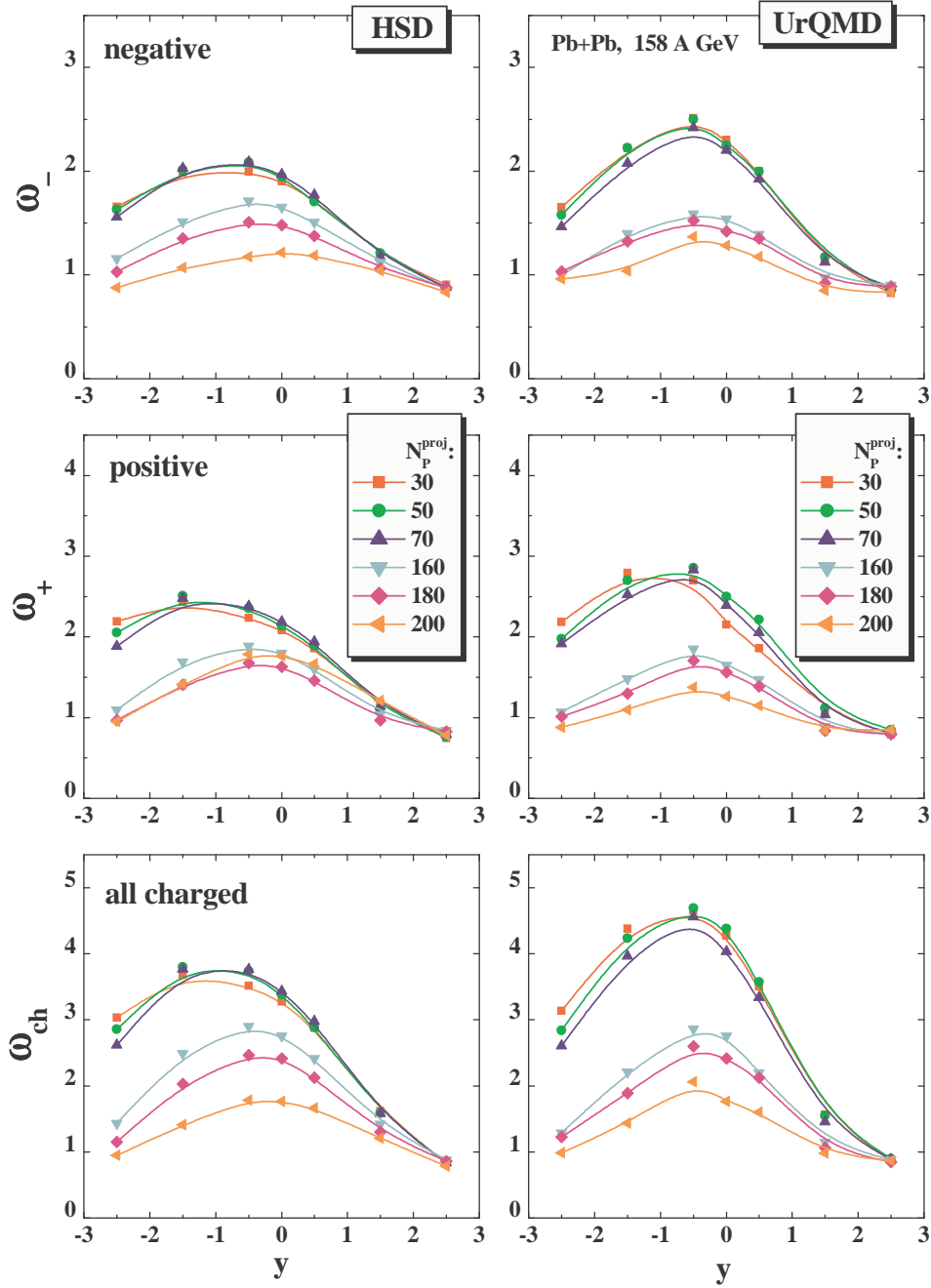


Figure 9. Scaled variances ω_- , ω_+ , and ω_{ch} from the HSD (left) and UrQMD (right) in the rapidity intervals $\Delta y = 1$ around $y = 0, \pm 0.5, \pm 1.5, \pm 2.5$ for different number of projectile participants N_p^{part} .

of N_P^{targ} have a small influence on the final multiplicity fluctuations in the projectile hemisphere, but they contribute very strongly to those in the target hemisphere.

A selection of collisions with a fixed number of N_P^{proj} and fluctuating number of N_P^{targ} means that the projectile and target initial flows are marked in fluctuations [49] in the number of colliding nucleons. The projectile and target related matters in the final

state of collisions can be then distinguished by an analysis of fluctuations of extensive quantities. The analysis of the fluctuations applied to collisions of identical nuclei gives a unique possibility to investigate the flows of particle production sources.

Fig. 9 shows the scaled variances ω_- , ω_+ and ω_{ch} in the HSD and UrQMD simulations as functions of rapidity for different N_P^{proj} values. It is clearly seen that the bias on a fixed number of projectile participants reduces strongly the particle fluctuations in the forward hemisphere, in particular within the NA49 acceptance ($1.1 < y < 2.6$). The fluctuations of the target participant numbers influence strongly the hadron production sources in the target hemispheres. They also contribute to the projectile hemisphere, but this contribution is only important in the rapidity interval $0 < y < 1$, i.e. close to midrapidity. It turns out that this "correlation length" in rapidity, $\Delta y \approx 1$, as seen in Fig. 9, is not large enough to reproduce the data. The large values of ω_i and their strong N_P^{proj} -dependence in the NA49 data (cf. Fig. 5) in the projectile rapidity interval, $1.1 < y < 2.6$, thus demonstrate a significantly larger amount of mixing in peripheral reactions than generated in simple hadron/string transport approaches.

4. Multiplicity Fluctuations in Central Nucleus-Nucleus Collisions

This Section presents the HSD results on the excitation function of the multiplicity fluctuations in central A+A collisions. They will be compared with corresponding results in p+p collisions. Note, that some observables in p+p and A+A collisions are rather close to each other. For example, the charged hadron multiplicity per participating nucleon, $n_{ch} \equiv \langle N_{ch} \rangle / \langle N_P \rangle$, at SPS energies of $20 \div 158$ AGeV are not much different in central Pb+Pb and inelastic p+p collisions [13, 52], $R_{ch} \equiv (n_{ch})_{AA} / (n_{ch})_{pp} = 1 \div 1.5$ ‡. This explains a vitality of the wounded nucleon model (WNM) [48] which treats the final state in A+A collision as the result of independent N+N collisions (see, e.g., Ref. [54] which discusses the recent data [55] on d+Au collisions at the RHIC energies of $\sqrt{s_{NN}} = 200$ GeV). However, the basic concept of the WNM is in a severe conflict with many other data, e.g., with multi-strange baryon production, $R_\Omega \equiv (n_\Omega)_{AA} / (n_\Omega)_{pp} \cong 12.5$ [56] in Pb+Pb at 158 AGeV. The R_Ω enhancement is expected to be even stronger at smaller collision energies. The search for quark-gluon plasma signatures in A+A collisions is usually based on the expectation of a very different behavior of special physical observables in A+A and p+p collisions. Famous examples of QGP signatures are the 'strangeness enhancement', ' J/ψ suppression', and 'jet quenching'. In all these cases one compares a suitably normalized physical quantity in A+A and in p+p reactions at the same collision energy per nucleon.

In general, one can define two groups of hadron observables. The first group includes observables which are rather similar in A+A and p+p collisions, thus, they can be reasonably described within the WNM. The second group consists of A+A observables which are very different from those in p+p collisions. The question arises: are the

‡ Note that $R_{ch} < 1$ at low collision energies. The change in behavior of R_{ch} is discussed in Ref. [53].

multiplicity fluctuations in A+A collisions close to those in p+p reactions, or are they very different? The aim of present Section is to study this question [57].

4.1. Inelastic N+N and Central A+A Collisions

The compilation of p+p data for $\langle N_{ch} \rangle$ and ω_{ch} are taken from Ref. [47] and presented in Fig. 10. The energy dependence can be parameterized by the functions [47]:

$$\langle N_{ch} \rangle \cong -4.2 + 4.69 \left(\frac{\sqrt{s_{NN}}}{\text{GeV}} \right)^{0.31}, \quad \omega_{ch} \cong 0.35 \frac{(\langle N_{ch} \rangle - 1)^2}{\langle N_{ch} \rangle}. \quad (27)$$

At high collision energies the KNO scaling [58] holds which implies that the multiplicity distribution $P(N_{ch})$ behaves as

$$\langle N_{ch} \rangle P(N_{ch}) = \psi(N_{ch}/\langle N_{ch} \rangle)$$

(see also Ref. [59,60]). For $\langle N_{ch} \rangle \gg 1$ it follows,

$$\langle N_{ch}^k \rangle = C_k \langle N_{ch} \rangle^k.$$

In particular, $\omega_{ch} \propto \langle N_{ch} \rangle$ [61] as also seen from the parametrization (27).

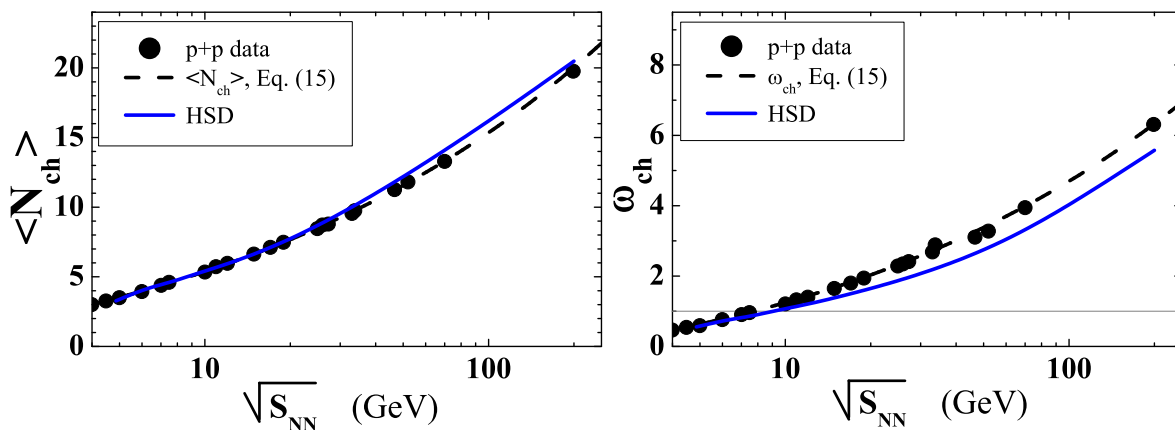


Figure 10. The multiplicity (*left*) and scaled variance (*right*) of all charged hadrons in p+p inelastic collisions as functions of collision energy. The dashed lines correspond to the parametrization (27) from Ref. [47]. The solid lines are the HSD results.

The HSD model description of the p+p data (for p+p reaction this is almost equivalent to the Lund-String model [62]) is shown in Fig. 10 by the solid lines. It gives a good reproduction of the p+p data for $\langle N_{ch} \rangle$, but slightly underestimates ω_{ch} at high collision energies. For negatively and positively charged hadrons the average multiplicities and scaled variances in p+p collisions can be presented in terms of the corresponding quantities for all charged particles, see Eq. (25).

We compare now the central collisions of heavy nuclei and N+N inelastic collisions (21,22) within the HSD model. A small difference between p+p and N+N collisions is only present at the SPS energies and gradually disappears at RHIC energies.

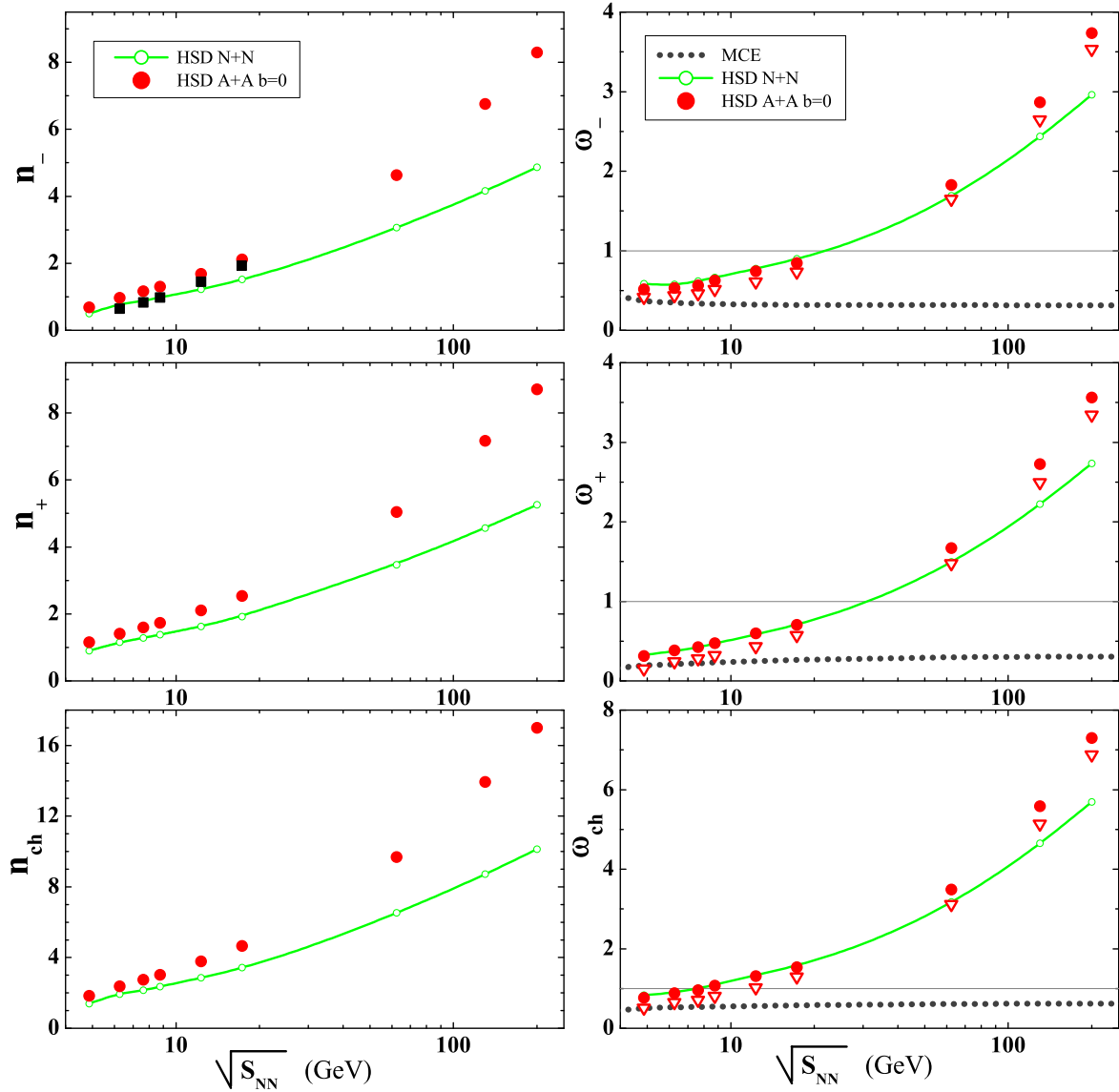


Figure 11. The multiplicities per participant, n_i (*left*), and scaled variances, ω_i (*right*). The solid lines are the HSD results for N+N collisions according to (21). The full circles are the HSD results for central A+A collisions for zero impact parameter, $b = 0$. The full squares for n_- are the NA49 data [13, 52] for $(\langle\pi^- \rangle + \langle K^- \rangle) / \langle N_P \rangle$ in the samples of 7% most central Pb+Pb collisions. The HSD results for ω_i after the subtraction of the contributions $\Delta\omega_i = n_i\omega_P$ are shown by open triangles. The dotted lines are the MCE HG model results for ω_i [63]. The HG parameters correspond to the chemical freeze-out conditions found from fitting the hadron yields.

In Fig. 11 the HSD model results are shown for the multiplicities per participating nucleons, $n_i = \langle N_i \rangle / \langle N_P \rangle$, and for the scaled variances, ω_i , in central collisions (zero impact parameter, $b = 0$) of Pb+Pb at $E_{lab} = 10, 20, 30, 40, 80, 158$ AGeV and Au+Au at $\sqrt{s_{NN}} = 62, 130, 200$ GeV. From Fig. 11 one concludes that the HSD results for the scaled variances in central A+A collisions are close to those in inelastic N+N collisions. The participant number fluctuations are found to be rather small for central A+A collisions

with zero impact parameter $b = 0$. For example, in Pb+Pb collisions with $b = 0$ at 158 AGeV the mean number of participants is $\langle N_P \rangle \cong 392$, and the scaled variance is $\omega_P \cong 0.055$. The additional fluctuations, $\Delta\omega_i$, of i th hadrons due to participant number fluctuations can be estimated as, $\Delta\omega_i = n_i \omega_P$. The HSD results for ω_i after subtraction of the contributions $\Delta\omega_i$ are shown in Fig. 11 by open triangles. These contributions to ω_i due to participant number fluctuations appear to be rather small at $b = 0$, and they do not explain the (positive) difference, $\omega_i(\text{AA}) - \omega_i(\text{NN})$ seen in Fig. 11 at $\sqrt{s_{NN}} = 200$ GeV.

On the other hand in the statistical model the scaled variances $\omega_i = 1$ for the ideal Boltzmann gas in the grand canonical ensemble (GCE). The deviations of ω_i from unity in the hadron-resonance gas (HG) model stem from Bose and Fermi statistics, resonance decays, and exactly enforced conservations laws within the canonical ensemble (CE) or micro-canonical ensemble (MCE) [63–65]. Note that the statistical model gives no predictions for the energy dependence of hadron multiplicities. All yields are proportional to the system volume V which is a free model parameter fitted to the multiplicity data at each collision energy. However, the statistical model does predict the scaled variances ω_i as they become to be independent of the system volume for large systems. In Fig. 11 the scaled variances ω_i calculated within the MCE HG model along the chemical freeze-out line (see Ref. [63] for details) are presented by the dotted lines: ω_i reach their asymptotic values at RHIC energies, $\omega_{\pm}(\text{MCE}) \cong 0.3$ and $\omega_{ch}(\text{MCE}) \cong 0.6$. The corresponding results in the GCE and CE are the following: $\omega_{\pm}(\text{GCE}) \cong 1.2$ and $\omega_{ch}(\text{GCE}) \cong 1.6$, $\omega_{\pm}(\text{CE}) \cong 0.8$ and $\omega_{ch}(\text{CE}) \cong 1.6$. The HSD results for ω_i in central A+A collisions are very different. They remain close to the corresponding values in p+p collisions and, thus, increase with collision energy as $\omega_i \propto n_i$. One observes no indication for ‘thermalization’ of fluctuations in the HSD results. This is especially seen for RHIC energies: $\omega_i(\text{HSD})/\omega_i(\text{MCE}) \geq 10$ at $\sqrt{s_{NN}} = 200$ GeV.

4.2. Comparison with the NA49 Data

The fluctuations of the number of nucleon participants correspond to volume fluctuations, hence, they translate directly to the final multiplicity fluctuations. To avoid these ‘trivial’ fluctuations, one has to select a sample of very central, $\leq 1\%$, collisions. Such a rigid centrality selection has been recently done for the NA49 data [66] by fixing the number of projectile participants close to its maximal value $N_P^{proj} = A$.

The HG model was compared with the NA49 data [66] for the sample of 1% most central collisions at the SPS energies, $20 \div 158$ AGeV in Ref. [63]. It was found that the MCE results for ω_{\pm} are very close to the data, they are shown by the dashed lines in Fig. 12. The NA49 acceptance probabilities for positively and negatively charged hadrons are approximately equal, and their numerical values are: $q = 0.038, 0.063, 0.085, 0.131, 0.163$, at the SPS energies of 20, 30, 40, 80, 158 AGeV, respectively. In the statistical model the scaled variances ω_{\pm}^{acc} for the accepted particles are calculated from ω_{\pm} in the full space according to the acceptance scaling formulae (see Ref. [63] for

details):

$$\omega_{\pm}^{acc} = 1 - q + q \omega_{\pm}. \quad (28)$$

Note that the energy dependence of ω_{\pm}^{acc} seen in Fig. 12 is strongly influenced by an increase with energy of the acceptance parameter q : only about 4% of the hadrons are detected at 20 AGeV and 16% at 158 AGeV.

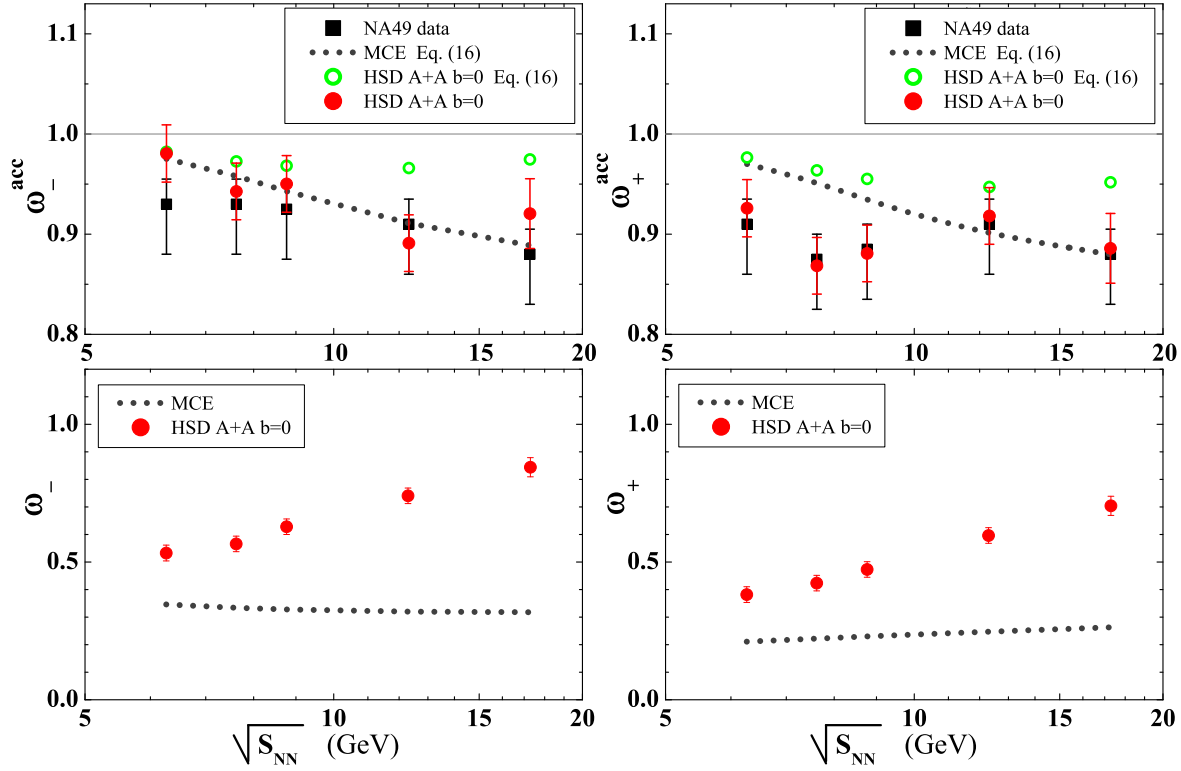


Figure 12. *Upper panel.* The scaled variances ω_{\pm}^{acc} for central Pb+Pb collisions. The squares with error bars are the NA49 data for 1% most central collisions [66]. The dotted lines show the MCE HG model results calculated from full 4π scaled variances using (28). The full circles present the HSD results in Pb+Pb collisions for $b = 0$ with the NA49 experimental acceptance conditions, while the open circles are obtained from the 4π HSD scaled variances using (28). *Lower panel.* The MCE HG (dotted line) and HSD (full circles, the same as in Fig. 11) for the 4π scaled variances ω_{\pm} at the SPS energies.

The comparison of the HSD results for central Pb+Pb collisions (zero impact parameter, $b = 0$) with the NA49 data of 1% most central collisions, selected by the number of projectile spectators, is presented in Fig. 12. It demonstrates a good agreement of the HSD results with the NA49 data. There are also no essential differences between the MCE HG model and the HSD transport model results. Several comments are needed at this point. The HSD results within the NA49 acceptance demonstrate that the acceptance scaling formulae (28) is violated. The straightforward calculations (full circles in Fig. 12) lead to smaller values of ω_{\pm}^{acc} than those obtained with the

acceptance scaling formulae (28) (open circles in Fig. 12). This difference may lead to a 10% effect in ω_{\pm}^{acc} for the NA49 acceptance conditions. Thus, the MCE results for ω_{\pm}^{acc} may also be about 10% smaller than those obtained from (28) and shown in the upper panel of Fig. 12. The lower panel of Fig. 12 demonstrates that the MCE and HSD results for ω_{\pm} at the lowest SPS energy 20 AGeV are ‘occasionally’ rather close to each other. They both are also close to ω_{\pm} in p+p collisions. The HSD scaled variances ω_i increase with collision energy. In contrast, the MCE ω_i values remain approximately constant. The ratio of the HSD to MCE values of ω_{\pm} reaches about the factor of 2 at the highest SPS energy 158 AGeV. It becomes a factor of 10 at the top RHIC energy $\sqrt{s_{NN}} = 200$ GeV. However, the rigid centrality selection is absent for the available RHIC fluctuation data. Due to this reason the participant number fluctuations give a dominant contribution to ω_i . On the other hand, for the SPS data the small values of the acceptance, $q = 0.04 \div 0.16$, and 10% possible ambiguities coming from (28) almost mask the difference between the HSD and MCE results (Fig. 12, upper panel).

Note that the scaled variance is a non-trivial function of the selected phase-space. This issue has been addressed in Ref. [67]. In order to study the dependence of scaled variance on rapidity, 12 different rapidity intervals have been constructed in such a way that the mean multiplicity in each interval is the same. If the scaled variance would follow the acceptance scaling formula (28), the scaled variance would be the same in each interval. However, as it has been shown in Ref. [67], the scaled variance is much higher near midrapidity than in forward and backward rapidities, which is illustrated in Fig. 13 taken from Ref. [67].

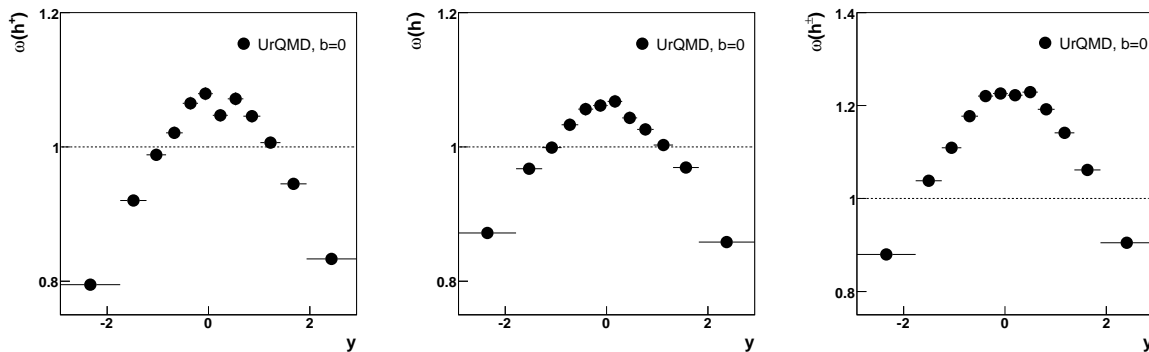


Figure 13. Rapidity dependence of scaled variance in UrQMD simulation performed in full acceptance of positive (top), negative (middle) and all charged (bottom) hadrons in central Pb+Pb collisions at 158 AGeV. The rapidity bins are constructed in such a way that the mean multiplicity in each bin is the same. The figure is taken from Ref. [67].

The transverse momentum dependence of scaled variance is shown in Fig. 14 for the full longitudinal phase-space and for a midrapidity and a forward rapidity interval. The scaled variance decreases with increasing transverse momentum for the full acceptance and at forward rapidity. At midrapidity it stays approximately constant. The decrease

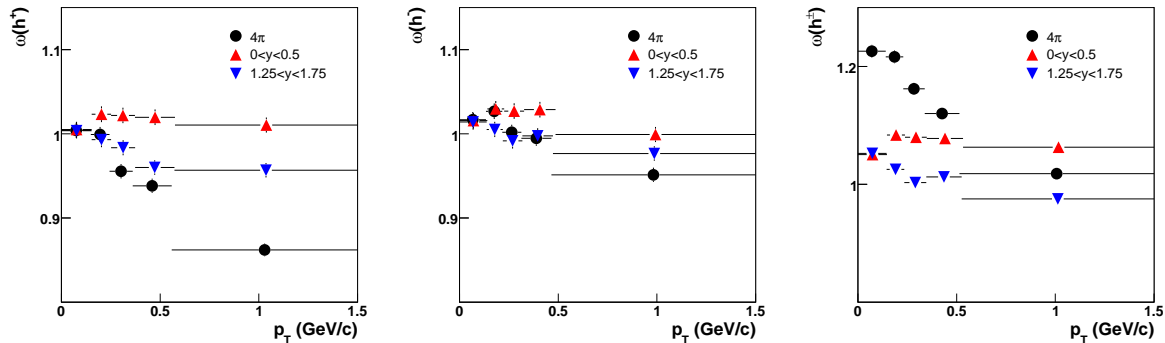


Figure 14. (Color online) Transverse momentum dependence of multiplicity fluctuations of positively (top), negatively (middle) and all charged hadrons (bottom) for all rapidities, $0 < y < 0.5$ and $1.25 < y < 1.75$. The transverse momentum bins are constructed in such a way that the mean multiplicity in each bin is the same. The figure is taken from Ref. [67].

of scaled variance is stronger for positively charged hadrons than for negatively charged ones because the protons, which have smaller relative fluctuations due to the large number of protons which enter the collision, have a larger mean transverse momentum.

A similar effect of decreasing fluctuations for larger rapidities and transverse momenta is observed as a result of energy- and momentum conservation in a hadron gas model using the micro-canonical ensemble [68]. It costs more energy to create a particle with high momentum, therefore their number is expected to fluctuate less.

5. Dependence on Energy and Atomic Number

An ambitious experimental program for a search of the QCD critical point has been started by the NA61 Collaboration at the SPS [5,30]. The program includes a variation in the atomic mass number A of the colliding nuclei as well as an energy scan. This allows to scan the phase diagram in the plane of temperature T and baryon chemical potential μ_B near the critical point as argued in Ref. [5,30] and shown in Fig. 15 which is taken from Ref. [69]. One expects to ‘locate’ the position of the critical point by studying its ‘fluctuation signals’. High statistics multiplicity fluctuation data will be taken for p+p, C+C, S+S, In+In, and Pb+Pb collisions at bombarding energies of $E_{lab}=10, 20, 30, 40, 80,$ and 158 AGeV.

The aim of the Section is to present the results of studies on the energy and system size dependence of event-by-event multiplicity fluctuations within the HSD and UrQMD microscopic transport approaches. Our study thus is in full correspondence to the experimental program of the NA61 Collaboration [5,30].

The QCD critical point is expected to be experimentally seen as a non-monotonic dependence of the multiplicity fluctuations, i.e. a specific combination of atomic mass number A and bombarding energy E_{lab} could move the chemical freeze-out of the system close to the critical point and show a ‘spike’ in the multiplicity fluctuations. Since HSD

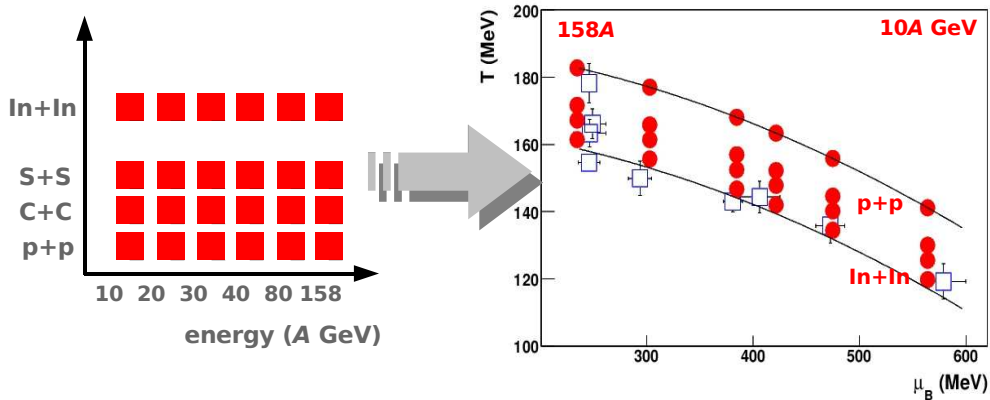


Figure 15. Left: The data sets on central A+A collisions planned to be registered by NA61 in a search for the critical point of strongly interacting matter and a study of the properties of the onset of deconfinement. Right: Hypothetical positions of the chemical freeze-out points of the reactions (In+In, S+S, C+C and p+p from bottom to top at 158A, 80A, 40A, 30A, 20A and 10A GeV from left to right) to be studied by NA61 in the (temperature)-(baryon-chemical potential) plane are shown by full dots. The open squares show the existing Pb+Pb NA49 data.

and UrQMD do not include explicitly a phase transition from a hadronic to a partonic phase, a clear suggestion for the location of the critical point can not be made – it is beyond the scope of such hadron-string models. However, this study might be helpful in the interpretation of the upcoming experimental data since it will allow to subtract simple dynamical and geometrical effects from the expected QGP signal. The deviations of the future experimental data from the HSD and UrQMD predictions may be considered as an indication for the critical point signals.

Theoretical estimates give about 10% increase of the multiplicity fluctuations due to the critical point [28, 70, 71]. It is large enough to be observed experimentally within the statistics of NA61 [5, 30]. To achieve this goal, it is necessary to have a control on other possible sources of fluctuations. One of such sources is the fluctuation of the number of nucleon participants. It has been shown in Section 3 that these fluctuations give a dominant contribution to hadron multiplicity fluctuations in A+A collisions. It was demonstrated that one can suppress the participant number fluctuations by selecting most central A+A collisions. That's why the NA61 Collaboration plans to measure central collisions of light and intermediate ions instead of peripheral Pb+Pb collisions. It is important to stress, that the conditions for the centrality selection in the measurement of fluctuations are much more stringent than those for mean multiplicity measurements.

5.1. Why Does One Need Central Collisions of Light Ions?

To minimize the event-by-event fluctuations of the number of nucleon participants in measuring the multiplicity fluctuations the NA49 Collaboration has been trying to fix

N_P^{proj} in Pb+Pb collisions. Samples of collisions with a fixed number of projectile spectators, $N_S^{proj} = const$ (and thus a fixed number of projectile participants, N_P^{proj}), have been selected. A similar centrality selection is expected to be implemented in the NA61 experiment.

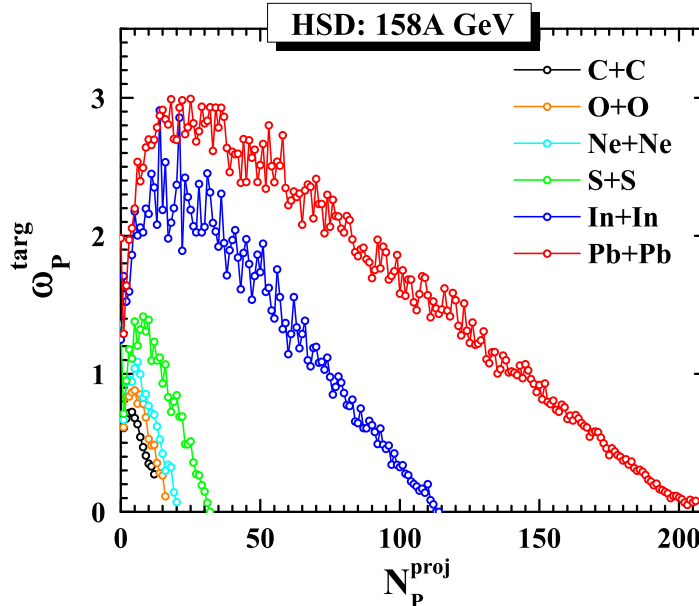


Figure 16. The scaled variance ω_P^{targ} for the fluctuations of the number of target participants, N_P^{targ} . The HSD simulations of ω_P^{targ} as a function of N_P^{proj} are shown for different colliding nuclei, In+In, S+S, Ne+Ne, O+O and C+C at $E_{lab}=158$ AGeV.

Fig. 16 presents the HSD scaled variances ω_P^{targ} for C+C, O+O, Ne+Ne, S+S, In+In, and Pb+Pb collisions at 158 AGeV as a function of N_P^{proj} . The fluctuations of N_P^{targ} are quite strong for mid-peripheral reactions with $N_P^{proj} = 20 \div 30$ and negligible for the most central collisions. A vanishing of $\omega_P^{targ} \cong 0$ at $N_P^{proj} \cong A$ does not, however, show up in collisions of light nuclei (from C to S). Even for the maximal values of $N_P^{proj} = A$ the fluctuations ω_P^{targ} do not vanish and increase with decreasing atomic mass number A . For example in C+C collisions for $N_P^{proj} = A = 12$ the number of participants from the target still fluctuates and the scaled variance amounts to $\omega_P^{targ} \cong 0.25$. Some combination of the system size N_P and collision energy E_{lab} might move the chemical freeze-out point close the QCD critical point. One could then expect an increase of multiplicity fluctuations in comparison to their ‘background values’.

Why does one need central collisions of light and intermediate ions instead of studying peripheral Pb+Pb collisions for a search of the critical point? Fig. 16 explains this issue. At fixed N_P^{proj} the average total number of participants, $N_P \equiv N_P^{proj} + N_P^{targ}$, is equal to $\langle N_P \rangle \cong 2N_P^{proj}$, and, thus, it fluctuates as $\omega_P = 0.5\omega_P^{targ}$. Then, for example, the value of $N_P^{proj} \cong 30$ corresponds to almost zero participant number fluctuations, $\omega_P \cong 0$, in S+S collisions while ω_P becomes large and is close to 1 and 1.5 for In+In and Pb+Pb, respectively. Even if N_P^{proj} is fixed exactly, the sample of the peripheral collision events

in the heavy-ion case contains large fluctuations of the participant number: this would ‘mask’ the critical point signals. As also seen in Fig. 16 (*right*), the picture becomes actually more complicated if the atomic mass number A is too small. In this case, the number of participants from a target starts to fluctuate significantly even for the largest and fixed value of $N_P^{proj} = A$.

5.2. Multiplicity Fluctuations at Zero Impact Parameter

The importance of a selection of the most central collisions for studies of hadron multiplicity fluctuations has been stressed in the previous sections. Due to its convenience in theoretical studies (e.g., in hydrodynamical models) one commonly uses the condition on impact parameter b for the selection of the ‘most central’ collisions in model calculations. However, the number of participant even at $b = 0$ is not strictly fixed and fluctuates according to some distributions. It should be also stressed that the conditions $b < b_{max}$ can not be fixed experimentally since the impact parameter itself can not be measured in a straightforward way. Actually, in experiments one accounts for the 1%, 2% etc. most central events selected by the measurement of spectators in the Veto calorimeter, which corresponds to the event class with the largest N_P^{proj} . As it will be demonstrated below the multiplicity fluctuations are very sensitive to the centrality selection criteria. In particular, the transport model results for $b = 0$ and for 1% events with the largest N_P^{proj} are rather different (see below).

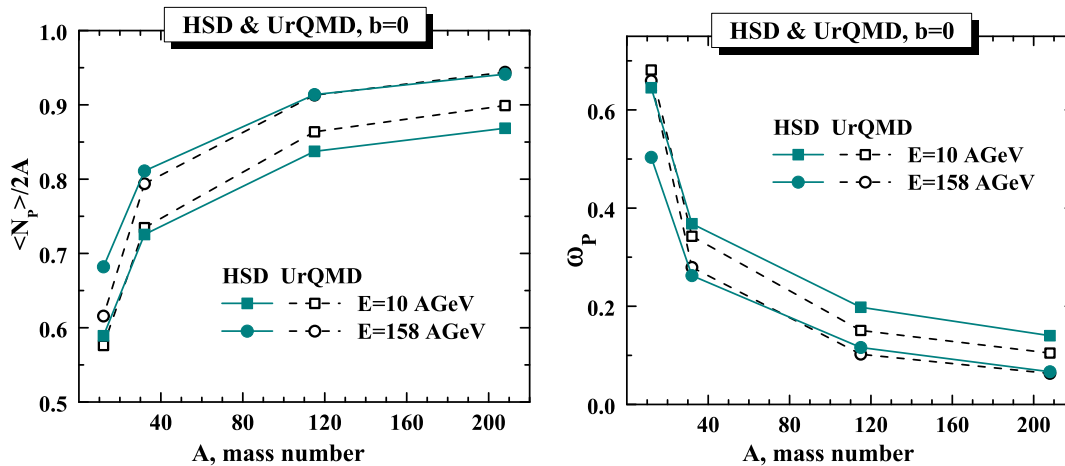


Figure 17. *Left:* Mean $\langle N_P \rangle$, divided by the maximum number of participants $2A$ in events with $b = 0$ for different nuclei at collision energies $E_{lab}=10$ and 158 AGeV. *Right:* The scaled variance ω_P in events with $b = 0$ for different nuclei at collision energies $E_{lab}=10$ and 158 AGeV.

Let’s start with the $b = 0$ centrality selection criterium. First, we estimate the average number of participants, $\langle N_P \rangle$, and the scaled variances of its fluctuations, ω_P , in $A + A$ collision events which satisfy the $b = 0$ condition. The left panel in Fig. 17 shows the ratio, $\langle N_P \rangle / 2A$, in $A + A$ collisions with $b = 0$ for different nuclei at collision

energies $E_{lab} = 10$ and 158 AGeV. Both transport models (HSD and UrQMD) show a monotonous increase of $\langle N_P \rangle / 2A$ with collision energy for all nuclei in the energy range $10 \div 158$ AGeV (Fig. 17, *left*). Correspondingly, the fluctuations of the number of participants ω_P for all nuclei become smaller with increasing collision energy (Fig. 17, *right*). As seen from Fig. 17 (*left*) about 90% of all nucleons are participants for Pb+Pb collisions with $b = 0$. This number becomes essentially smaller, about 60-70%, for C+C collisions. One can therefore expect that participant number fluctuations at $b = 0$ are small for heavy nuclei but strongly increase for light systems. This is demonstrated in Fig. 17 (*right*): ω_P is about $0.1 \div 0.2$ in Pb+Pb and In+In but becomes much larger, $0.5 \div 0.7$, in C+C collisions.

One can conclude that the condition $b = 0$ corresponds to ‘most central’ $A + A$ collisions only for nuclei with large atomic mass number (In and Pb). In this case the average number of participants is close to its maximum value and its fluctuations are rather small. However, in the studies of event-by-event multiplicity fluctuations in the collisions of light nuclei (C and S) the criterium $b = 0$ is far from selecting the ‘most central’ $A + A$ collisions.

Results of HSD and UrQMD transport model calculations for the scaled variance of negative, ω_- , positive, ω_+ , and all charged, ω_{ch} , hadrons are shown in Fig. 18 at different collision energies, $E_{lab} = 10, 20, 30, 40, 80, 158$ AGeV, and for different colliding nuclei, C+C, S+S, In+In, Pb+Pb. The transport model results correspond to collision events for zero impact parameter, $b = 0$. To make the picture more complete, the transport model results for inelastic p+p collisions are shown too, for reference. Note that the proton spectators are not accounted for in the calculation of N_+ and N_{ch} . Thus, proton spectators do not contribute to ω_+ and ω_{ch} .

One sees a monotonic dependence of the multiplicity fluctuations on both E_{lab} and A : the scaled variances ω_- , ω_+ , and ω_{ch} increase with E_{lab} and decrease with A . The results for p+p collisions are different from those for light ions. Note that within HSD a detailed comparison of the multiplicity fluctuations in N+N inelastic collisions and $b = 0$ heavy-ion collisions (Pb+Pb and Au+Au), including the energy dependence up to $\sqrt{s_{NN}} = 200$ GeV, has been presented in Sec. 4 and in Refs. [57,67]. Fig. 18 corresponds to the full 4π acceptance.

The combination of the multiplicity fluctuations in elementary N+N collisions and fluctuations of the number of nucleon participants explains the main features of hadron multiplicity fluctuations in $A + A$ collisions. In particular, within the MIS (20) one obtains the dependence on collision energy and atomic mass number shown in Fig. 18. The value of n_i in Eq. (20) is the average number of i 'th particles per participant, $n_i = \langle N_i \rangle / \langle N_P \rangle$, and ω_P equals the scaled variance for the number of nucleon participants. The N+N collisions define the fluctuations $\omega_i^* = \omega_i^{NN}$ from a single source.

In Fig. 19 the HSD results for ω_i in $A + A$ collisions at $b = 0$ are compared to the Eq. (20). One concludes that the transport model results for the multiplicity fluctuations are in qualitative agreement with MIS (20). Both n_i and ω_i^* increase strongly with

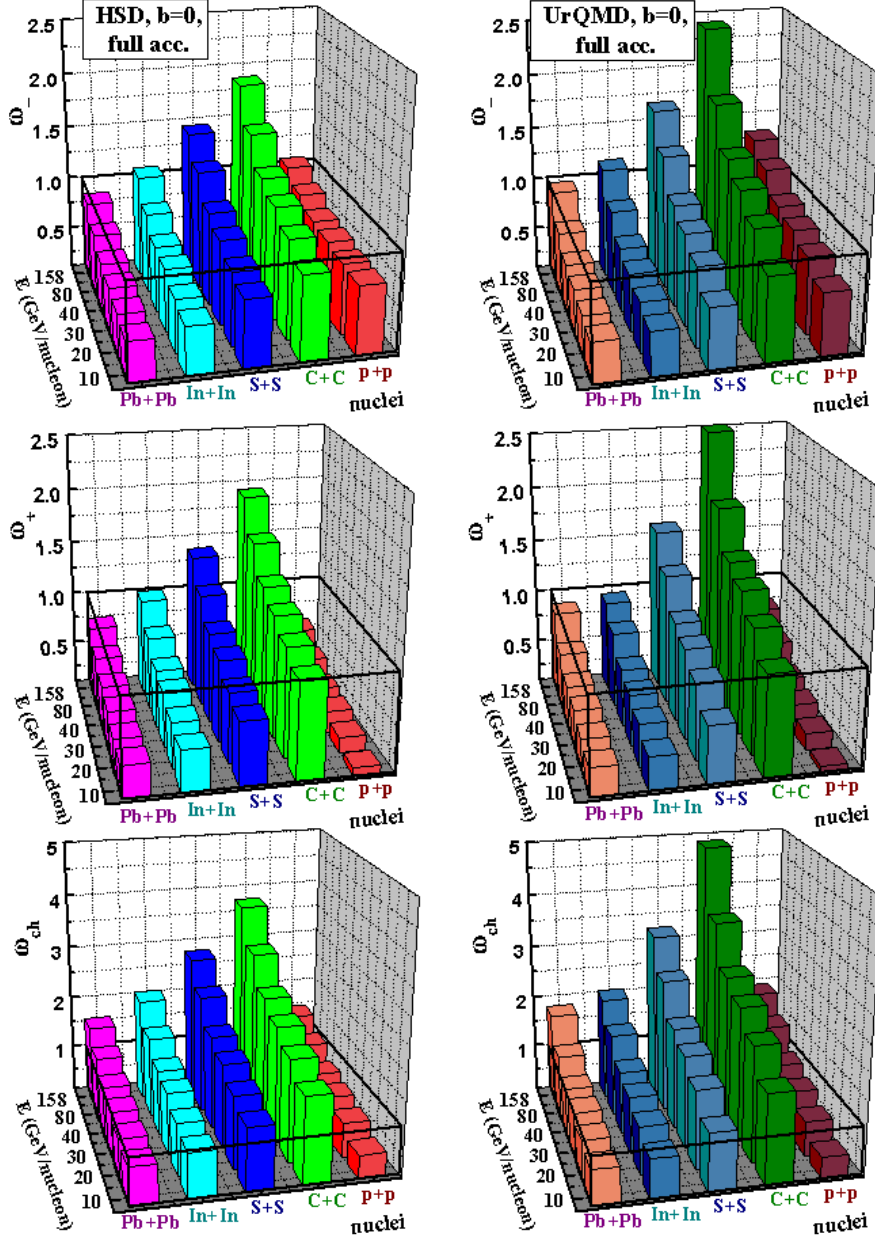


Figure 18. The results of HSD (*left*) and UrQMD (*right*) simulations for ω_- (top panel), ω_+ (middle panel), and ω_{ch} (lower panel) in p+p and central C+C, S+S, In+In, Pb+Pb collisions at $E_{lab} = 10, 20, 30, 40, 80, 158$ AGeV. The condition $b = 0$ is used here as a criterium for centrality selection. There are no cuts in acceptance.

collision energy as seen from Fig. 10. This explains, due to Eq. (20), the monotonous increase with energy of the scaled variances ω_i in A+A collisions at $b = 0$ seen in Fig. 18. Note that ω_P at $b = 0$ decreases with collision energy as shown in Fig. 17, *right*. This, however, does not compensate a strong increase of both n_i and ω_i^* . The atomic mass number dependence of the scaled variances ω_i in A + A collisions with $b = 0$ follows from the A-dependence of ω_P . Fig. 17 (*right*) demonstrates a strong increase of ω_P for

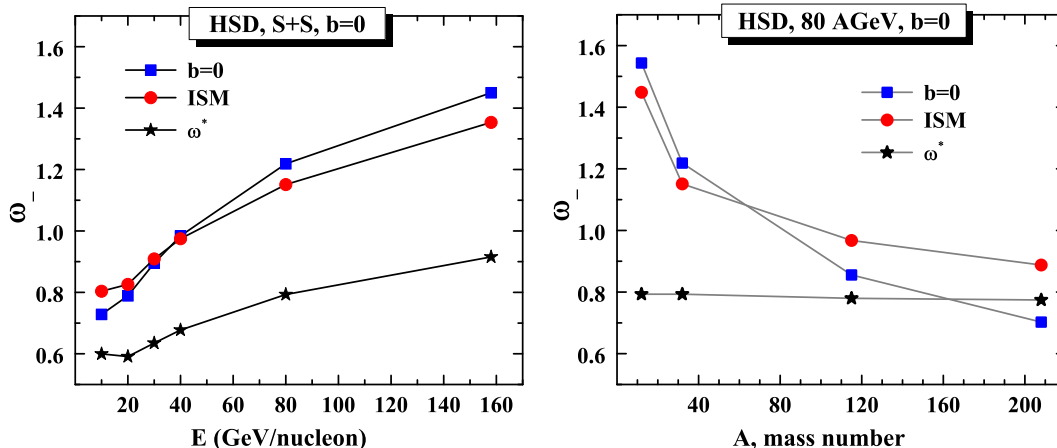


Figure 19. The *left* panel illustrates the energy dependence of ω_- in S+S collisions at $b = 0$ in the full 4π acceptance, the *right* panel – the ω_- dependence on atomic mass number at $E_{lab}=80$ AGeV. The HSD results are shown by the squares while the circles correspond to the MIS (20). The stars show the first term, ω^* , in the r.h.s. of Eq. (20) – the scaled variance for negative hadrons in N+N collisions. The values of ω_-^* , n_i , and ω_P are calculated within HSD.

light nuclei. This, due to (20), is transformed to the corresponding behavior of ω_i seen in Fig. 18.

5.3. Centrality Trigger with the Number of Projectile Participants

In this subsection the centrality selection procedure by fixing the number of projectile participants N_P^{proj} is considered. This corresponds to the real situation of A+A collisions in fixed target experiments. As a first step one simulates in HSD and UrQMD the minimal bias events and calculate the event distribution over the number of participants N_{part} . Then, one selects 1% most central collisions which correspond to the largest values of N_P^{proj} . In such a sample of A+A collisions events with largest N_P^{proj} from different impact parameters can contribute. After that one calculates the values of ω_P in these samples. Note, that even for a fixed number of N_P^{proj} the number of target participants N_P^{targ} fluctuates. Thus, the total number of participants $N_P = N_P^{targ} + N_P^{proj}$ fluctuates, too. In our 1% sample, both N_P^{targ} and N_P^{proj} fluctuate. Besides there are correlations between N_P^{targ} and N_P^{proj} .

Fig. 20 shows the ratio $\langle N_P \rangle / 2A$ and the scaled variance, ω_P , for 1% most central collisions selected by the largest values of N_P^{proj} . These results are compared with those for the $b = 0$ centrality selection. For heavy nuclei, like In and Pb, one finds no essential differences between these two criteria of centrality selection. However, the 1% centrality trigger defined by the largest values of N_P^{proj} looks much more rigid for light ions (S and C). In this case the ratio $\langle N_P \rangle / 2A$ is larger, and ω_P is essentially smaller than for the criterion $b = 0$. As a result the 1% centrality trigger by the largest values of N_P^{proj} leads to a rather weak A -dependence of ω_P .

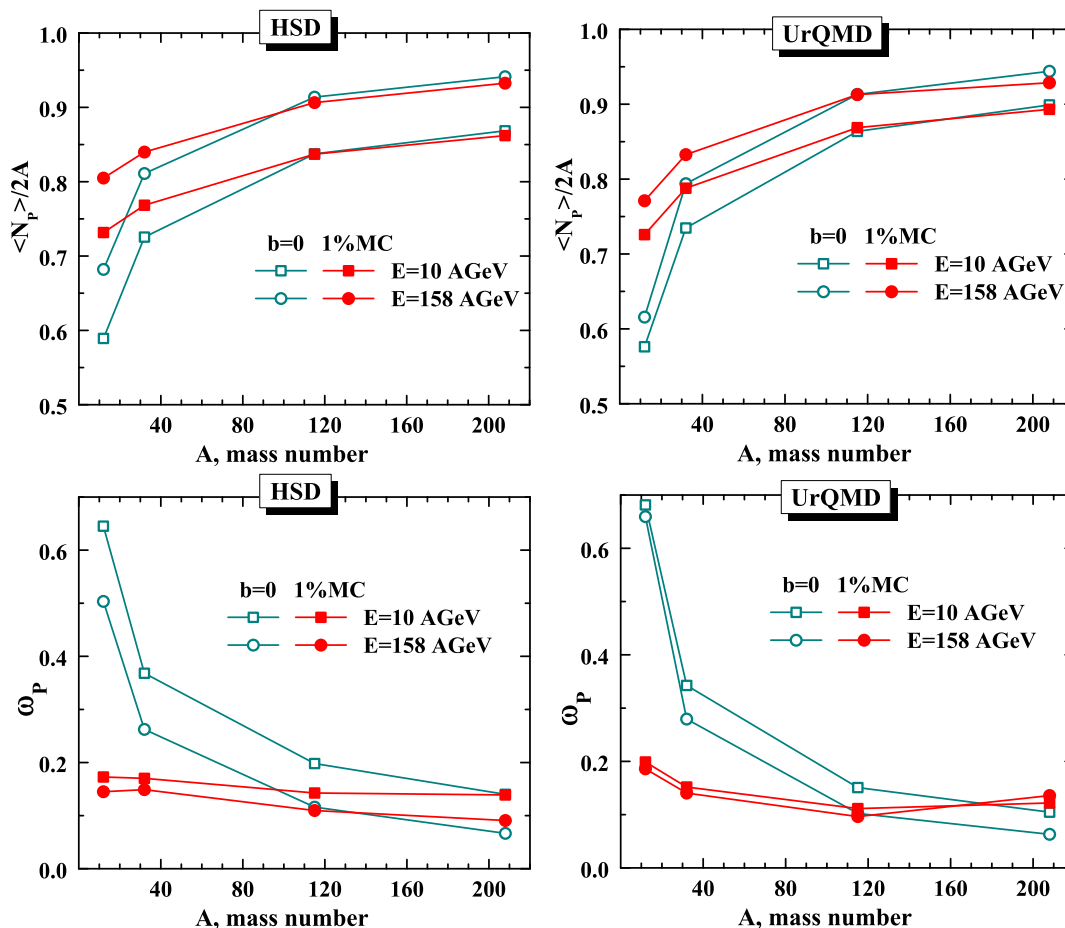


Figure 20. The HSD (*left*) and UrQMD (*right*) results for the ratio $\langle N_P \rangle / 2A$ (the upper panel) and the scaled variance of the participant number fluctuations, ω_P (the lower panel), for the 1% most central collisions selected by the largest values of N_P^{proj} (full symbols), for different nuclei at collision energies $E_{lab}=10$ and 158 AGeV. The open symbols present the results of Fig. 17 (*right*) for $b = 0$.

Some comments are appropriate at this point. Let's define the centrality $c(N)$ as a percentage of events with a multiplicity larger than N (this can be the number of produced hadrons, number of participants, etc.). It was argued in Ref. [72] that a selection of $c(N)$ of most central $A + A$ collisions is equivalent to restricting the impact parameter, $b < b(N)$, with,

$$b(N) = \sqrt{\frac{\sigma_{inel}}{\pi}} c(N), \quad (29)$$

where σ_{inel} is the total inelastic $A+A$ cross section. Thus, the centrality criterion by the multiplicity N is equivalent to the geometrical criterion by the impact parameter b . Moreover, the result (29) does not depend on the specific observable N used to define the c -percentage of most central $A+A$ collisions. The result (29) should be valid for any observable N which is a monotonic function of b . Therefore, the relation (29) reduces any centrality selection to the geometrical one. This result was obtained in Ref. [72] by

neglecting the fluctuations of multiplicity N at a given value of b . This is valid if c is not too small and the colliding nuclei are not too light. In the sample of A+A events with 1% of largest N_P^{proj} , the relation (29) can not be applied for S+S and C+C collisions.

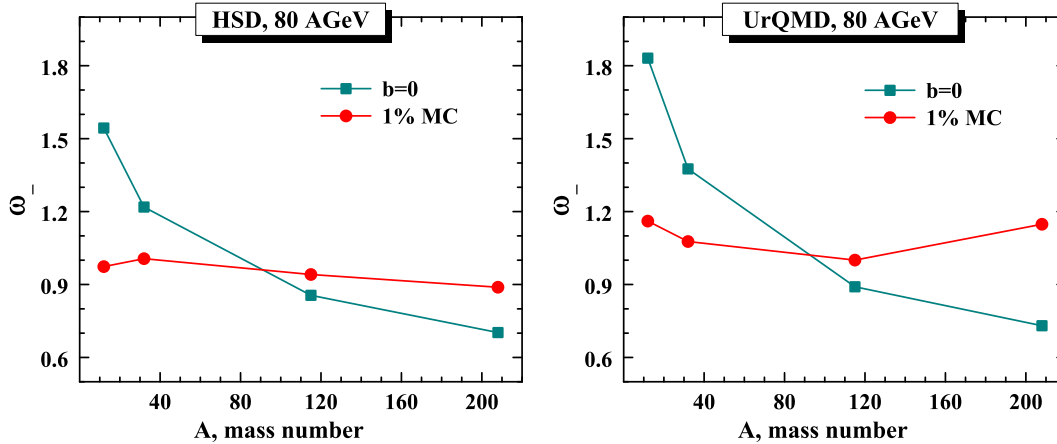


Figure 21. The dependence of ω_- on atomic mass number at $E_{lab}=80$ AGeV for the HSD (left) and UrQMD (left) simulations. The squares correspond to $b = 0$, and circles to 1% largest N_P^{proj} .

Fig. 21 shows a comparison of the A-dependence of ω_- in the transport models for two different samples of the collision events: for $b = 0$ and for the 1% of events with largest N_P^{proj} values. One can see that the multiplicity fluctuations are rather different in these two samples. Moreover, these differences are in the opposite directions for heavy nuclei and for light nuclei. For light nuclei, ω_- is essentially smaller in the 1% sample with largest N_P^{proj} values, whereas for heavy nuclei the smaller fluctuations correspond to $b = 0$ events. Note that in the 1% sample with largest N_P^{proj} values the A-dependence of multiplicity fluctuations becomes much weaker. In this case a strong increase of the multiplicity fluctuations for light nuclei, seen for $b = 0$, disappears.

For the 1% most central A + A collision events - selected by the largest values of N_P^{proj} - the HSD multiplicity fluctuations are shown in Fig. 22 and Fig. 23. For light nuclei (S and C) the multiplicity fluctuations in the samples of 1% most central collisions are smaller than in the $b = 0$ selection and the atomic mass number dependencies become less pronounced (compare Fig. 22 and Fig. 18). This is because the participant number fluctuations ω_P have now essentially smaller A-dependence, as seen in Fig. 20.

Fig. 18 shows that both HSD and UrQMD predict a monotonic dependence of the charge particle multiplicity with energy. So, the hadronic ‘background’ for the NA61 experiments is expected to be a smooth monotonic function of beam energy.

The event-by-event observables show a higher sensitivity to the initial nucleon density distribution than the standard single particle observables [73]. A sensitivity of the A-dependence of ω_{ch} to these details of the models indicates a necessity for further studies of the initializations of the nuclei in transport model approaches. This becomes important for the theoretical interpretation of future experimental data on

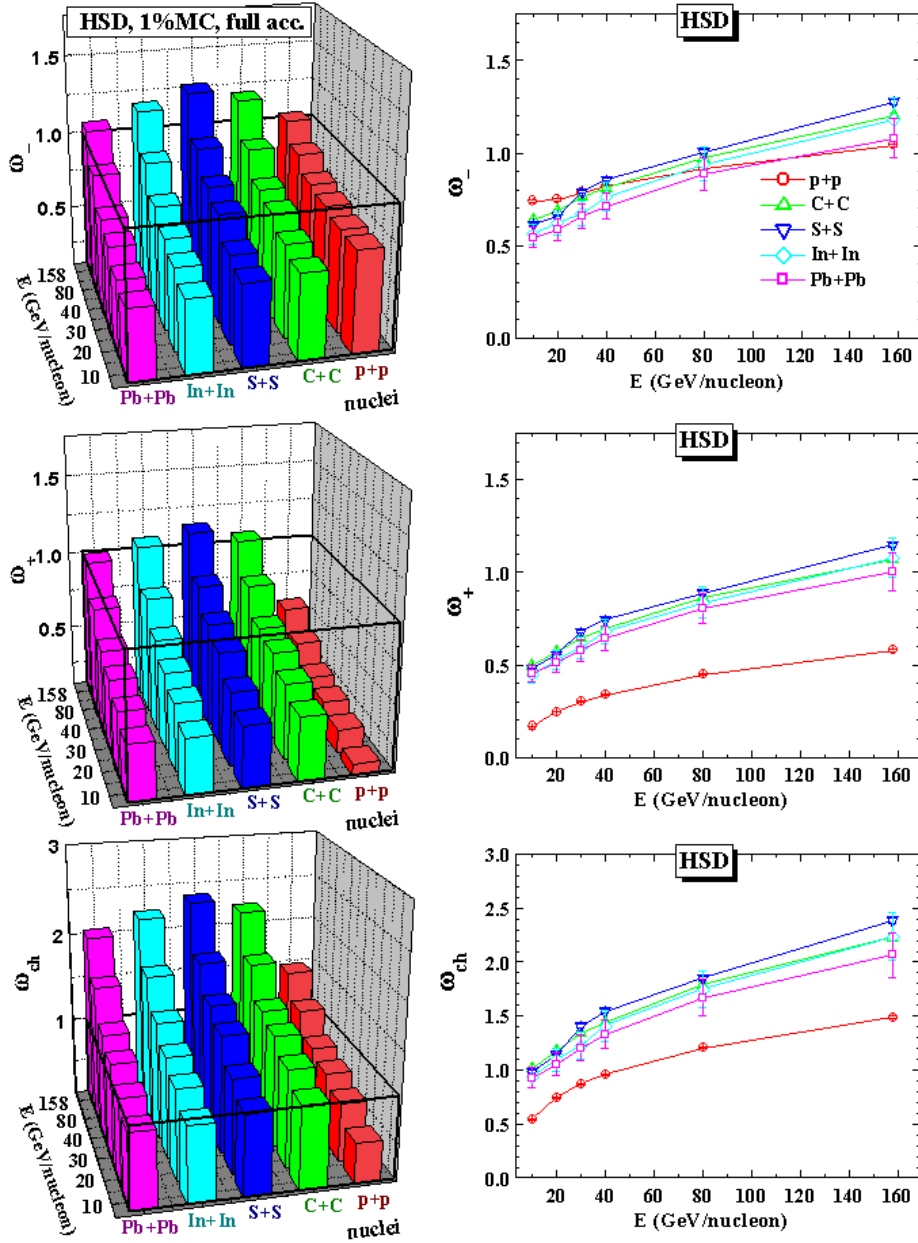


Figure 22. The HSD results for ω_- (upper panel), ω_+ (middle panel), and ω_{ch} (lower panel) in $A + A$ and $p+p$ collisions for the full 4π acceptance in 3D (*left*) and 2D (*right*) projection. The 1% most central C+C, S+S, In+In, and Pb+Pb collisions are selected by choosing the largest values of N_P^{proj} at different collision energies $E_{lab}=10, 20, 30, 40, 80, 158$ AGeV. The errorbars indicate the estimated uncertainties in the model calculations. The HSD results from inelastic $p+p$ collisions are the same as in Fig. 18.

event-by-event fluctuations.

Note that the MIS and Eq. (20) work for the multiplicity fluctuations simulated by the transport models in full 4π acceptance but not for the acceptance in a specific

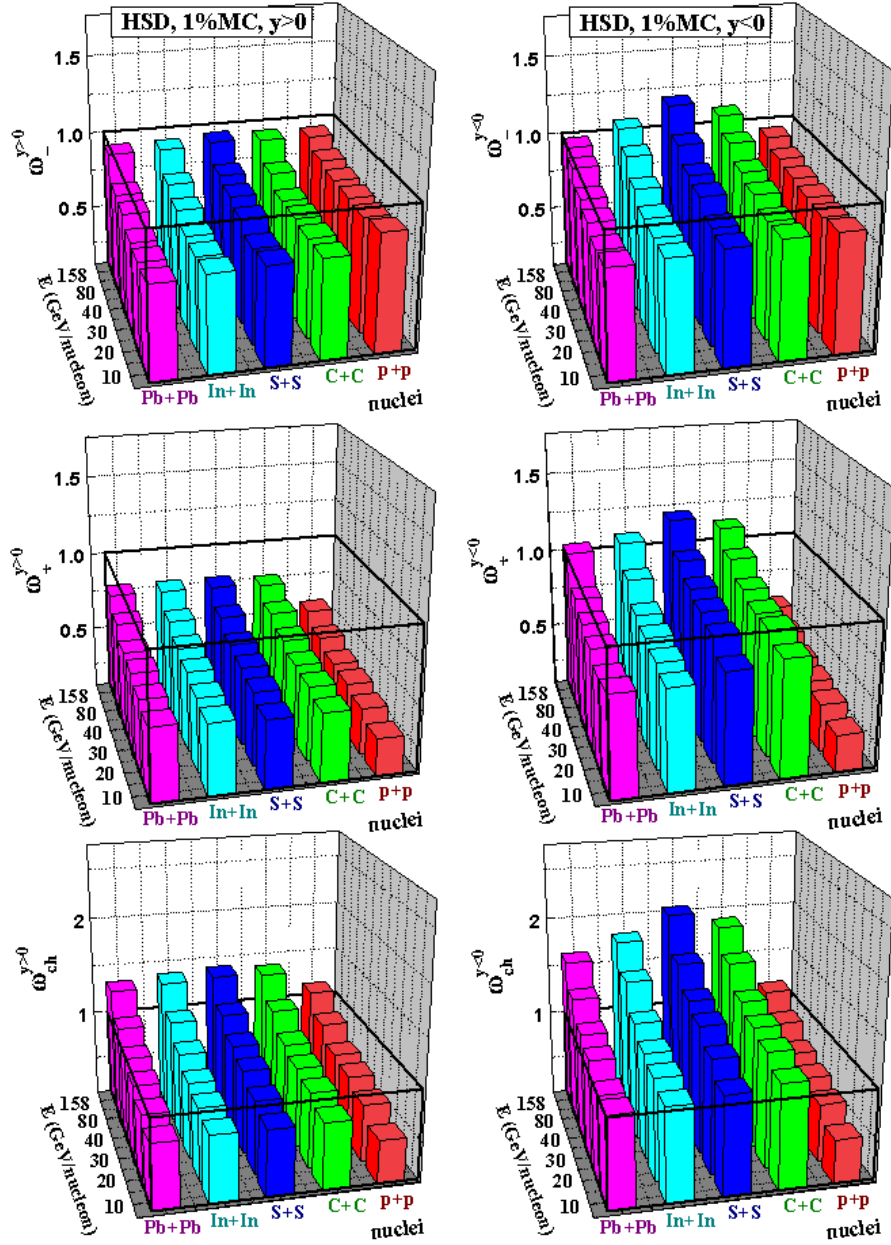


Figure 23. The same as in Fig. 22, but for final hadrons accepted in the projectile hemisphere, $y > 0$ (left), and in the target hemisphere, $y < 0$ (right).

rapidity region. The results for inelastic p+p collisions are identical in the projectile and target hemispheres. This is not the case in the sample of 1% most central $A+A$ collisions selected by N_P^{proj} . The total number of nucleons participating in $A+A$ collisions fluctuates. These fluctuations are not symmetric in forward-backward hemispheres: in the selected 1% sample the number of target participants N_P^{targ} fluctuates essentially stronger than that of N_P^{proj} . The HSD results in Fig. 23 clearly demonstrate larger values for all scaled variances, ω_- , ω_+ , and ω_{ch} , for $y < 0$ acceptance than those for

$y > 0$ one. This is due to stronger target participant fluctuations, $\omega_P^{targ} > \omega_P^{proj}$.

6. Fluctuations and Correlations in Au+Au Collisions at RHIC

In this Section we discussed some features of the particle number fluctuations [74] and forward-backward correlations [75] in Au+Au collisions at $\sqrt{s_{NN}} = 200$ GeV.

6.1. Multiplicity Fluctuations in Au+Au Collisions at RHIC

The charged multiplicity fluctuations in Au+Au collisions at $\sqrt{s_{NN}} = 200$ GeV have been measured recently by the PHENIX Collaboration [76,77]. The centrality selection is an important aspect of fluctuation studies in A+A collisions. As it was discussed in the previous sections the samples of collisions with a fixed number of projectile participants N_P^{proj} can be selected to minimize the participant number fluctuations at the fixed target experiments. This selection is possible due to a measurement of the number of nucleon spectators from the projectile, N_S^{proj} , in each individual collision by a calorimeter which covers the projectile fragmentation domain. In a collider type experiments another centrality trigger should be used. For the multiplicity fluctuations data the PHENIX Collaboration uses two kinds of detectors which define the centrality of Au+Au collision: Beam-Beam Counters (BBC) and Zero Degree Calorimeters (ZDC). The BBC measure the charged particle multiplicity in the pseudorapidity range $3.0 < |\eta| < 3.9$, and the ZDC – the number of neutrons with $|\eta| > 6.0$ [76,77]. These neutrons are part of the nucleon spectators. Due to technical reasons the neutron spectators can be only detected by the ZDC (not protons and nuclear fragments), but in both hemispheres. The BBC distribution will be used in the HSD calculations to divide Au+Au collision events into 5% centrality samples. The HSD does not specify different spectator groups – neutrons, protons, and nuclear fragments. Thus, one can not use the ZDC information. In Fig. 24 (*left*) the HSD results for the BBC distribution and centrality classes in Au+Au collisions at $\sqrt{s_{NN}} = 200$ GeV are shown. One finds a good agreement between the HSD shape of the BBC distribution and the PHENIX data [76,77]. Note, however, that the HSD $\langle N_P \rangle$ numbers are not exactly equal to the PHENIX values. It is also not obvious that different definitions for the 5% centrality classes give the same values of the scaled variance ω_P for the participant number fluctuations.

Defining the centrality selection via the HSD transport model (which is similar to the BBC in the PHENIX experiment) we calculate the mean number of nucleon participants, $\langle N_P \rangle$, and the scaled variance of its fluctuations, ω_P , in each 5% centrality sample. The results are shown in Fig. 24, right. The Fig. 25 (*left*) shows the HSD results for the mean number of charged hadrons per nucleon participant, $n_i = \langle N_i \rangle / \langle N_P \rangle$, where the index i stands for “–”, “+”, and “ch” final hadrons. Note that the centrality dependence of n_i is opposite to that of ω_P .

The PHENIX detector accepts charged particles in a small region of the phase space with pseudorapidity $|\eta| < 0.26$, azimuthal angle $\phi < 245^\circ$, and the p_T range from 0.2 to

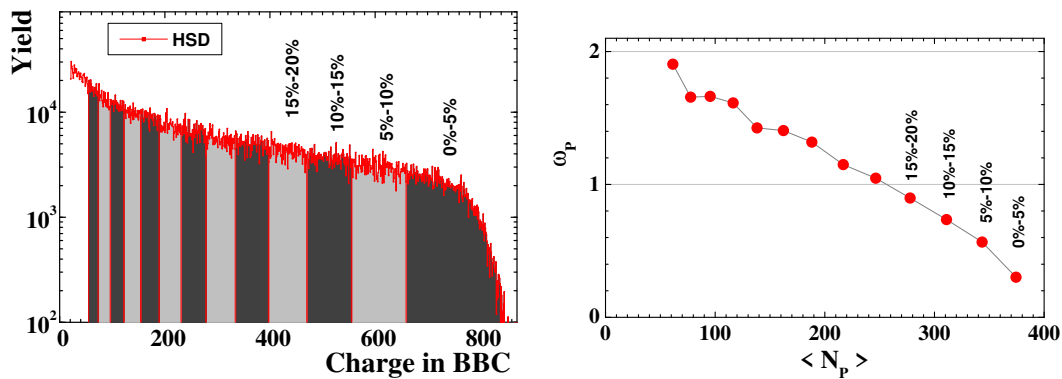


Figure 24. HSD model results for Au+Au collisions at $\sqrt{s_{NN}} = 200$ GeV. *Left:* Centrality classes defined via the BBC distribution. *Right:* The average number of participants, $\langle N_P \rangle$, and the scaled variance of the participant number fluctuations, ω_P , calculated for the 5% BBC centrality classes.

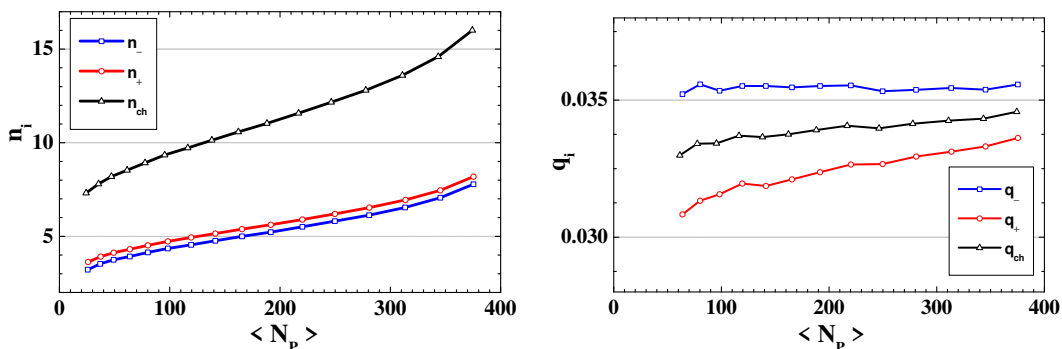


Figure 25. HSD results for different BBC centrality classes in Au+Au collisions at $\sqrt{s_{NN}} = 200$ GeV. *Left:* The mean number of charged hadrons per participant, $n_i = \langle N_i \rangle / \langle N_P \rangle$. *Right:* The fraction of accepted particles, $q_i = \langle N_i^{acc} \rangle / \langle N_i \rangle$.

2.0 GeV/c [76, 77]. The fraction of the accepted particles $q_i = \langle N_i^{acc} \rangle / \langle N_i \rangle$ calculated within the HSD model is shown in Fig. 25, right. According to the HSD results only about 3% of charged particles are accepted by the mid-rapidity PHENIX detector.

To estimate the role of the participant number event-by-event fluctuations the MIS relation (20) has been used. It has been assumed that N+N collisions define the fluctuations ω_i^* from a single source. To calculate the fluctuations ω_i^{acc} in the PHENIX acceptance the acceptance scaling formula (28) is used. One finds,

$$\omega_i^{acc} = 1 - q_i + q_i \omega_i^* + q_i n_i \omega_P. \quad (30)$$

The HSD results for ω_P (Fig. 24, right), n_i (Fig. 25, left), q_i (Fig. 25, right), together with the HSD nucleon-nucleon values, $\omega_-^* = 3.0$, $\omega_+^* = 2.7$, and $\omega_{ch}^* = 5.7$ at $\sqrt{s_{NN}} = 200$ GeV, define completely the results for ω_i^{acc} according to (30). We find a surprisingly good agreement of the results given by (30) with the PHENIX data shown in Fig. 26. The centrality dependence of ω_i^{acc} stems from the product, $q_i n_i \omega_P$, in the

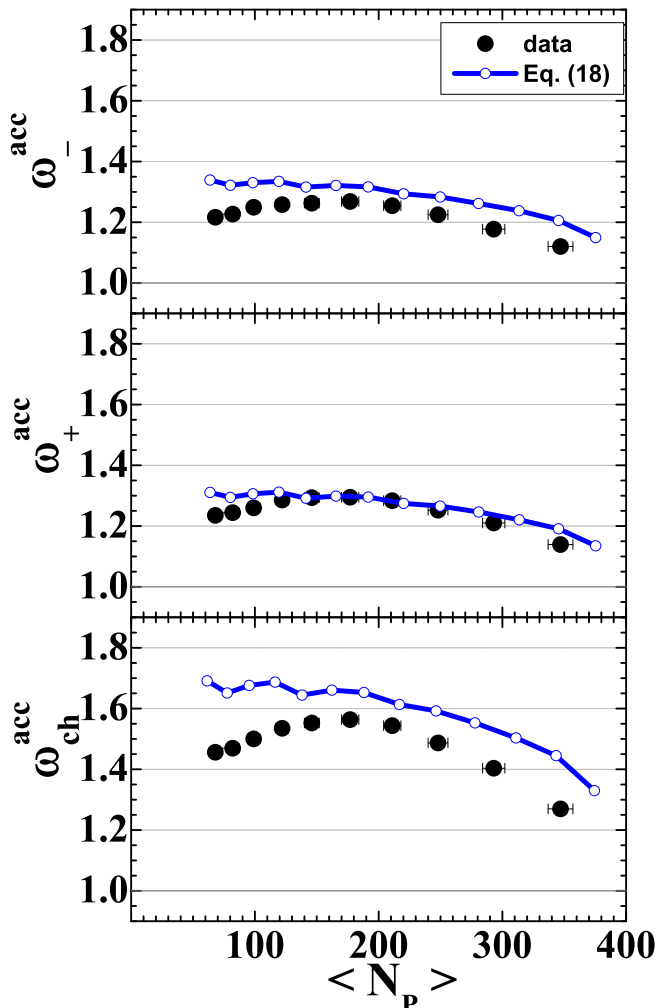


Figure 26. The scaled variance of charged particle fluctuations in Au+Au collisions at $\sqrt{s_{NN}} = 200$ GeV with the PHENIX acceptance. The circles are the PHENIX data [76, 77] while the open points (connected by the solid line) correspond to (30) with the HSD results for ω_P , n_i , and q_i .

last term of the r.h.s. of (30). Note that ω_P decreases with $\langle N_P \rangle$, whereas both n_i and q_i increase. It may lead to a nontrivial centrality dependence with a maximum at intermediate values of $\langle N_P \rangle$ as seen in the PHENIX data.

6.2. Forward-Backward Correlations

Correlations of particles between different regions of rapidity have for a long time been considered to be a signature of new physics. A shortening in the correlation length in rapidity has been thought to signal a transition to a quark-gluon plasma [78, 79]. Conversely, the appearance of long-range correlations has been associated with the onset of the percolation limit, also linked to the QCD phase transition [80, 81]. Recently, the correlations across a large distance in rapidity have also been suggested to arise from a color glass condensate [82, 83]. The observation of such correlations in A+A collisions

at RHIC energies by the STAR Collaboration [84, 85] has therefore elicited a lot of theoretical interest.

The purpose of this Section is to identify some *baseline* contributions to the experimentally observed correlations, contributions that do not depend on new physics [75]. Two models that incorporate event-by-event fluctuations in initial conditions have been used to illustrate the effect of these contributions: the HSD transport model and a ‘toy’ wounded nucleon model. Based on such a comparison one can argue that a study of the dependence of correlations on the centrality bin definition as well as the bin size may distinguish between ‘trivial’ correlations and correlations arising from ‘new physics’.

The statistical properties of a particular sample of events can be characterized by a set of moments or cumulants of some observable. These properties depend upon a set of criteria which are used to select this sample. Applied to the context of A+A collisions this translates to the construction of centrality bins of collision events from minimum-bias data. The charged hadron multiplicities N_A and N_B will be considered in two symmetric intervals $\Delta\eta$ of pseudo-rapidity. After construction of the centrality bins, one can calculate the moments of a resulting distribution $P_c^{\eta_{gap}}(N_A, N_B; \Delta\eta)$:

$$\langle N_A^k \cdot N_B^l \rangle_c^{\eta_{gap}} \equiv \sum_{N_A, N_B} N_A^k N_B^l P_c^{\eta_{gap}}(N_A, N_B; \Delta\eta) . \quad (31)$$

In (31) the subscript c denotes a particular centrality bin, while the superscript η_{gap} denotes the separation of two symmetric intervals $\Delta\eta$ in pseudo-rapidity space where particle multiplicities N_A and N_B are measured. The correlation coefficient is defined by

$$\rho \equiv \frac{\langle \Delta N_A \cdot \Delta N_B \rangle_c^{\eta_{gap}}}{\sqrt{\langle (\Delta N_A)^2 \rangle_c^{\eta_{gap}} \langle (\Delta N_B)^2 \rangle_c^{\eta_{gap}}}} \quad (32)$$

and measures how strongly multiplicities N_A and N_B – in a given centrality bin c for pseudo-rapidity separation η_{gap} – are correlated. In (32), $\Delta N \equiv N - \langle N \rangle_c^{\eta_{gap}}$ and $\langle (\Delta N_A)^2 \rangle_c^{\eta_{gap}} = \langle (\Delta N_B)^2 \rangle_c^{\eta_{gap}}$ for symmetric intervals.

The recent preliminary data on the forward-backward correlation coefficient (32) of charged particles by the STAR Collaboration [84,85] exhibit two striking features: a) an approximate independence on the width of the pseudo-rapidity gap η_{gap} , b) a strong increase of ρ with centrality.

6.3. *Glauber Monte Carlo Model*

The PHOBOS Glauber Monte Carlo code [86] coupled to a ‘toy’ wounded nucleon model is used here, referred to as GMC. The aim of this model is to emphasize two crucial aspects: 1) an averaging over different system sizes within one centrality bin introduces correlations; 2) the strength of these correlations depend on the criteria used for the centrality definition and on the size of the centrality bins.

Employing the Glauber code the distribution of the number of participating nucleons, N_P , is modelled in each A+A collision for given impact parameter b (cf.

Fig. 27, *left*). This is done for Au+Au with standard Wood-Saxon profile and the N+N cross section of $\sigma_{NN} = 42$ mb. The ‘event’ construction proceeds then in a two-step process. Firstly, the total number of charged particles is randomly generated:

$$N_{ch} = \sum_{i=1}^{N_P} n_{ch}^i, \quad (33)$$

where the number of charged particles n_{ch}^i per participating nucleon are generated by independently sampling a Poisson distribution with given mean value $\bar{n}_{ch} = 10$. Secondly, these charged particles are randomly distributed according to a Gaussian in pseudo-rapidity space:

$$\frac{dN_{ch}}{d\eta} \propto \exp\left(-\frac{\eta^2}{2\sigma_\eta}\right), \quad (34)$$

where $\sigma_\eta = 3$ defines the width of the pseudo-rapidity distribution. Hence, in each single event there are no correlations between the momenta of any two particles. Note that numerical values of \bar{n}_{ch} and σ_η are fixed in a way to have a rough correspondence with the data on charged particle production at $\sqrt{s_{NN}} = 200$ GeV.

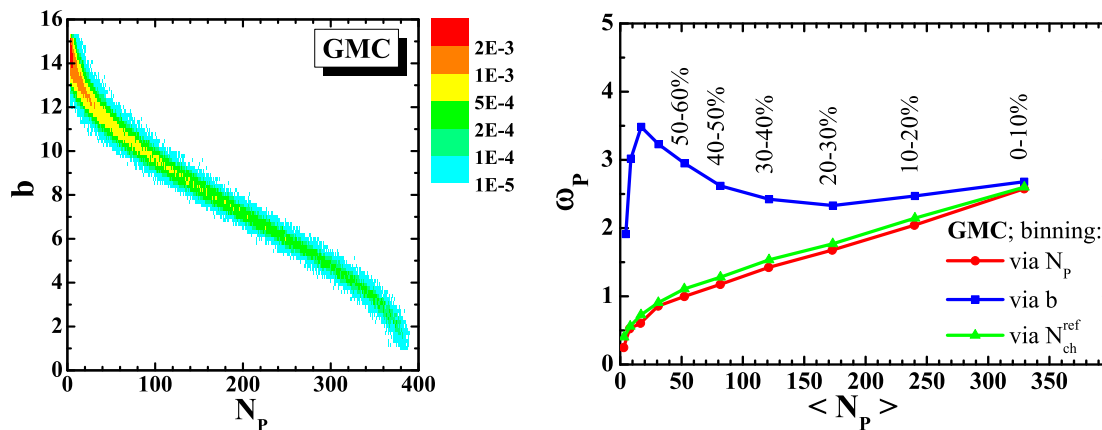


Figure 27. *Left:* The histogram shows the distribution of events with a fixed number of participating nucleons N_P and fixed impact parameter b in Au+Au collisions at $\sqrt{s_{NN}} = 200$ GeV. *Right:* The scaled variance ω_P of the distribution of participating nucleons in 10% bins as defined via b , N_P , and N_{ch}^{ref} .

Fig. 27 (*left*) shows the GMC event distribution in the (b, N_P) -plane. For each of these events we randomly generate the number of charged particles N_{ch} and their η -distribution according to (33) and (34), respectively. The construction of centrality classes can now be done in several ways. The following criteria are chosen: via impact parameter b , via the number of participating (wounded) nucleons N_P , and via the charged particle multiplicity N_{ch}^{ref} in the midrapidity window $|\eta| < 1$.

In the case of choosing the number of participating nucleons N_P for centrality definition, one takes vertical cuts in Fig. 27 (*left*), while choosing the impact parameter

b , one takes horizontal cuts. Hence, depending on the centrality definition, one may assign a particular event (characterized by N_P and b) to two different centrality bins.

Fig. 27 (*right*) shows the resulting scaled variance ω_P ,

$$\omega_P \equiv \frac{\langle (\Delta N_P)^2 \rangle_c}{\langle N_P \rangle_c}, \quad (35)$$

of the underlying distribution of the number of participating nucleons N_P in each centrality bin. Using the centrality selection via impact parameter b , which is only the theoretically available trigger, one generally obtains a rather wide distribution of participating nucleons in each bin. The lines for centrality selections via N_{ch}^{ref} and via N_P are similar due to the event construction by (33) and (34).

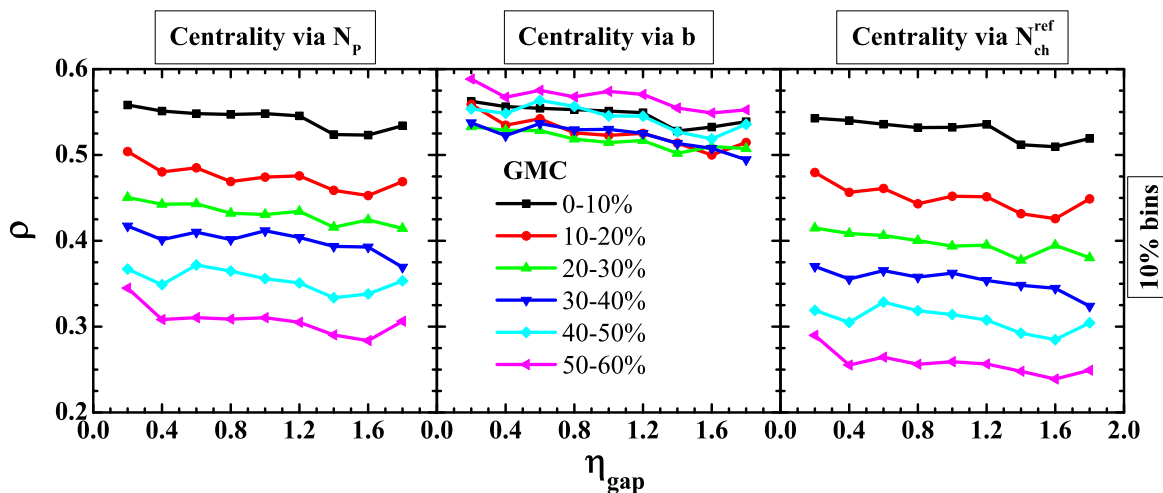


Figure 28. The forward-backward correlation coefficient ρ for 10% centrality classes defined via N_P (*left*), via the impact parameter b (*middle*), and via the multiplicity in the central rapidity region N_{ch}^{ref} (*right*).

The sensitivity of the forward-backward correlation signal as a function of the separation η_{gap} of two narrow intervals ($\Delta\eta = 0.2$) on the centrality definition is investigated now. This is done for the 10% centrality defined via N_P , via b , and via N_{ch}^{ref} . The results are shown in Fig. 28. In the GMC one can identify the number of participating nucleons N_P with the system size, and ω_P as the measure for system size fluctuations. Having a large system – as measured by N_P – implies a large number of charged particles N_{ch} . In GMC they are distributed independently in pseudo-rapidity space. Conversely, an event with small N_P contains only few charged particles. By grouping the collision events into 10% centrality bins one finds rather large N_P -fluctuations in one specific bin. The averaging over different states in the centrality bin introduces correlations between any two regions of pseudo-rapidity. Small systems will have few particles ‘on the left’ and few particles ‘on the right’ with respect to midrapidity. Large systems will have many particles ‘on the left’ and many particles ‘on the right’. But this just means a non-zero forward-backward correlation. From the

definition (32) one finds a positive correlation coefficient ρ due to averaging over system sizes.

Note that centrality selections via N_P and via N_{ch} give essentially the same results for ρ in the GMC (cf. *left* and *right* panels of Fig. 28). Using the impact parameter b for the centrality definition generates centrality bins with almost constant ρ as seen in Fig. 28 (*middle*). This is due to a rather flat dependence of ω_P on the centrality defined via b as shown in Fig. 27 (*right*). In the GMC model the apparent ordering of ρ values with respect to centrality bins originates from the width of the underlying distribution in the number of wounded nucleons in each bin, i.e. from the values of ω_P .

The measured and apparently strong forward-backward correlations can be accounted for by a ‘toy’ model such as the GMC, provided it produces particles over the whole rapidity range and includes strong enough event-by-event fluctuations of N_P . The next section will show that an introduction of dynamics and hadron re-interactions within HSD does not alter these conclusions significantly.

6.4. HSD Transport Model Simulations

A physically more reasonable scenario which, however, also does not include any ‘new physics’ (such as color glass condensate, quark-gluon plasma, etc.) can be obtained in the HSD transport approach. As before within the GMC, the HSD events are generated according to a uniform distribution, $N_{ev}(b) \sim b$. The resulting distribution of events in the (N_P, b) -plane is similar to the GMC result depicted in Fig. 27 (*left*). Note, that the peripheral part of the distribution determines also the centrality binning and the real bin widths. This is crucial for most central collisions where the number of events is small. Slight uncertainties in the peripheral “tail” of the distribution leads to large errors in the sizes of most central bins and hence to large changes in results for fluctuations and correlations.

In contrast to the STAR data, the charged particle reference multiplicity N_{ch}^{ref} in the same pseudo-rapidity range $|\eta| < 1$ for all values of η_{gap} is used in the HSD simulations. This procedure introduces a systematic bias, since the pseudo-rapidity regions for the measured multiplicity in a small $\Delta\eta$ window (signal) and for the reference multiplicity partially overlap. This bias, however, is small and does not affect any of the conclusions.

Fig. 29 shows the scaled variance of the underlying N_P distribution for 10% (*left*) and 2% (*right*) centrality bins defined via different centrality triggers within HSD. The results for 10% bins can be compared with the scaled variance ω_P in the GMC model in Fig. 27 (*right*). Fluctuations of the number of participants, as well as their average values, are similar in both HSD and GMC models when the centrality bins are defined via N_P . These quantities are completely defined by the N_P distribution, which is similar in both models. Binning via the impact parameter b in HSD, as well as in GMC, gives decreasing fluctuations in the participant number with increasing collision centrality. The results for 10% bins defined via the reference multiplicity are rather different in the GMC and HSD models. In GMC the charged multiplicity distribution is implemented

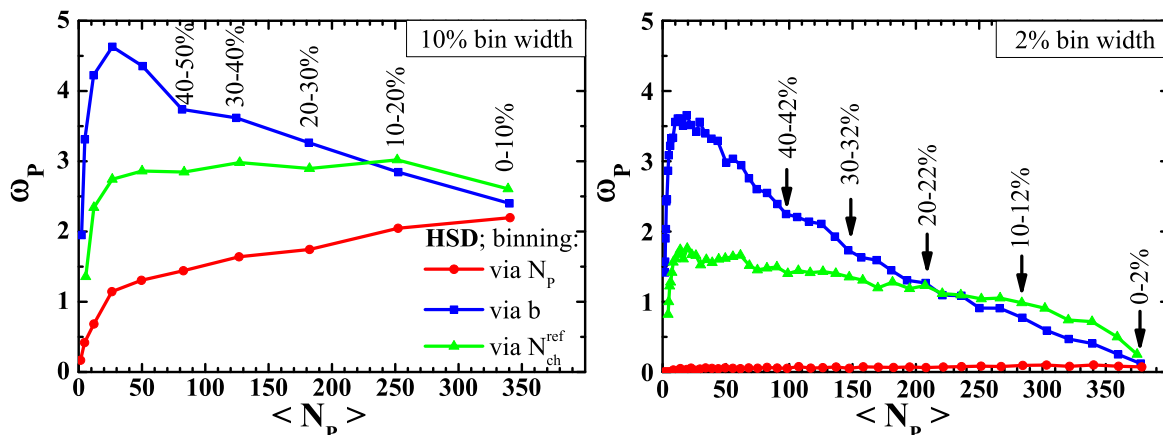


Figure 29. The HSD results for the fluctuations ω_{part} as a function of the mean value $\langle N_P \rangle$ of the participating nucleons within bins as defined via b , N_P , and N_{ch}^{ref} . The *left* panel corresponds to a 10% and the *right* to a 2% bin width.

according to (33) and (34). Hence, the results obtained by binning via the reference multiplicity follow the line obtained by binning via N_P . In contrast to the GMC, in the HSD simulations the average number of charged particles \bar{n}_{ch} per participating nucleon is not a constant, but increases with N_P . Additionally, the shape of rapidity distribution is also different in different centrality bins. These two effects lead to different values of ω_P in the centrality bins defined via N_{ch}^{ref} in the GMC and HSD models. An interesting feature seen in Figs. 27 and 30 is that ω_P is large for 10% most central bins. The behavior for 2% centrality bins is rather different: ω_P decreases with centrality as seen from Fig. 29 right. This becomes similar to the dependence of ω_P on N_P^{proj} considered in Sec. 3 for the fixed target experiments.

One comment is appropriate here. It was argued in Ref. [72] that any centrality selection in A+A collisions is equivalent to the geometrical one via impact parameter b . This was already discussed in Sec. 4. Different centrality selection criteria give indeed the same *average* values of physical observables. However, they may lead to rather different fluctuations of these observables in the corresponding centrality bins, cf. equal values of $\langle N_P \rangle$ and different values of ω_P for different centrality selections presented in Fig. 29. When considering smaller centrality bins (2% in Fig. 29, *right*) the fluctuations in the participant number become smaller but more strongly dependent on the definition of the binning.

Fig. 30 summarizes the dependence of forward-backward correlation coefficient ρ as a function of η_{gap} on the bin size and centrality definition within the HSD model. The dependence of ρ on η_{gap} is almost flat, reflecting a boost-invariant distribution of particles created by string breaking in the HSD. The *right top* panel of Fig. 30 demonstrates also a comparison of the HSD results with the STAR data [84,85]. One observes that the HSD results exceed systematically the STAR data. However, the main qualitative features of the STAR data – an approximate independence of the width of the pseudo-rapidity

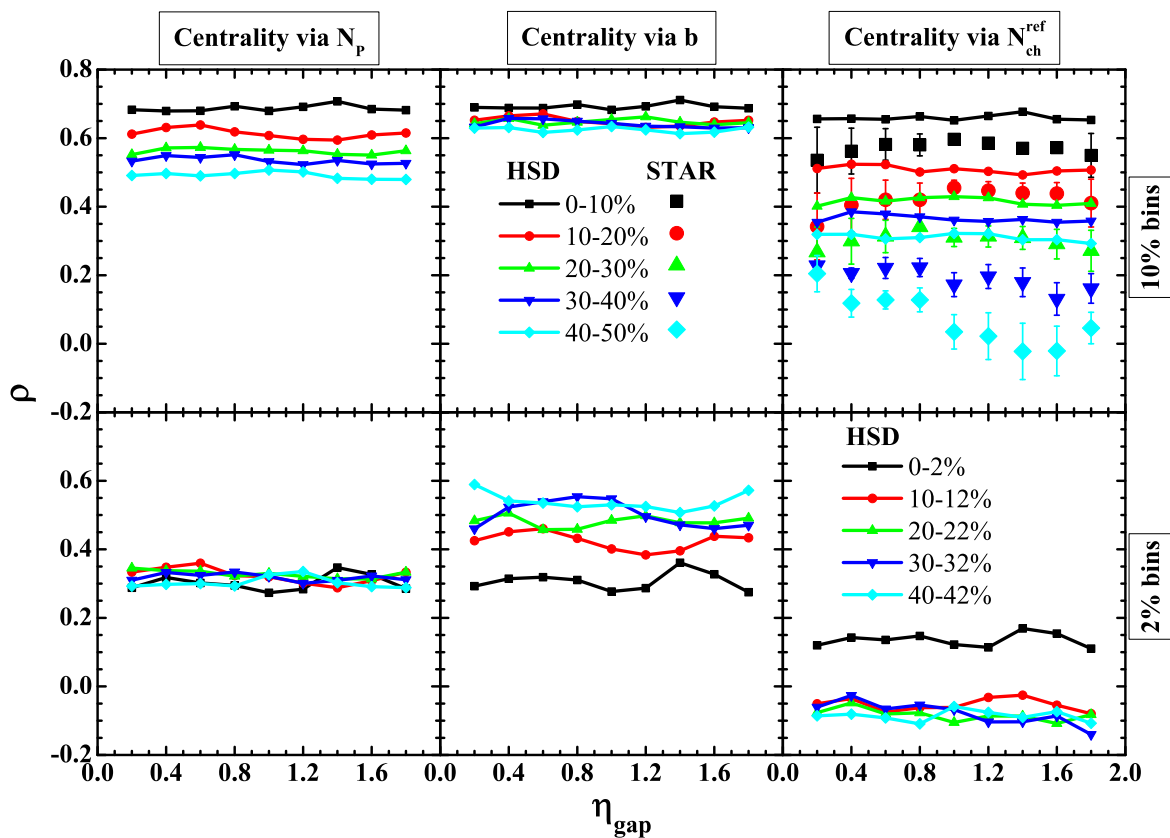


Figure 30. The HSD results for the forward-backward correlation coefficient ρ for 10% (top) and 2% (bottom) centrality classes defined via N_P (left), via impact parameter b (center), and via the reference multiplicity N_{ch}^{ref} (right). The symbols in the top right panel present the STAR data in Au+Au collisions at $\sqrt{s_{NN}} = 200$ GeV [84, 85].

gap η_{gap} and a strong increase of ρ with centrality – are fully reproduced by the HSD simulations.

The correlation coefficient ρ largely follows the trend of the participant number fluctuations ω_P as a function of centrality. The actual results, however, strongly depend on the way of defining the centrality bins. For instance, choosing smaller centrality bins leads to weaker forward-backward correlations, a less pronounced centrality dependence, and a stronger dependence on the bin definition. The physical origin for this is demonstrated in Fig. 31. As the bin size becomes comparable to the width of the correlation band between N_P and N_{ch}^{ref} , the systematic deviations of different centrality selections become dominant: the same centrality bins defined by N_P and by N_{ch}^{ref} contain different events and may give rather different values for the forward-backward correlation coefficient ρ .

It should be underlined that these properties are specific to the *geometric* nature of the correlations analyzed here. If the observed fluctuations are of *dynamical* origin (for example, arising from the quantum fluctuations of coherent fields created in the first fm/c of the system's lifetime as in Refs. [82, 83]), there are no evident reasons why

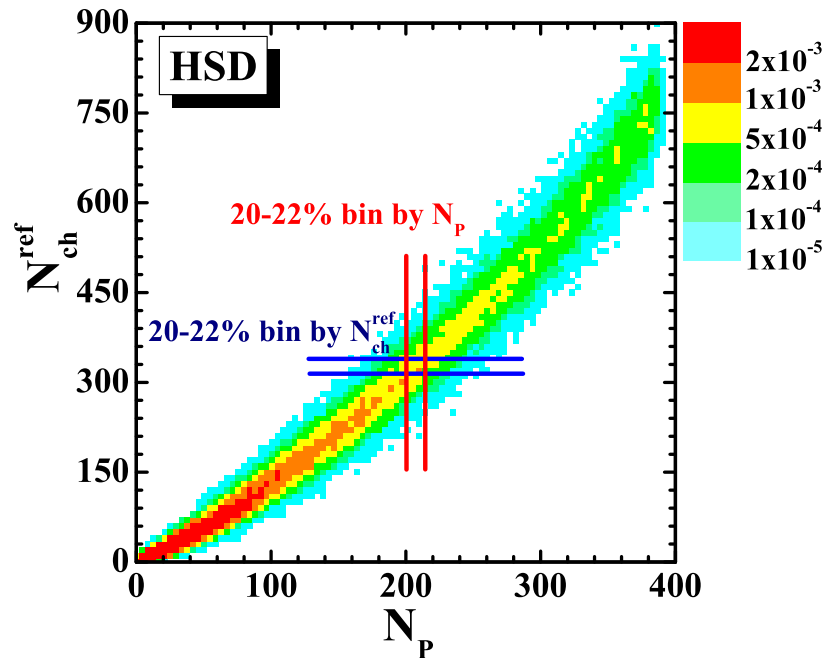


Figure 31. The histogram shows the distribution of HSD events with fixed number of participating nucleons N_P and fixed reference charge particle multiplicity N_{ch}^{ref} . The same centrality class (20-22% as an example) defined in various ways contains different events.

they should strongly depend on the centrality bin definitions and bin sizes. Thus, the experimental analysis for different bin sizes and centrality definitions – as performed here – may serve as a diagnostic tool for an origin of the observed correlations. A strong specific dependence of the correlations on bin size and centrality definition would signify their geometrical origin.

7. Fluctuations of Conserved Charges in Nucleus-Nucleus Collisions

The aim of the present Section is to study event-by-event fluctuations of the conserved charges – net baryon number and electric charge – in Pb-Pb collisions at 158 AGeV energies within the HSD transport approach [87].

7.1. Net Baryon Number Fluctuations

Let's start with a quantitative discussion by first considering the fluctuations of the net baryon number in different regions of the participant domain in collisions of two identical nuclei. These fluctuations are most closely related to the fluctuations of the number of participant nucleons because of baryon number conservation.

The HSD results for ω_B in Pb+Pb at 158 AGeV are presented in Fig. 32. In

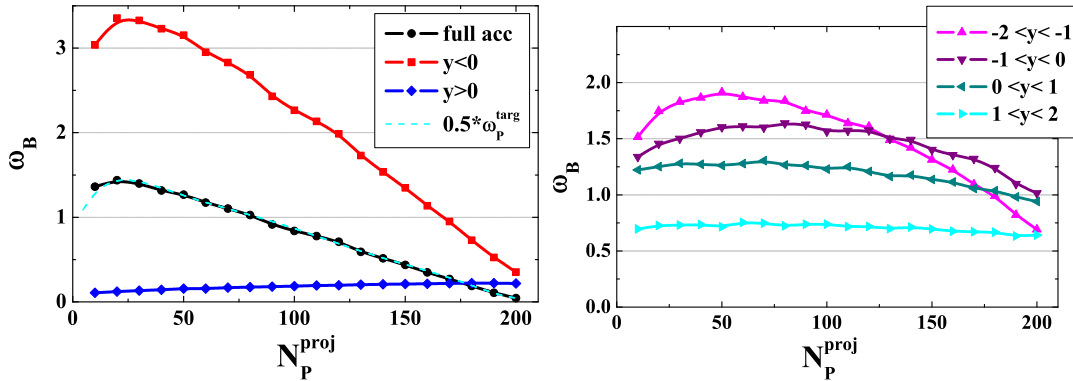


Figure 32. The HSD simulations for Pb+Pb collisions at 158 AGeV for fixed values of N_P^{proj} . *Left:* The baryon number fluctuations in full acceptance, ω_B , in projectile hemisphere, ω_B^p (lower curve), and in target hemisphere, ω_B^t (upper curve). *Right:* The scaled variances of the baryon number fluctuations in different rapidity intervals.

each event the nucleon spectators when counting the number of baryons are subtracted. Otherwise there would be no fluctuations of the net baryon number in the full acceptance and ω_B equals to zero. The net baryon number in the full phase space, $B \equiv N_B - N_{\bar{B}}$, equals to the total number of participants $N_P = N_P^{targ} + N_P^{proj}$. At fixed N_P^{proj} the N_P number fluctuates due to fluctuations of N_P^{targ} . These fluctuations correspond to an average value, $\langle N_P^{targ} \rangle \simeq N_P^{proj}$, and a scaled variance, ω_P^{targ} (see Fig. 4). Thus, for the net baryon number fluctuations in the full phase space one finds, $\omega_B \simeq 0.5\omega_B^{targ}$. A factor $1/2$ appears because only a half of the total number of participants fluctuates.

One introduces ω_B^p and ω_B^t , where the superscripts p and t mark quantities measured in the projectile and target momentum hemispheres, respectively. Fig. 32 demonstrates that $\omega_B^t > \omega_B^p$, both in the whole projectile-target hemispheres and in the symmetric rapidity intervals. On the other hand one observes that $\omega_B^p \approx \omega_B^t$ in most central collisions. This is because the fluctuations of the target participants become negligible in this case, i.e. $\omega_P^{targ} \simeq 0$ (Fig. 4, *right*). As a consequence the fluctuations of any observable in the symmetric rapidity intervals become identical in most central collisions. Note also that transparency-mixing effects are different at different rapidities. From Fig. 32 (*right*) it follows that ω_B^p in the target rapidity interval $[-2, -1]$ is much larger than ω_B^t in the symmetric projectile rapidity interval $[1, 2]$. This fact reveals the strong transparency effects. On the other hand, the behavior is different in symmetric rapidity intervals near the midrapidity. From Fig. 32 (*right*) one observes that ω_B^p in the target rapidity interval $[-1, 0]$ is already much closer to ω_B^t in the symmetric projectile rapidity interval $[0, 1]$. This gives a rough estimate of the width, $\Delta y \approx 1$, for the region in rapidity space where projectile and target nucleons communicate to each others.

7.2. Net Electric Charge Fluctuations

It is difficult to study experimentally the baryon number fluctuations since an identification of neutrons in a large acceptance in a single event is difficult. In this subsection we consider the HSD results for the net electric charge, Q , fluctuations. As $Q \cong 0.4B$ in the initial heavy nuclei one can naively expect that Q fluctuations are quite similar to B fluctuations. However, there is a principal difference between Q and B in relativistic A+A collisions. Fig. 33 demonstrates the rapidity distributions of the net baryon number, $B = N_B - N_{\bar{B}}$ (*left*), and *total* number of baryons, $N_B + N_{\bar{B}}$ (*right*), for different centralities in Pb+Pb collisions at 158 AGeV. One observes that both quantities are very close to each other; the y -dependence and absolute values are very close for B and $N_B + N_{\bar{B}}$ distributions. This is, of course, because the number of antibaryons is rather small, $N_{\bar{B}} \ll N_B$.

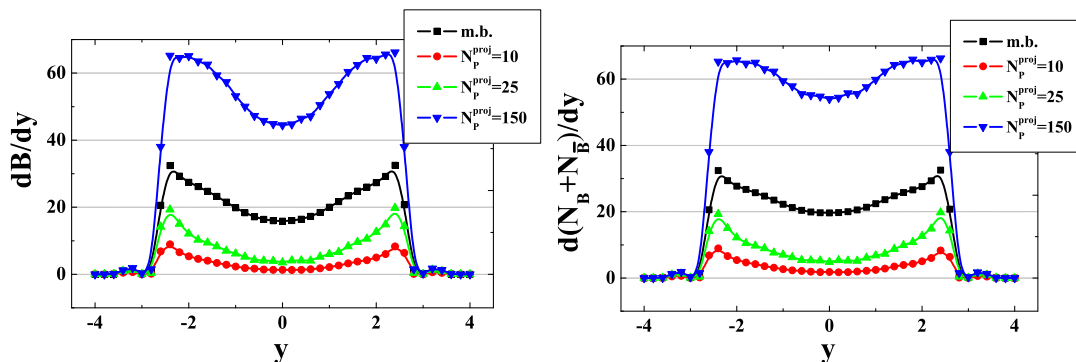


Figure 33. The HSD rapidity distributions in Pb+Pb collisions at 158 AGeV for the net baryon number, $B = N_B - N_{\bar{B}}$ (*left*), and total number of baryons, $N_B + N_{\bar{B}}$ (*right*), at different N_p^{proj} and in the minimum bias (m.b.) sample.

Fig. 34 shows the same as Fig. 33 but for the electric charge $Q = N_+ - N_-$ (*left*), and *total* number of charged particles, $N_{ch} \equiv N_+ + N_-$ (*right*). The y -dependence of

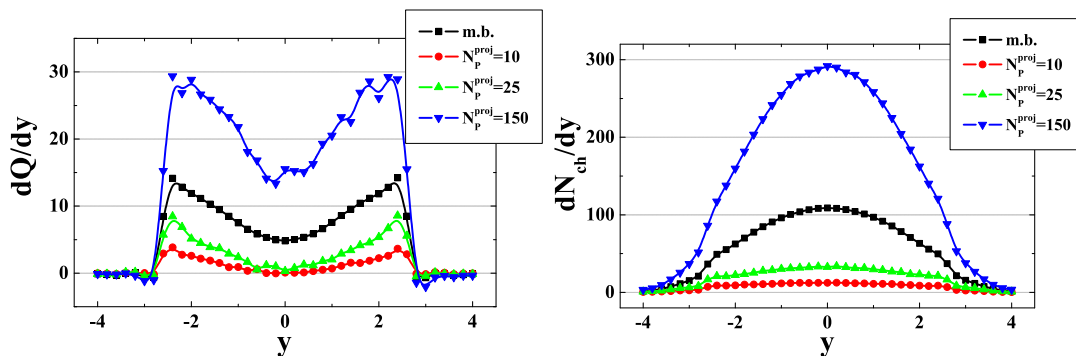


Figure 34. The same as in Fig. 33 but for the electric charge $Q = N_+ - N_-$ (*left*), and total number of charged particles, $N_{ch} \equiv N_+ + N_-$ (*right*).

dQ/dy and dN_{ch}/dy is quite different. Besides, the absolute values of N_{ch} are about

10 times larger than those of Q . This implies that $Q \ll N_+ \approx N_-$. In the previous subsection the scaled variance ω_B to quantify the measure of the net baryon fluctuations has been used. It appears to be a useful variable as ω_B is straightforwardly connected to ω_P^{targ} and due to the relatively small number of antibaryons. Fig. 34 tells that ω_Q is a bad measure of the electric charge fluctuations in high energy A+A collisions. One observes that $\omega_Q \equiv Var(Q)/\langle Q \rangle$ is much larger than 1 simply due to the small value of $\langle Q \rangle$ in a comparison with N_+ and N_- . If the A+A collision energy increases, it follows, $\langle N_+ \rangle \cong \langle N_- \rangle$ increases with collision energy, whereas $\langle Q \rangle \cong 0.4B$ remains constant. This leads to very large values of $\omega_Q \rightarrow$. The same would happen with ω_B , too, but at much larger collision energies. A useful measure of the net electric charge fluctuations is the quantity (see, e.g., [88]):

$$X_Q \equiv \frac{Var(Q)}{\langle N_{ch} \rangle}. \quad (36)$$

A value of X_Q can be easily calculated for the Boltzmann ideal gas in the grand canonical ensemble. In this case the number of negative and positive particles fluctuates according to the Poisson distribution (i.e. $\omega_- = \omega_+ = 1$), and the correlation between N_+ and N_- are absent (i.e. $\langle N_+ N_- \rangle = \langle N_+ \rangle \langle N_- \rangle$), so that $X_Q = 1$. On the other hand, the canonical ensemble formulation (i.e. when $Q = const$ fixed exactly for all microscopic states of the system) leads to $X_Q = 0$. Fig. 35 shows the results of the HSD simulations for the full acceptance, for the projectile and target hemispheres (*left*), and also for symmetric rapidity intervals in the c.m.s. (*right*).

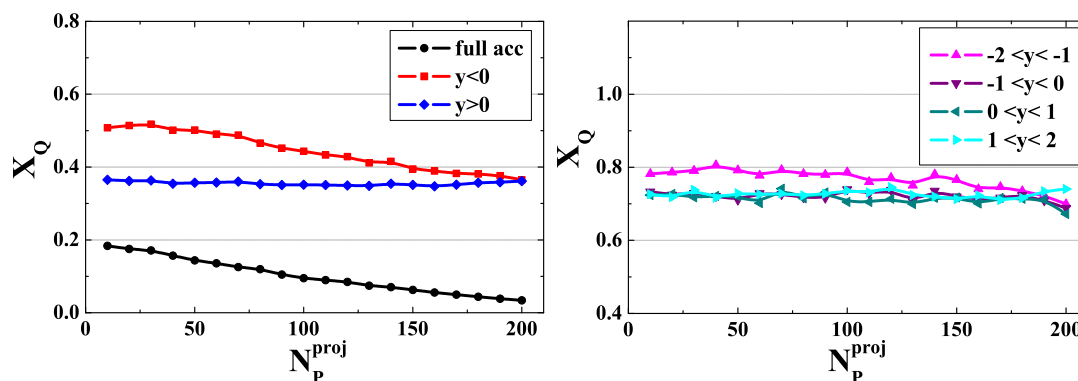


Figure 35. *Left:* The HSD simulations in Pb+Pb collisions at 158 AGeV for X_Q at different values of N_P^{proj} in the full acceptance (lower curve), for the projectile (middle curve) and target (upper curve) hemispheres. *Right:* The same, but for the fixed rapidity intervals in the c.m.s.

The Q fluctuation in the full acceptance is due to N_P^{targ} fluctuations. As $Q \cong 0.4B$ in colliding (heavy) nuclei, one may expect $Var(Q) \cong 0.16 Var(B)$. In addition, $\langle N_{ch} \rangle \cong 4\langle N_P \rangle$ at 158 AGeV, so that one estimates $X_Q \cong 0.04 \omega_B$ for the fluctuations in the full phase space. The actual values of X_Q presented in Fig. 35 (*left*) are about 3 times larger. This is because of Q fluctuations due to different event-by-event values of proton and neutron participants even in a sample with fixed values of N_P^{proj} and N_P^{targ} .

From Fig. 35 (*right*) one sees only a tiny difference between the X_Q values in the symmetric rapidity intervals in the projectile and target hemispheres, and slightly stronger effects for the whole projectile and target hemispheres (Fig. 35, *left*). In fact, the fluctuations of N_+ and N_- are very different in the projectile and target hemispheres, and the scaled variances ω_+^t and ω_-^t have a very strong N_P^{proj} -dependence. This is shown on top-*left* and middle-*left* panels of Fig. 8.

The X_Q can be presented in two equivalent forms

$$\begin{aligned} X_Q &= \omega_+ \frac{\langle N_+ \rangle}{\langle N_{ch} \rangle} + \omega_- \frac{\langle N_- \rangle}{\langle N_{ch} \rangle} - 2 \frac{\Delta(N_+, N_-)}{\langle N_{ch} \rangle} \\ &= 2 \omega_+ \frac{\langle N_+ \rangle}{\langle N_{ch} \rangle} + 2 \omega_- \frac{\langle N_- \rangle}{\langle N_{ch} \rangle} - \omega_{ch} . \end{aligned} \quad (37)$$

The Eq. (37) is valid for any region of the phase space: full phase space, projectile or target hemisphere, etc. As seen from Fig. 8, both ω_+^t and ω_-^t are large and strongly N_P^{proj} -dependent. This is not seen in X_Q^t because of strong correlations between N_+^t and N_-^t , i.e. the term $2 \Delta(N_+, N_-)/\langle N_{ch} \rangle$ compensates ω_+ and ω_- terms in (37).

Fig. 36 shows a comparison of the HSD results for X_Q with NA49 data in Pb+Pb collisions at 158 AGeV for the forward rapidity interval $1.1 < y < 2.6$ inside the projectile hemisphere with additional p_T -filter imposed.

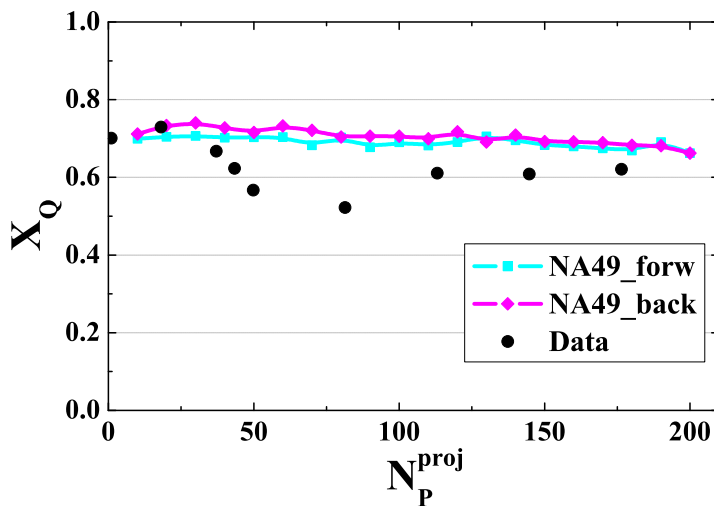


Figure 36. The HSD results for X_Q for Pb+Pb collisions at 158 AGeV for the forward rapidity interval $1.1 < y < 2.6$ inside the projectile hemisphere. The solid dots are the estimates obtained from Eq. (37) using the NA49 experimental data [46, 89, 90] (the error bars are not indicated here). For illustration, the HSD results in the symmetric backward rapidity interval $-2.6 < y < -1.1$ (target hemisphere) are also presented.

As an illustration, the HSD results in the symmetric backward rapidity interval $-2.6 < y < -1.1$ (target hemisphere) are also included. One observes no difference between the X_Q results for the NA49 acceptance in the projectile and target hemispheres. The HSD values for ω_+ , ω_- , and ω_{ch} are rather different in the projectile and target hemispheres for the NA49 acceptance (see Fig. 8). This is not seen in Fig. 36 for X_Q .

As explained above a cancellation between ω_+ , ω_- and ω_{ch} terms take place in (37). In fact, NA49 did not perform the X_Q measurements. The X_Q -data (solid dots) presented in Fig. 36 are obtained from Eq. (37) using the NA49 data for ω_+ , ω_- , and ω_{ch} as well as $\langle N_+ \rangle$, $\langle N_- \rangle$, and $\langle N_{ch} \rangle$ [46, 89, 90]. Such a procedure leads, however, to very large errors for X_Q (not indicated in Fig. 36) which excludes any conclusion about the (dis)agreement of HSD results with NA49 data.

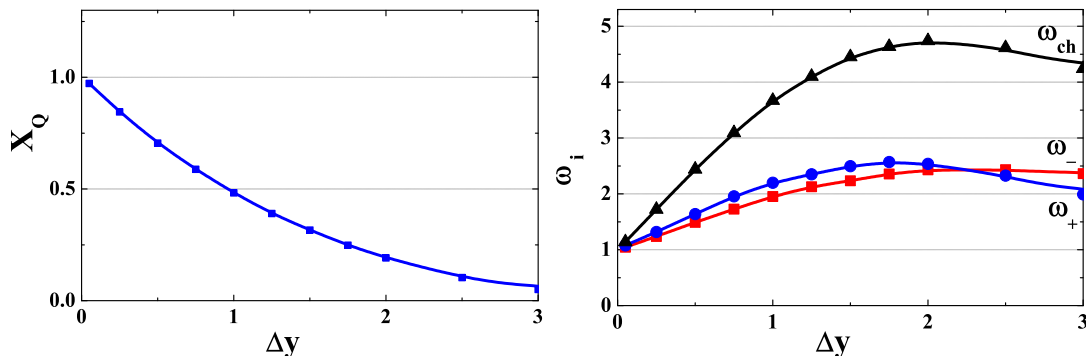


Figure 37. The HSD results for electric charge fluctuations in 2% most central Pb+Pb collisions at 158 AGeV in the symmetric rapidity interval, $\Delta Y = [-y, y]$ as a function of $\Delta y = \Delta Y/2$ in the c.m.s. A *left* panel shows the behavior of X_Q , and a *right* one demonstrates separately ω_+ , ω_- , and ω_{ch} .

It is instructive to consider the electric charge fluctuations in the symmetric rapidity interval $[-y, y]$ in the c.m.s. for the most central Pb+Pb events. The sample of most central events is chosen by restricting the impact parameter to $b < 2$ fm. It gives about 2% most central Pb+Pb collisions from the whole minimum bias sample. Fig. 37 shows the HSD results for electric charge fluctuations in 2% most central Pb+Pb collisions for the symmetric rapidity interval $\Delta Y = [-y, y]$ in the c.m.s. as the function of $\Delta y = \Delta Y/2$.

For $\Delta Y \rightarrow 0$ one finds $X_Q \rightarrow 1$. This can be understood as follows: For $\Delta Y \rightarrow 0$ the fluctuations of negatively, positively and all charged particles behave as for the Poisson distribution: $\omega_+ \cong \omega_- \cong \omega_{ch} \cong 1$. Then from Eq. (37) it follows that $X_Q \cong 1$, too. From Fig. 37 (*right*) one observes that ω_+ , ω_- , and ω_{ch} all increase with increasing interval ΔY . However, X_Q decreases with ΔY and – because of global Q conservation – it goes approximately to zero when all final particles are accepted.

8. Fluctuations of Ratios in Nucleus-Nucleus Collisions

The measurement of the fluctuations in the kaon to pion ratio by the NA49 Collaboration [91] was the first event-by-event measurement in nucleus-nucleus collisions. It was suggested that this ratio might allow to distinguish events with enhanced strangeness production attributed to the QGP phase. Nowadays, the excitation function for this observable is available in a wide range of energies: from the NA49 collaboration [92]

in Pb+Pb collisions at the CERN SPS and from the STAR collaboration [93, 94] in Au+Au collisions at RHIC. First statistical model estimates of the K/π fluctuations have been reported in Refs. [95, 96]. The results from the transport model UrQMD have been presented in Ref. [97] for the SPS energy range.

This Section presents the results of a systematic study of K/π , K/p and p/π ratio fluctuations ($K = K^+ + K^-$, $\pi = \pi^+ + \pi^-$, and p means $p + \bar{p}$) based on the HSD transport model. These results will be compared to statistical model results in different ensembles [98, 99] and available experimental data.

8.1. Notations and Approximations

The fluctuations of the ratio $R_{AB} \equiv N_A/N_B$ will be characterized by [95, 96]

$$\sigma^2 \equiv \frac{\langle (\Delta R_{AB})^2 \rangle}{\langle R_{AB} \rangle^2}. \quad (38)$$

Using the expansion,

$$\frac{N_A}{N_B} = \frac{\langle N_A \rangle + \Delta N_A}{\langle N_B \rangle + \Delta N_B} = \frac{\langle N_A \rangle + \Delta N_A}{\langle N_B \rangle} \times \left[1 - \frac{\Delta N_B}{\langle N_B \rangle} + \left(\frac{\Delta N_B}{\langle N_B \rangle} \right)^2 - \dots \right], \quad (39)$$

one finds to second order in $\Delta N_A/\langle N_A \rangle$ and $\Delta N_B/\langle N_B \rangle$ the average value and fluctuations of the A to B ratio:

$$\langle R_{AB} \rangle \cong \frac{\langle N_A \rangle}{\langle N_B \rangle} \left[1 + \frac{\omega_B}{\langle N_B \rangle} - \frac{\Delta(N_A, N_B)}{\langle N_A \rangle \langle N_B \rangle} \right], \quad (40)$$

$$\begin{aligned} \sigma^2 &\cong \frac{\Delta(N_A, N_A)}{\langle N_A \rangle^2} + \frac{\Delta(N_B, N_B)}{\langle N_B \rangle^2} - 2 \frac{\Delta(N_A, N_B)}{\langle N_A \rangle \langle N_B \rangle} \\ &= \frac{\omega_A}{\langle N_A \rangle} + \frac{\omega_B}{\langle N_B \rangle} - 2\rho_{AB} \left[\frac{\omega_A \omega_B}{\langle N_A \rangle \langle N_B \rangle} \right]^{1/2}. \end{aligned} \quad (41)$$

If species A and B fluctuate independently according to the Poisson distributions (this takes place, for example, in the GCE for an ideal Boltzmann gas) one finds, $\omega_A = \omega_B = 1$ and $\rho_{AB} = 0$. The Eq. (41) then reads

$$\sigma^2 = \frac{1}{\langle N_A \rangle} + \frac{1}{\langle N_B \rangle}. \quad (42)$$

In a thermal gas, the average multiplicities are proportional to the system volume V . The Eq. (42) demonstrates then a simple dependence $\sigma^2 \propto 1/V$ on the system volume.

A few examples concerning to Eq. (41) are appropriate here. When $\langle N_B \rangle \gg \langle N_A \rangle$, e.g., $A = K^+ + K^-$ and $B = \pi^+ + \pi^-$, the σ^2 (41) is dominated by the less abundant particles and the resonances decaying into it. When $\langle N_A \rangle \cong \langle N_B \rangle$, e.g., $A = \pi^+$ and $B = \pi^-$, the correlation term in Eq. (41) may become especially important. A resonance decaying always into a $\pi^+\pi^-$ -pair does not contribute to σ^2 (41), but contributes to π^+ and π^- average multiplicities. This leads [96] to a suppression of σ^2 (41) in comparison

to its value given by Eq. (42). For example, if all π^+ and π^- particles come by pairs from decay of resonances, one finds the correlation coefficient $\rho_{\pi^+\pi^-} = 1$ in Eq. (41), and thus $\sigma^2 = 0$. In this case, the numbers of π^+ and π^- fluctuate as the number of resonances, but the ratio π^+/π^- does not fluctuate.

8.2. Mixed Events Procedure

The experimental data for N_A/N_B fluctuations are usually presented in terms of the so called dynamical fluctuations [100]§

$$\sigma_{dyn} \equiv \text{sign}(\sigma^2 - \sigma_{mix}^2) \left| \sigma^2 - \sigma_{mix}^2 \right|^{1/2}, \quad (43)$$

where σ^2 is defined by Eq. (41), and σ_{mix}^2 corresponds to the following *mixed events* procedure||. One takes a large number of nucleus-nucleus collision events, and measures the numbers of N_A and N_B in each event. Then all A and B particles from all events are combined into one *set*. A construction of *mixed events* is done like the following: One fixes a random number $N = N_A + N_B$ according to the experimental probability distribution $P(N)$, takes randomly N particles (A and/or B) from the *whole set*, fixes the values of N_A and N_B , and returns these N particles into the *set*. This is the mixed event number one. Then one constructs event number 2, number 3, etc.

Note that the number of events is much larger than the number of hadrons, N , in any single event. Therefore, the probabilities p_A and $p_B = 1 - p_A$ to take the A and B species from the whole *set* can be considered as constant values during the event construction. Another consequence of a large number of events is the fact that all A and B particles in any constructed *mixed event* most probably belong to different *physical events* of nucleus-nucleus collisions. Therefore, the correlations between N_B and N_A numbers in a physical event are expected to be destroyed in a mixed event. This is the main purpose of the mixed events construction. For any function f of N_A and N_B the mixed events averaging is then defined as,

$$\begin{aligned} \langle f(N_A, N_B) \rangle_{mix} &= \sum_N P(N) \sum_{N_A, N_B} f(N_A, N_B) \times \\ &\delta(N - N_A - N_B) \frac{(N_A + N_B)!}{N_A! N_B!} p_A^{N_A} p_B^{N_B}. \end{aligned} \quad (44)$$

The straightforward calculation of mixed averages (44) can be simplified by introducing the generating function $Z(x, y)$,

$$Z(x, y) \equiv \sum_N P(N) \sum_{N_A, N_B} \delta(N - N_A - N_B) \frac{(N_A + N_B)!}{N_A! N_B!} (xp_A)^{N_A} (yp_B)^{N_B}$$

§ Other dynamical measures, Φ [101,102] and F [96], can be also used. See the discussion of this point in the recent paper [103].

|| The idealized mixed events procedure appropriate for model analysis is described here. The real experimental mixed events procedure is more complicated and includes experimental uncertainties, such as particle identification etc.

$$= \sum_N P(N) (xp_A + yp_B)^N . \quad (45)$$

The averages (44) are then expressed as x - and y -derivatives of $Z(x, y)$ at $x = y = 1$. One finds:

$$\begin{aligned} \langle N_A \rangle_{mix} &= \left(\frac{\partial Z}{\partial x} \right)_{x=y=1} = p_A \langle N \rangle , \\ \langle N_B \rangle_{mix} &= \left(\frac{\partial Z}{\partial y} \right)_{x=y=1} = p_B \langle N \rangle , \end{aligned} \quad (46)$$

$$\langle N_A(N_A - 1) \rangle_{mix} = \left(\frac{\partial^2 Z}{\partial^2 x} \right)_{x=y=1} = p_A^2 \langle N(N - 1) \rangle , \quad (47)$$

$$\langle N_B(N_B - 1) \rangle_{mix} = \left(\frac{\partial^2 Z}{\partial^2 y} \right)_{x=y=1} = p_B^2 \langle N(N - 1) \rangle , \quad (48)$$

$$\begin{aligned} \langle N_A N_B \rangle_{mix} - \langle N_A \rangle_{mix} \langle N_B \rangle_{mix} &= \left(\frac{\partial^2 Z}{\partial x \partial y} \right)_{x=y=1} \\ &= p_A p_B \omega_N \langle N \rangle . \end{aligned} \quad (49)$$

Calculating the N_A/N_B fluctuations for mixed events according to (41) one gets:

$$\begin{aligned} \sigma_{mix}^2 &\equiv \frac{\Delta_{mix}(N_A, N_A)}{\langle N_A \rangle^2} + \frac{\Delta_{mix}(N_B, N_B)}{\langle N_B \rangle^2} - 2 \frac{\Delta_{mix}(N_A, N_B)}{\langle N_A \rangle \langle N_B \rangle} \\ &= \left[\frac{1}{\langle N_A \rangle} + \frac{\omega_N - 1}{\langle N \rangle} \right] + \left[\frac{1}{\langle N_B \rangle} + \frac{\omega_N - 1}{\langle N \rangle} \right] - 2 \frac{\omega_N - 1}{\langle N \rangle} \\ &= \frac{1}{\langle N_A \rangle} + \frac{1}{\langle N_B \rangle} . \end{aligned} \quad (50)$$

A comparison of the final result in Eq. (50) with Eq. (42) shows that the mixed event procedure gives the same σ^2 for N_A/N_B fluctuations as in the GCE formulation for an ideal Boltzmann gas, i.e. $\omega_A = \omega_B = 1$ and $\rho_{AB} = 0$. If $\omega_N = 1$ (e.g., for the Poisson distribution $P(N)$), one indeed finds $\omega_A^{mix} = \omega_B^{mix} = 1$ and $\rho_{AB}^{mix} = 0$. Otherwise, if $\omega_N \neq 1$, the mixed events procedure leads to $\omega_A^{mix} \neq 1$, $\omega_B^{mix} \neq 1$, and to non-zero $N_A N_B$ correlations, as seen from the second line of (50). However, the final result for σ_{mix}^2 (50) is still the same simple. It does not depend on the specific form of $P(N)$. Non-trivial ($\omega_{A,B}^{mix} \neq 1$) fluctuations of N_A and N_B as well as non-zero ρ_{AB}^{mix} correlations may exist in the mixed events procedure, but they are cancelled out exactly in σ_{mix}^2 .

8.3. Hadron Scaled Variances and Correlation Coefficients

The values of ω_π , ω_K , ω_p and $\rho_{K\pi}$, $\rho_{K\pi}$, $\rho_{K\pi}$ for the HSD simulations of and statistical model (SM) in Pb+Pb (Au+Au) central collisions are presented in Figs. 38 and 39.

Let us first comment the SM (see more details in Refs. [98,99]). In the SM the scaled variances ω_A and correlation parameter ρ_{AB} approach finite values in the thermodynamic limit of large volumes. For central Pb+Pb and Au+Au collisions the corresponding volumes in the SM are large enough. Finite volume corrections are expected on the level of a few percent. We discuss K/π fluctuations in more details. The π - K correlations $\rho_{K\pi}$

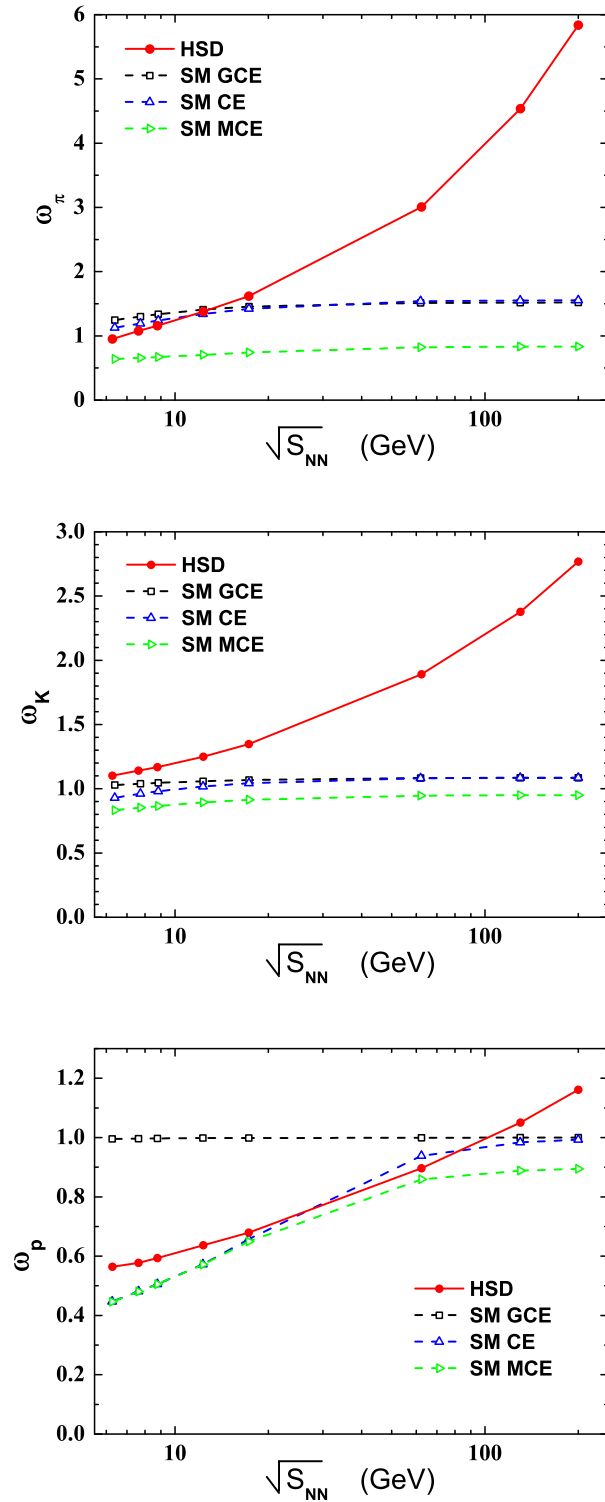


Figure 38. The SM results in the GCE, CE, and MCE ensembles and the HSD results (impact parameter $b = 0$) are presented for the scaled variances ω_π , ω_K , ω_p for Pb+Pb (Au+Au) collisions at different c.m. energies $\sqrt{s_{NN}}$.

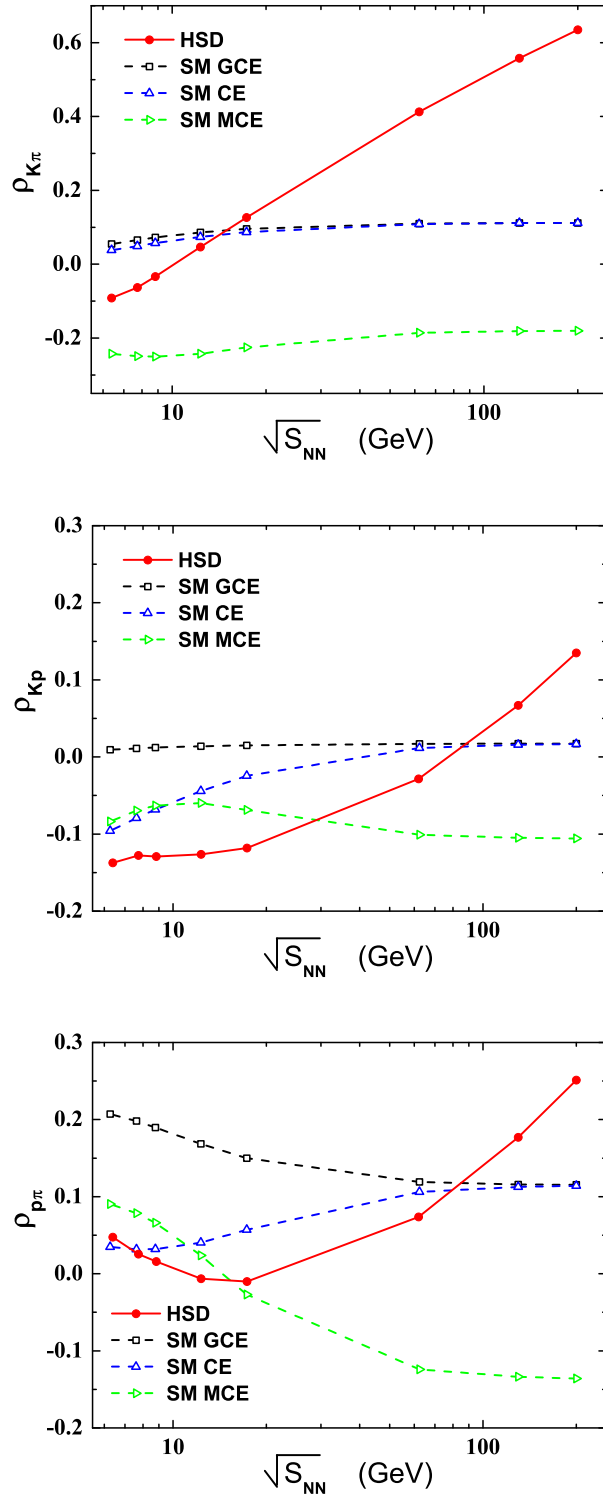


Figure 39. The SM results in the GCE, CE, and MCE ensembles and the HSD results (impact parameter $b = 0$) are presented for the correlation parameters $\rho_{K\pi}$, ρ_{Kp} , $\rho_{p\pi}$ for Pb+Pb (Au+Au) collisions at different c.m. energies $\sqrt{s_{NN}}$

are due to resonances having simultaneously K and π mesons in their decay products. In the hadron-resonance gas within the GCE ensemble, these quantum statistics and resonance decay effects are responsible for deviations of ω_K and ω_π from 1, and of $\rho_{K\pi}$ from 0. The most important effect of an exact charge conservation in the CE ensemble is a suppression of the kaon number fluctuation. This happens mainly due to exact strangeness conservation and is reflected in smaller CE values of ω_K at low collision energies in comparison to those from the GCE ensemble. The MCE values of ω_K and ω_π are further suppressed in comparison those from the CE ensemble. This is due to exact energy conservation. The effect is stronger for pions than for kaons since pions carry a larger part of the total energy. An important feature of the MCE is the anticorrelation between N_π and N_K , i.e. negative values of $\rho_{K\pi}$. This is also a consequence of energy conservation for each microscopic state of the system in the MCE [63]. The presented results demonstrate that global conservation laws are rather important for the values of ω_π , ω_K , and $\rho_{K\pi}$. In particular, the exact energy conservation strongly suppresses the fluctuations in the pion and kaon numbers and leads to $\omega_K < 1$ and $\omega_\pi < 1$ in the MCE ensemble, instead of $\omega_K > 1$ and $\omega_\pi > 1$ in the GCE and CE ensembles. The exact energy conservation changes also the π - K correlation into an anticorrelation: instead of $\rho_{K\pi} > 0$ in the GCE and CE ensembles one finds $\rho_{K\pi} < 0$ in the MCE. The effects of global conservation laws and resonance decays are also seen for ρ_{Kp} , $\rho_{p\pi}$ and ω_p .

The HSD results for ω_A and ρ_{AB} shown by the solid lines in Figs. 38 and 39 are close to the CE and MCE results for low SPS energies. One may conclude that the influence of conservation laws is more stringent at low collision energies. The HSD values for ω_A and ρ_{AB} increase, however, at high collision energies and a sizeable deviation of the HSD results from those in the MCE SM is observed with increasing energies.

In Fig. 40 the HSD scaled variance ω_π for the full acceptance is shown in A+A collisions for $b = 0$. The samples of collision events selected experimentally are 3.5% of most central collision events in Pb+Pb collisions at the SPS energies and 5% in Au+Au collisions at RHIC energies.

Fig. 40 presents the HSD results for ω_π in these samples the comparison with the HSD results at $b = 0$. One finds much larger values of ω_π in the centrality selected samples than for $b = 0$. The effect is especially strong at RHIC energies. Collisions with $b = 0$ correspond to $\omega_P \cong 0$. Thus, ω_π^* in Eq. (20) can be approximately taken as ω_π at $b = 0$. The HSD results correspond approximately to $\omega_P \cong 0.5$ for the 3.5% most central Pb+Pb collisions at SPS energies and $\omega_P \cong 1$ for the 5% most central Au+Au collisions at RHIC energies. The results of the MIS (20) for ω_π are shown by the dashed line in Fig. 40 and they are close to the actual values of the HSD simulations for ω_π .

The fluctuation in the kaon to pion ratio is dominated by the fluctuations of kaons alone since the average multiplicity of kaons is about 10 times smaller than that of pions. The model calculations of $\sigma(K\pi)$ require, in addition to ω_K , ω_π , and $\rho_{K\pi}$ values, the knowledge of the average multiplicities $\langle N_K \rangle$ and $\langle N_\pi \rangle$. To fix the average multiplicities in the SM one needs to choose the system volume. For each collision energy the volume of the statistical system has been fixed in a way to obtain the same kaon average

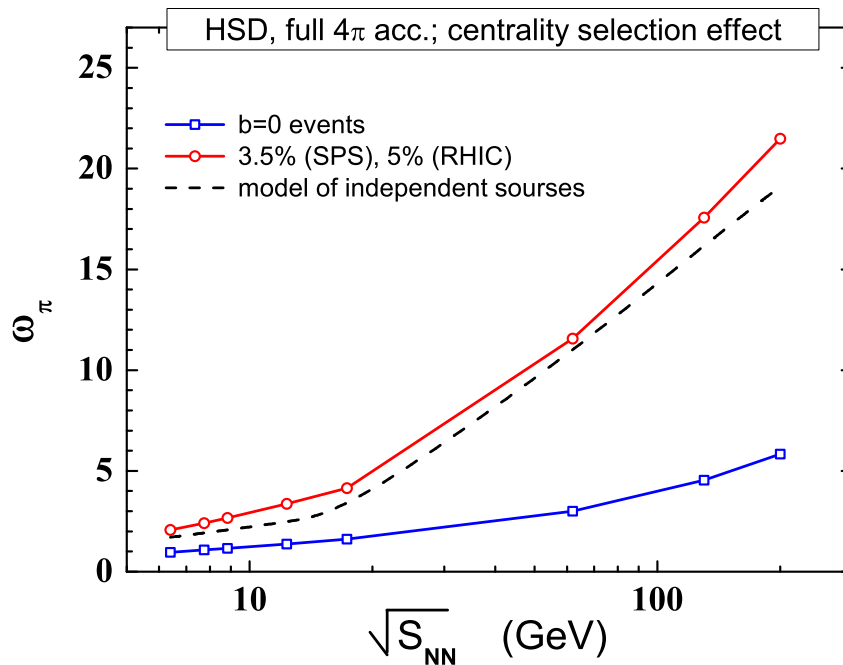


Figure 40. (Color online) The HSD results for ω_π for Pb+Pb (Au+Au) collisions at different c.m. energies $\sqrt{s_{NN}}$ within the full 4π -acceptance. The lower solid line corresponds to zero impact parameter ($b = 0$) and the upper one to the experimentally selected samples of collision events. The dashed line reflects the model of independent sources (20).

multiplicity in the SM as in the HSD calculations: $\langle N_K \rangle_{stat} = \langle N_K \rangle_{HSD}$. Recall that average multiplicities of kaons and pions are the same in all statistical ensembles. The SM volume in central Pb+Pb (Au+Au) collisions is large enough and all statistical ensembles are thermodynamically equivalent for the average pion and kaon multiplicities, since these multiplicities are much larger than 1.

In Fig. 41 the values of σ and σ_{mix} (in percents) are presented, in the *left* and *right* panel, respectively, for the SM in different ensembles as well as for the HSD simulations. A first conclusion from Fig. 41 (*left*) is that all results for σ in the different models are rather similar. One observes a monotonic decrease of σ with collision energy. This is just because of an increase of the kaon and pion average multiplicities with collision energy. The mixed event fluctuations σ_{mix} in the model analysis are fully defined by these average multiplicities according to (50). The values of σ_{mix} are therefore the same in the different statistical ensembles. They are also very close to the HSD values because the statistical system volume has been defined to obtain the same kaon average multiplicities in the statistical model as in HSD at each collision energy. As seen from Fig. 41 (*right*) the requirement of $\langle N_K \rangle_{stat} = \langle N_K \rangle_{HSD}$ leads to almost equal values of σ_{mix} in both HSD and the SM.

Differences between the statistical ensembles as well as between the statistical and

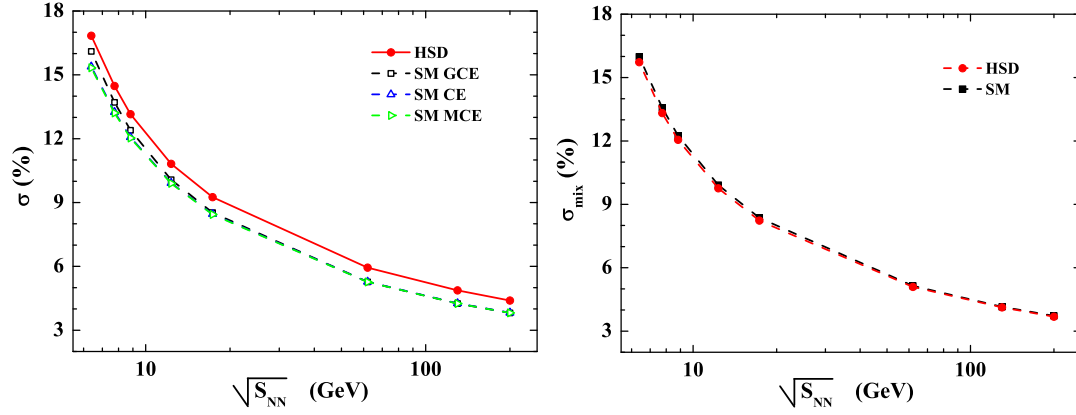


Figure 41. *Left:* The SM results in the GCE, CE, and MCE ensembles as well as the HSD results (impact parameter $b = 0$) are presented for $\sigma \cdot 100\%$ for K/π ratio in Pb+Pb (Au+Au) collisions at different c.m. energies $\sqrt{s_{NN}}$. *Right:* The same as in the *left* panel, but for $\sigma_{mix} \cdot 100\%$ in mixed events defined by (50)

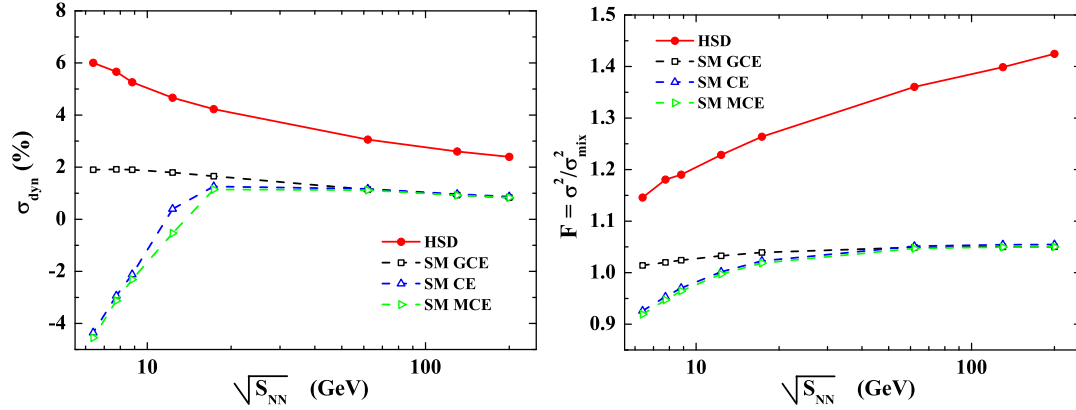


Figure 42. *Left:* The results for the K/π fluctuations at different c.m. energies $\sqrt{s_{NN}}$ in the GCE, CE, and MCE ensembles as well as from HSD (impact parameter $b = 0$) are presented for $\sigma_{dyn} \cdot 100\%$ defined by (43). *Right:* The same as in the *left* panel but for $F = \sigma^2/\sigma_{mix}^2$.

HSD results become visible for other measures of K/π fluctuations, such as σ_{dyn} defined by (43) and $F = \sigma^2/\sigma_{mix}^2$. They are shown in Fig. 42, *left* and *right*, respectively. At small collision energies the CE and MCE results in Fig. 42 demonstrate negative values of σ_{dyn} , respectively $F < 1$. When the collision energy increases, σ_{dyn} in the CE and MCE ensembles becomes positive, i.e. $F > 1$. Moreover, the different statistical ensembles approach to the same values of σ_{dyn} and F at high collision energy. In the statistical model the values of σ and σ_{mix} approach to zero at high collision energies due to an increase of the average multiplicities. The same trivial limit should be also valid for σ_{dyn} in the SM. In contrast, the measure F shows a non-trivial behavior at high energies: the SM gives $F \cong 1.05$ in high energy limit. The HSD result for F demonstrates a monotonic increase with collision energy. An interesting feature of the

SM is the approximately equal values of σ (and, thus, σ_{dyn} and F) in the CE and MCE ensembles. From Figs. 38 and 39 one observes that both ω_K , ω_π and $\rho_{K\pi}$ are rather different in the CE and MCE. Thus, as discussed above, an exact energy conservation influences the particle scaled variances and correlations. These changes are, however, cancelled out in the fluctuations of the kaon to pion ratio.

It has been mentioned in the literature (see, e.g., [95]) that the fluctuations of particle number ratio N_A/N_B are independent of volume fluctuations since both multiplicities N_A and $N + B$ are proportional to the volume. This is not correct. In fact, the *average multiplicities* $\langle N_A \rangle$ and $\langle N_B \rangle$, but not N_A and N_B , are proportional to the system volume. Let us consider the problem in the SM assuming the presence of volume fluctuations with the distribution function $W(V)$ at fixed values of T and μ_B . This assumption corresponds approximately to the volume fluctuations in A+A collisions because of different impact parameters in each collision event. Under these assumptions the SM values of ω_A , ω_B , and ρ_{AB} remain the same for any volume V (if only this volume is large enough). However, the average hadron multiplicities are proportional to the volume V . Therefore, the SM result for σ^2 reads, $\sigma^2 = \sigma_0^2 V_0/V$, where V_0 is the average system volume, and σ_0^2 is calculated with the average multiplicities corresponding to this average volume V_0 . Expanding $V_0/V = V_0/(V_0 + \delta V)$ in a series of $\delta V/V_0$, one finds to the second order in $\delta V/V_0$,

$$\sigma^2 \cong \sigma_0^2 \left[1 + \frac{\langle (\delta V)^2 \rangle}{V_0^2} \right], \quad (51)$$

where

$$\langle (\delta V)^2 \rangle = \int dV (V - V_0)^2 W(V) \quad (52)$$

corresponds to averaging over the volume distribution function $W(V)$ which describes the volume fluctuations. As clearly seen from Eq. (51) the volume fluctuations influence, of course, the K/π particle number fluctuations and make them larger. Comparing the K/π particle number fluctuations in, e.g., 1% of most central nucleus-nucleus collisions with those in, e.g., 10% one should take into account two effects. First, in the 10% sample the average volume V_0 is smaller than that in 1% sample and, thus, σ_0^2 in Eq. (51) is larger. Second, the volume fluctuations (52) in the 10% sample is larger, and this gives an additional contribution to σ^2 according to Eq. (51).

One may also consider volume fluctuations at fixed energy and conserved charges (see, e.g., Ref. [104]). In this case the connection between the average multiplicity and the volume becomes more complicated. The volume fluctuation within the MCE ensemble can strongly affect the fluctuations in the particle number ratios. This possibility will be discussed in more detail in a forthcoming study.

8.4. *Excitation Function for the Fluctuations of Ratios*

A comparison of the SM results for fluctuations in different ensembles with the data looks problematic at present; the same is true for most other theoretical models. This

is because of difficulties in implementing the experimental acceptance and centrality selection which, however, can be taken into account in the transport approach. In order to compare the HSD calculations with the measured data, the experimental cuts are applied for the simulated set of HSD events.

In Fig. 43 the HSD results of σ_{dyn} for the K/π , p/π and K/p ratios are shown in comparison with the experimental data by the NA49 Collaboration at the SPS [92] and the preliminary data of the STAR Collaboration at RHIC [93, 94, 105, 106]. The available results of UrQMD calculations (from Refs. [92, 97, 107]) are also shown by the dashed lines.

For the SPS energies we use the NA49 acceptance tables from Ref. [92]. For the RHIC energies we employ the following cuts: in pseudorapidity, $|\eta| < 1$, and in transverse momentum, $0.2 < p_T < 0.6$ GeV/c for kaons and pions and $0.4 < p_T < 1$ GeV/c for protons [93, 94, 105, 106]. We note also, that the HSD results presented in Fig. 43 correspond to the same centrality selection as in the experiment: the NA49 data correspond to the 3.5% most central collisions selected via the veto calorimeter, whereas in the STAR experiment the 5% most central events with the highest multiplicities in the pseudorapidity range $|\eta| < 0.5$ have been selected.

One sees that the UrQMD model gives practically a constant $\sigma_{dyn}^{K\pi}$, which is by about 40% smaller than the results from HSD at the lowest SPS energy. This difference between the two transport models may be attributed to different realizations of the string and resonance dynamics in HSD and UrQMD: in UrQMD the strings decay first to heavy baryonic and mesonic resonances which only later on decay to ‘light’ hadrons such as kaons and pions. In HSD the strings dominantly decay directly to ‘light’ hadrons (from the pseudoscalar meson octet) or the vector mesons ρ , ω and K^* (or the baryon octet and decouplet in case of baryon number ± 1). Such a ‘non-equilibrated’ string dynamics leads to stronger fluctuations of the K/π ratio. Note that all differences between SM and transport models, as well as between different versions of the transport models, become clearly seen at the lower bombarding energies. This is only because of using σ_{dyn} as a measure of the K/π ratio fluctuations. If one uses $F = \sigma^2/\sigma_{mix}^2$ as a measure of the K/π fluctuations the conclusion will be opposite: as Fig. 42 (*right*) demonstrates the difference between the SM and HSD predictions measured in F would increase with collision energy.

The excitation function of σ_{dyn}^{Kp} for the K/p ratio is presented in the middle panel of Fig. 43. The ‘stars’ correspond to the preliminary STAR data in Au+Au collisions [106]. The HSD results for σ_{dyn}^{Kp} show a weak energy dependence in both SPS and RHIC energy regions. However, as follows from our analysis this observable is very sensitive to the experimental acceptance. In order to illustrate it, we extended the HSD calculations for Au+Au within the STAR acceptance for SPS energies also - cf. the upper red line with solid dots, which is higher than the HSD result for Pb+Pb obtained for the NA49 acceptance - lower blue line with open dots. The influence of the experimental acceptance is clearly seen at 158 AGeV where a switch from the NA49 to the STAR acceptance leads to a jump in σ_{dyn}^{Kp} by more than 3%. On the other hand, our calculations

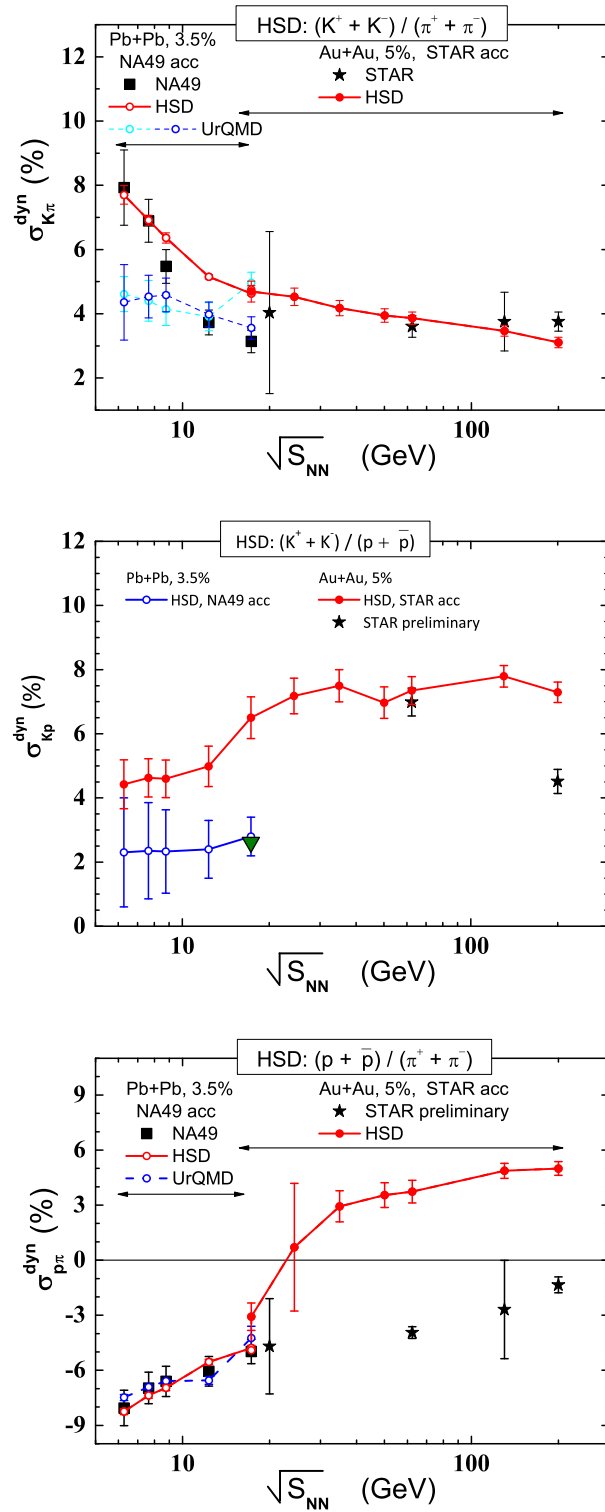


Figure 43. The HSD results for the excitation function in σ_{dyn} for the K/π , K/p , p/π ratios within the experimental acceptance (solid line) in comparison to the experimental data measured by the NA49 Collaboration at SPS [92] and by the STAR Collaboration at RHIC [93,94,105,106]. The UrQMD calculations are shown by dotted lines.

for Pb+Pb (3.5% central) and for Au+Au (5% central) collisions - performed within the NA49 acceptance for both cases at 160 AGeV - shows a very weak sensitivity of σ_{dyn}^{Kp} on the actual choice of the collision system and centrality – cf. the coincident open circle and triangle at 158 AGeV in the middle panel of Fig. 43. Indeed, new data from NA49 and STAR should clarify the situation.

At SPS energies the HSD simulations lead to negative values of σ_{dyn} for the proton to pion ratio – cf. Fig. 43, lower panel. This is in agreement with the NA49 data in Pb+Pb collisions. On the other hand HSD gives large positive values of $\sigma_{dyn}^{p\pi}$ at RHIC energies which strongly overestimate the preliminary STAR data for Au+Au collisions [105].

9. Summary

The present review has been devoted to a systematic study of fluctuations and correlations in heavy-ion collisions within the HSD and UrQMD transport models. This provides a powerful tool to simulate experimental collisions on an event-by-event basis.

In Section 3 the centrality dependence of multiplicity fluctuations has been studied in fixed target A+A experiments. The centrality selection in Pb+Pb collisions at 158 AGeV has been performed in full correspondence to the NA49 experimental procedure: only the samples of events with fixed numbers of the projectile participants, N_P^{proj} , have been considered. A decrease of the scaled variance ω_P for the participant number fluctuations with N_P^{proj} in central A+A collisions has been found. The transport model results for the scaled variances ω_i of negative, positive, and all charged hadrons in Pb+Pb at 158 AGeV have been presented and interpreted. The samples with $N_P^{proj} = 20 \div 30$ show a maximum of fluctuations of the number of target nucleon participants N_P^{targ} . The final hadron multiplicity fluctuations exhibit an analogous behavior. This explains the large values of the HSD and UrQMD scaled variances ω_i for positive, negative, and all charged hadrons in the target hemispheres and in the full 4π acceptance. The asymmetry between the projectile and target participants – introduced in the data samples by the trigger condition of fixed N_P^{proj} – can be used to explore different dynamical scenarios for A+A collisions by measuring the final multiplicity fluctuations as a function of rapidity (cf. Fig. 9). The analysis reveals that the NA49 data indicate a rather strong mixing of the longitudinal flows of the projectile and target hadron production sources. This sheds new light on the A+A reaction dynamics at top SPS energies. The data demonstrate a significantly larger amount of mixing than generated in hadron-string transport approaches. This probably points towards the presence of strongly interacting quark-gluon phase.

In Section 4 the particle number fluctuations in central A+A collisions from 10 to 21300 AGeV have been studied within the HSD transport model. HSD predicts that the scaled variances ω_i in central A+A collisions remain close to the corresponding values in $p+p$ collisions and increase with collision energy with the multiplicity per participating nucleon, $\omega_i \propto n_i$. The scaled variances ω_i calculated within the statistical hadron-

resonance gas (HG) model along the chemical freeze-out line show a rather different behavior: the ω_i approach finite values at high collision energy. At the top RHIC energy $\sqrt{s_{NN}} = 200$ GeV the HSD results for ω_i (HSD) are already about 10 times larger than the corresponding micro-canonical (MCE) HG values for ω_i (MCE). Thus, the HSD and HG scaled variances ω_i show a different energy dependence and are very different numerically at high energies. However, a comparison with the NA49 data of very central, $\leq 1\%$, Pb+Pb collisions in the SPS energy range does not distinguish between the HSD and MCE HG results. This occurs because of two reasons: First, the MCE HG and HSD results for ω_i at SPS energies are not too much different from each other at SPS energies as well as from the ω_i values in p+p collisions. Second, small experimental values of the acceptance, $q = 0.04 \div 0.16$, and about 10% possible ambiguities coming from the acceptance scaling relation (28) make the difference between the HSD and MCE HG results almost invisible. New measurements of ω_i for samples of very central A+A collisions with large acceptance at both SPS and RHIC energies are needed to allow for a proper determination of the underlying dynamics.

In Section 5 the event-by-event multiplicity fluctuations in A+A collisions have been studied for different energies and system sizes within the transport approach. This study is in full correspondence to the future experimental program of the NA61 Collaboration at the SPS. The central C+C, S+S, In+In, and Pb+Pb nuclear collisions from $E_{lab} = 10, 20, 30, 40, 80, 158$ AGeV have been investigated. The influence of participant number fluctuations on hadron multiplicity fluctuations has been emphasized and studied in detail. To make these ‘trivial’ fluctuations smaller, one has to consider the most central collisions. Indeed, one needs to make a very rigid selection – 1% or smaller – of the ‘most central’ collision events. In addition, one wants to compare the event-by-event fluctuations in these ‘most central’ collisions for heavy and for light nuclei. Under these new requirements different centrality selections are not equivalent to each other. As a consequence, there is no universal geometrical selection by the impact parameter. This is a new and serious problem for theoretical models (e.g. for hydrodynamical models) in a precision description of the event-by-event fluctuation data. The above statements have been illustrated by the $b = 0$ selection criterium. For light nuclei even these ‘absolutely central’ geometrical collisions lead to rather large fluctuations of the number of participants, essentially larger than in the 1% most central collisions selected by the largest values of the projectile participants N_P^{proj} . The multiplicity fluctuations calculated in these samples show a much weaker dependence on the atomic mass number A than for the criterium of zero impact parameter $b = 0$. A monotonic energy dependence for the multiplicity fluctuations is obtained in both the HSD and UrQMD transport models. The two models demonstrate a similar qualitative behavior of the particle number fluctuations. Our study has also demonstrated a sensitivity of the multiplicity fluctuations to some specific details of the transport models. Thus, the present HSD and UrQMD results for the scaled variances provide a general trend of their dependencies on A and E_{lab} and indicate quantitatively the systematic uncertainties. It has to be stressed again, that HSD and UrQMD - in their present formulations - do not

include explicitly a phase transition to the QGP. The expected enhanced fluctuations – attributed to the critical point and phase transition – can be observed experimentally on top of a monotonic and smooth ‘hadronic background’. The most promising signature of the QCD critical point would be an observation of a non-monotonic dependence of the scaled variances with bombarding energy E_{lab} for central A+A collisions with fixed atomic mass number. In the fixed target SPS experiments the measurements of ω_- , ω_+ , and ω_{ch} are preferable in the forward hemispheres. In this case the remaining small fluctuations of the number of target participants N_P^{targ} in the 1% most central collisions – defined by the number of the projectile participants N_P^{proj} – become even less important, as they contribute mainly to the particle fluctuations in the backward hemisphere. These findings are expected to be helpful for the optimal choice of collision systems and collision energies for the experimental search of the QCD critical point.

In Section 6 the HSD transport model has been used to calculate the scaled variance of participant number fluctuations, ω_P , and the number of i 'th hadrons per nucleon accepted by the mid-rapidity PHENIX detector, $q_i n_i$, in different Beam-Beam Counter centrality classes. The HSD model for N+N collisions has been also used to estimate the fluctuations from a single source, ω_i^* . It has been found that the model of independent sources based on these HSD results leads to a good agreement with the PHENIX data [76, 77]. In different 5% centrality classes, ω_P goes down and $q_i n_i$ goes up with increasing of $\langle N_P \rangle$. This results in a non-monotonic dependence of ω_i^{acc} on $\langle N_P \rangle$ as seen in the PHENIX data. Thus, one may conclude that the centrality dependence of the fluctuations seen in the present PHENIX data are the consequences of participant number fluctuations. To avoid a dominance of the participant number fluctuations we stress again that one needs to analyze most central collisions with a much more rigid ($\leq 1\%$) centrality selection.

The system size event-by-event fluctuations induce also rapidity forward-backward correlations in relativistic A+A collisions. The analysis has been based on two independent models – the microscopic HSD transport approach and a ‘toy’ wounded nucleon model realized as a Glauber Monte Carlo event generator. It has been shown that strong forward-backward correlations arise due to an averaging over many different events that belong to one 10% centrality bin. In contrast to average multiplicities, the resulting fluctuations and correlations depend strongly on the specific centrality trigger. For example, the centrality selection via impact parameter b (used in most theoretical calculations) and via N_{ch}^{ref} (used experimentally) lead to rather different values of participant number fluctuations ω_P and forward-backward correlation parameters ρ . These different centrality selections give also quite different dependencies of ω_P and ρ on centrality. The HSD simulations reveal strong forward-backward correlations and reproduce the main qualitative features of the STAR data in Au+Au collisions at RHIC energies [82, 83]. The forward-backward correlations can be studied experimentally for smaller size centrality bins defined by N_{ch}^{ref} . When the size of the bins decreases, the contribution of ‘geometrical’ fluctuations should lead to weaker forward-backward correlations and to a less pronounced centrality dependence. Note, that the ‘geometrical’

fluctuations discussed here are in fact present in all dynamical models of A+A collisions. Thus, they should be carefully accounted before any discussion of new physical effects is addressed. A future experimental analysis – in the direction examined here – should clarify whether the observed correlations by the STAR Collaboration at RHIC contain really additional contributions from ‘new physics’.

In Section 7 the transport approach has been used to investigate the event-by-event fluctuations of baryon number and electric charge in A+A collisions. The study has been based on the microscopic HSD transport model which allows to analyze on the event-by-event basis the influence of two main sources of the conserved charge fluctuations – the fluctuations of the number of participants and the finite experimental acceptance. It has been found that the fluctuations in the number of target participants strongly influences the baryon number and electric charge fluctuations. The consequences depend crucially on the dynamics of the initial flows of the conserved charges. For a better understanding of the HSD results three limiting groups of models for A+A collisions have been discussed: transparency, mixing and reflection. These “pedagogical” considerations indicate that the HSD model shows only a small mixing on initial baryon flow and is closer to the transparency models. This makes important the findings of Refs. [26, 43, 108, 109] about the influence of the partonic degrees of freedom on the initial phase dynamics. This phase might increase the mixing of conserved charges by additional strong parton-parton interactions.

In Section 8 the event-by-event multiplicity fluctuations of pions, kaons, protons as well as their correlations and ratio fluctuations in central Au+Au (or Pb+Pb) collisions from low SPS up to top RHIC energies have been studied within the HSD transport approach and in the statistical hadron-resonance gas model for different statistical ensembles – the grand canonical ensemble (GCE), canonical ensemble (CE), and micro-canonical ensemble (MCE). The HSD results at SPS energies are close to those in the CE and MCE statistical models. This indicates a dominant role of resonance decays and global conservation laws for low energy A+A collisions. On the other hand, substantial differences in HSD and statistical model results have been observed at RHIC energies which can be attributed to non-equilibrium dynamical effects in the HSD simulations. Thus, the scaled variances of different particle species may serve as good observables to probe the amount of equilibration achieved in central A+A collisions at RHIC energies. On the other hand, it has been found that the observable σ_{dyn} , which characterizes ratio fluctuations, appears to be rather sensitive to the details of the model at low collision energies. It has been found that HSD can qualitatively reproduce the measured excitation function for the K/π ratio fluctuations in central Au+Au (or Pb+Pb) collisions from low SPS up to top RHIC energies. The HSD results for $\sigma_{dyn}^{p\pi}$ appear to be close to the NA49 data at the SPS. The data for σ_{dyn}^{Kp} in Pb+Pb collisions at the SPS energies will be available soon and allow for further insight. A comparison of the HSD results with preliminary STAR data in Au+Au collisions at RHIC energies are not fully conclusive: σ_{dyn} from the HSD calculations is approximately in agreement with data [106] for the kaon to proton ratio, but overestimates the experimental results [105]

for the proton to pion ratio. New data on event-by-event fluctuations in Au+Au at RHIC energies will help to clarify the situation.

It has been argued in the Introduction that event-by-event fluctuations in nucleus-nucleus collisions can be considered as a probe for the phase transition and the QCD critical point. The transport models have been employed to study the fluctuations and correlations including the influence of experimental acceptance as well as the centrality selection, the dependence on the system size and collision energy.

So far, the transport models employed do not include an explicit phase transition to the QGP as well as a dynamical description of hadronization. Recent steps have been taken in this direction within Parton-Hadron-String-Dynamics (PHSD) approach [110,111] that incorporates the partonic dynamics in line with an equation of state from lattice QCD. Nevertheless, the comparison of results from microscopic transport models with experimental data will allow to separate the effects indicated by a phase transition to the QGP and the QCD critical point.

Acknowledgments

We like to thank V.V. Begun, M. Bleicher, H. Büsching, W. Cassing, M. Gaździcki, M. Hauer, C. Höhne, D. Kresan, O. Linnyk, B. Lungwitz, I. N. Mishustin, J. T. Mitchell, M. Mitrovski, L. M. Satarov, T. Schuster, Yu. M. Sinyukov, R. Stock, H. Stöcker, H. Ströbele, T. Tarnowsky, G. Torrieri, G. Westfall and O. S. Zozulya for useful discussions. V.K.'s work was supported by the Helmholtz International Center for FAIR within the framework of the LOEWE program (Landesoffensive zur Entwicklung Wissenschaftlich-Ökonomischer Exzellenz) launched by the State of Hesse.

References

- [1] NA38, M. C. Abreu *et al.*, Phys. Lett. **B449**, 128 (1999).
- [2] NA49, J. Bachler *et al.*, Nucl. Phys. **A661**, 45 (1999).
- [3] NA50, B. Alessandro *et al.*, Eur. Phys. J. **C39**, 335 (2005), hep-ex/0412036.
- [4] NA60, R. Arnaldi *et al.*, J. Phys. **G32**, S51 (2006), nucl-ex/0609039.
- [5] NA49-future, M. Gaździcki *et al.*, A new sps programme Vol. CPOD2006, p. 016, 2006, nucl-ex/0612007.
- [6] BRAHMS, I. Arsene *et al.*, Nucl. Phys. **A757**, 1 (2005), nucl-ex/0410020.
- [7] B. B. Back *et al.*, Nucl. Phys. **A757**, 28 (2005), nucl-ex/0410022.
- [8] STAR, J. Adams *et al.*, Nucl. Phys. **A757**, 102 (2005), nucl-ex/0501009.
- [9] PHENIX, K. Adcox *et al.*, Nucl. Phys. **A757**, 184 (2005), nucl-ex/0410003.
- [10] ALICE, K. Aamodt *et al.*, JINST **0803**, S08002 (2008).
- [11] K. Peters, AIP Conf. Proc. **814**, 33 (2006).
- [12] A. N. Sissakian, A. S. Sorin, and V. D. Toneev, (2006), nucl-th/0608032.
- [13] The NA49, S. V. Afanasiev *et al.*, Phys. Rev. **C66**, 054902 (2002), nucl-ex/0205002.
- [14] The NA49, C. Alt *et al.*, J. Phys. **G30**, S119 (2004), nucl-ex/0305017.
- [15] V. Toneev, PoS **CPOD07**, 057 (2007), 0709.1459.
- [16] P. Braun-Munzinger, K. Redlich, and J. Stachel, (2003), nucl-th/0304013.
- [17] J. Cleymans and K. Redlich, Phys. Rev. Lett. **81**, 5284 (1998), nucl-th/9808030.
- [18] J. Cleymans and K. Redlich, Phys. Rev. **C60**, 054908 (1999), nucl-th/9903063.

- [19] A. Andronic, P. Braun-Munzinger, and J. Stachel, Nucl. Phys. **A772**, 167 (2006), nucl-th/0511071.
- [20] Z. Fodor and S. D. Katz, JHEP **04**, 050 (2004), hep-lat/0402006.
- [21] F. Karsch, J. Phys. **G30**, S887 (2004), hep-lat/0403016.
- [22] R. Anishetty, P. Koehler, and L. D. McLerran, Phys. Rev. **D22**, 2793 (1980).
- [23] S. Date, M. Gyulassy, and H. Sumiyoshi, Phys. Rev. **D32**, 619 (1985).
- [24] L. V. Bravina *et al.*, Phys. Rev. **C60**, 024904 (1999), hep-ph/9906548.
- [25] L. V. Bravina *et al.*, Nucl. Phys. **A698**, 383 (2002), nucl-th/0104023.
- [26] E. L. Bratkovskaya *et al.*, Phys. Rev. **C69**, 054907 (2004), nucl-th/0402026.
- [27] M. Gazdzicki, M. I. Gorenstein, and S. Mrowczynski, Phys. Lett. **B585**, 115 (2004), hep-ph/0304052.
- [28] M. A. Stephanov, K. Rajagopal, and E. V. Shuryak, Phys. Rev. **D60**, 114028 (1999), hep-ph/9903292.
- [29] C. R. Allton *et al.*, Phys. Rev. **D68**, 014507 (2003), hep-lat/0305007.
- [30] NA61, A. Laszlo *et al.*, PoS **CPOD07**, 054 (2007), 0709.1867.
- [31] W. Ehehalt and W. Cassing, Nucl. Phys. **A602**, 449 (1996).
- [32] W. Cassing and E. L. Bratkovskaya, Phys. Rept. **308**, 65 (1999).
- [33] S. A. Bass *et al.*, Prog. Part. Nucl. Phys. **41**, 255 (1998), nucl-th/9803035.
- [34] M. Bleicher *et al.*, J. Phys. **G25**, 1859 (1999), hep-ph/9909407.
- [35] E. L. Bratkovskaya and W. Cassing, Nucl. Phys. **A807**, 214 (2008), 0712.0635.
- [36] W. Cassing, Eur. Phys. J. ST **168**, 3 (2009), 0808.0715.
- [37] K. Weber *et al.*, Nucl. Phys. **A539**, 713 (1992).
- [38] W. Cassing, Nucl. Phys. **A700**, 618 (2002), nucl-th/0105069.
- [39] J. Geiss, W. Cassing, and C. Greiner, Nucl. Phys. **A644**, 107 (1998), nucl-th/9805012.
- [40] B. Nilsson-Almqvist and E. Stenlund, Comput. Phys. Commun. **43**, 387 (1987).
- [41] T. Falter, *Nuclear reactions of high energy protons, photons, and leptons*, PhD thesis, Uni. Giessen, 2004.
- [42] Particle Data Group, L. Montanet *et al.*, Phys. Rev. **D50**, 1173 (1994).
- [43] H. Weber, E. L. Bratkovskaya, W. Cassing, and H. Stoecker, Phys. Rev. **C67**, 014904 (2003), nucl-th/0209079.
- [44] E. L. Bratkovskaya, S. Soff, H. Stoecker, M. van Leeuwen, and W. Cassing, Phys. Rev. Lett. **92**, 032302 (2004), nucl-th/0307098.
- [45] V. P. Konchakovski *et al.*, Phys. Rev. **C73**, 034902 (2006), nucl-th/0511083.
- [46] NA49, M. Rybczynski *et al.*, J. Phys. Conf. Ser. **5**, 74 (2005), nucl-ex/0409009.
- [47] H. Heiselberg, Phys. Rept. **351**, 161 (2001), nucl-th/0003046.
- [48] A. Bialas, M. Bleszynski, and W. Czyz, Nucl. Phys. **B111**, 461 (1976).
- [49] M. Gazdzicki and M. I. Gorenstein, Phys. Lett. **B640**, 155 (2006), hep-ph/0511058.
- [50] U. Katscher *et al.*, Z. Phys. **A346**, 209 (1993).
- [51] Y. B. Ivanov, V. N. Russkikh, and V. D. Toneev, Phys. Rev. **C73**, 044904 (2006), nucl-th/0503088.
- [52] NA49, T. Anticic *et al.*, Phys. Rev. **C69**, 024902 (2004).
- [53] M. Gazdzicki and M. I. Gorenstein, Acta Phys. Polon. **B30**, 2705 (1999), hep-ph/9803462.
- [54] A. Bialas and W. Czyz, Acta Phys. Polon. **B36**, 905 (2005), hep-ph/0410265.
- [55] PHOBOS, B. B. Back *et al.*, Phys. Rev. **C72**, 031901 (2005), nucl-ex/0409021.
- [56] NA49, C. Alt *et al.*, Phys. Rev. Lett. **94**, 192301 (2005), nucl-ex/0409004.
- [57] V. P. Konchakovski, M. I. Gorenstein, and E. L. Bratkovskaya, Phys. Lett. **B651**, 114 (2007), nucl-th/0703052.
- [58] Z. Koba, H. B. Nielsen, and P. Olesen, Nucl. Phys. **B40**, 317 (1972).
- [59] A. I. Golokhvastov, Sov. J. Nucl. Phys. **27**, 430 (1978).
- [60] M. Gazdzicki, R. Szwed, G. Wrochna, and A. K. Wroblewski, Mod. Phys. Lett. **A6**, 981 (1991).
- [61] A. Wroblewski, Acta Phys. Polon. **B4**, 857 (1973).

- [62] B. Andersson, G. Gustafson, and H. Pi, *Z. Phys.* **C57**, 485 (1993).
- [63] V. V. Begun *et al.*, *Phys. Rev.* **C76**, 024902 (2007), nucl-th/0611075.
- [64] V. V. Begun, M. Gazdzicki, M. I. Gorenstein, and O. S. Zozulya, *Phys. Rev.* **C70**, 034901 (2004), nucl-th/0404056.
- [65] V. V. Begun, M. I. Gorenstein, M. Hauer, V. P. Konchakovski, and O. S. Zozulya, *Phys. Rev.* **C74**, 044903 (2006), nucl-th/0606036.
- [66] NA49, B. Lungwitz *et al.*, Energy dependence of multiplicity fluctuations in heavy ion collisions Vol. CFRNC2006, p. 024, 2006, nucl-ex/0610046.
- [67] B. Lungwitz and M. Bleicher, *Phys. Rev.* **C76**, 044904 (2007), 0707.1788.
- [68] M. Hauer, *Phys. Rev.* **C77**, 034909 (2008), 0710.3938.
- [69] M. Gazdzicki, *Eur. Phys. J. ST* **155**, 37 (2008), 0801.4919.
- [70] M. A. Stephanov, K. Rajagopal, and E. V. Shuryak, *Phys. Rev. Lett.* **81**, 4816 (1998), hep-ph/9806219.
- [71] M. Stephanov, *Acta Phys. Polon.* **B35**, 2939 (2004).
- [72] W. Broniowski and W. Florkowski, *Phys. Rev.* **C65**, 024905 (2002), nucl-th/0110020.
- [73] B. M. Tavares, H. J. Drescher, and T. Kodama, *Braz. J. Phys.* **37**, 41 (2007), hep-ph/0702224.
- [74] V. P. Konchakovski, M. I. Gorenstein, and E. L. Bratkovskaya, *Phys. Rev.* **C76**, 031901 (2007), 0704.1831.
- [75] V. P. Konchakovski, M. Hauer, G. Torrieri, M. I. Gorenstein, and E. L. Bratkovskaya, *Phys. Rev.* **C79**, 034910 (2009), 0812.3967.
- [76] PHENIX, S. S. Adler *et al.*, *Phys. Rev.* **C71**, 034908 (2005), nucl-ex/0409015.
- [77] J. T. Mitchell, *J. Phys. Conf. Ser.* **27**, 88 (2005), nucl-ex/0511033.
- [78] A. Bialas and R. B. Peschanski, *Nucl. Phys.* **B273**, 703 (1986).
- [79] S. Jeon, L. Shi, and M. Bleicher, *Phys. Rev.* **C73**, 014905 (2006), nucl-th/0506025.
- [80] N. Armesto, M. A. Braun, E. G. Ferreira, and C. Pajares, *Phys. Rev. Lett.* **77**, 3736 (1996), hep-ph/9607239.
- [81] M. A. Braun and C. Pajares, *Phys. Rev. Lett.* **85**, 4864 (2000), hep-ph/0007201.
- [82] N. Armesto, L. McLerran, and C. Pajares, *Nucl. Phys.* **A781**, 201 (2007), hep-ph/0607345.
- [83] T. Lappi and L. McLerran, *Nucl. Phys.* **A772**, 200 (2006), hep-ph/0602189.
- [84] STAR, T. J. Tarnowsky, *PoS CPOD07*, 019 (2007), 0711.1175.
- [85] T. Tarnowsky, R. Scharenberg, and B. Srivastava, *Int. J. Mod. Phys.* **E16**, 1859 (2007), nucl-ex/0702055.
- [86] B. Alver, M. Baker, C. Loizides, and P. Steinberg, (2008), 0805.4411.
- [87] V. P. Konchakovski, M. I. Gorenstein, E. L. Bratkovskaya, and H. Stoecker, *Phys. Rev.* **C74**, 064911 (2006), nucl-th/0606047.
- [88] S. Jeon and V. Koch, (2003), hep-ph/0304012.
- [89] NA49, T. Anticic *et al.*, *Phys. Rev.* **C70**, 034902 (2004), hep-ex/0311009.
- [90] NA49, P. Dinkelaker, *J. Phys.* **G31**, S1131 (2005).
- [91] NA49, S. V. Afanasev *et al.*, *Phys. Rev. Lett.* **86**, 1965 (2001), hep-ex/0009053.
- [92] NA49, C. Alt *et al.*, *Phys. Rev.* **C79**, 044910 (2009), 0808.1237.
- [93] STAR, S. Das, *J. Phys.* **G32**, S541 (2006).
- [94] STAR, B. I. Abelev, *Phys. Rev. Lett.* **103**, 092301 (2009), 0901.1795.
- [95] G. Baym and H. Heiselberg, *Phys. Lett.* **B469**, 7 (1999), nucl-th/9905022.
- [96] S. Jeon and V. Koch, *Phys. Rev. Lett.* **83**, 5435 (1999), nucl-th/9906074.
- [97] NA49, C. Roland *et al.*, *J. Phys.* **G30**, S1381 (2004), nucl-ex/0403035.
- [98] M. I. Gorenstein, M. Hauer, V. P. Konchakovski, and E. L. Bratkovskaya, *Phys. Rev.* **C79**, 024907 (2009), 0811.3089.
- [99] V. P. Konchakovski, M. Hauer, M. I. Gorenstein, and E. L. Bratkovskaya, *J. Phys.* **G36**, 125106 (2009), 0906.3229.
- [100] S. A. Voloshin, V. Koch, and H. G. Ritter, *Phys. Rev.* **C60**, 024901 (1999), nucl-th/9903060.
- [101] M. Gazdzicki and S. Mrowczynski, *Z. Phys.* **C54**, 127 (1992).

- [102] S. Mrowczynski, Phys. Lett. **B430**, 9 (1998), nucl-th/9712030.
- [103] V. Koch and T. Schuster, (2009), 0911.1160.
- [104] V. V. Begun, M. Gazdzicki, and M. I. Gorenstein, Phys. Rev. **C78**, 024904 (2008), 0804.0075.
- [105] G. Westfall, p/π fluctuations in au-au collisions in star, in *poster at Quark Matter 2009*, 2009.
- [106] J. Tian, Event-by-event p/k fluctuations from a+a collisions at rhic, in *poster at Quark Matter 2009*, 2009.
- [107] D. Kresan and V. Friese, PoS **CFRNC2006**, 017 (2006).
- [108] E. L. Bratkovskaya *et al.*, Prog. Part. Nucl. Phys. **53**, 225 (2004), nucl-th/0312048.
- [109] E. L. Bratkovskaya, W. Cassing, and H. Stoecker, Phys. Rev. **C67**, 054905 (2003), nucl-th/0301083.
- [110] W. Cassing and E. L. Bratkovskaya, Phys. Rev. **C78**, 034919 (2008), 0808.0022.
- [111] W. Cassing and E. L. Bratkovskaya, Nucl. Phys. **A831**, 215 (2009), 0907.5331.